

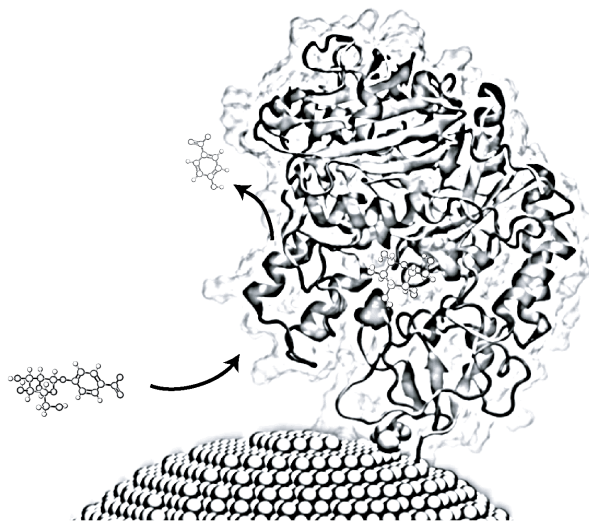
College of Engineering, Mathematics and Physical Sciences



A whispering gallery mode based biosensor platform for single enzyme analysis

Submitted by Sivaraman Subramanian, to the University of Exeter as a thesis for the degree of Doctor of Philosophy in Physics, December 2020.

This thesis is available for Library use on the understanding that it is copyright material and that no quotation from the thesis may be published without proper acknowledgement.



I certify that all material in this thesis which is not my own work has been identified and that any material that has previously been submitted and approved for the award of a degree by this or any other University has been acknowledged.

Signature:

Date: August 20, 2021

Acknowledgements

It would be an understatement to say that this work would not be possible without the help and support of many people. I would like to take this opportunity to thank everyone who aided me in this journey. Firstly, I would like to thank my supervisor, Frank Vollmer, for guiding me and providing the space and time to explore my own ideas. Although many of my attempts could not directly be part of this thesis, I am grateful for the freedom I received to learn things at my own pace. I am sure that these efforts will be useful to someone down the line who attempts this path. A special thanks to Martin Baaske, Eugene Kim and Jon Swaim for paving the path for me to undertake this work without which this task would have been much more difficult. I would like to thank Serge Vincent, a fellow traveller and friend, for the critical discussions, support and encouragement. I would also like to thank my co-supervisor, Bill Barnes, for his guidance at a time where I was a bit lost. I thank my pastoral tutor Sharon Strawbridge for providing me with advice when I really needed it and assuring me that the thesis would come together in time.

This work was conducted partly at the Max Planck Institute for the Science of Light. I would like to thank all my colleagues and friends from the MPL, Matthew Foreman, Lu, Martin Butryn, Ali Mahdavi, Ying-Jen Chen, Aaron Webster, Paul Roth, Ulrike Schöler, and Roman Guliaev. I would like to thank my colleagues at the University of Exeter, Callum Jones, Aneeth Kakkanattu Arunkumar, Katya Zossimova, Jolly Xavier, Hsin-Yu Wu, Rithvik Gutha, Gema Cabello, and Tom Constant. I would like to specially thank, Simona Frustaci, Aruturo Bianchetti, Fabian Meder, Marianna Serrano, Matias Rafti, Silvan Englisch, Tobias Zech, Mayuk Nath and Tobias Lutz, whose collaboration and friendship I greatly appreciate. These past few years at University of Exeter has been fantastic thanks to my friends, David, Adrian, Henry, Andrea, Micheal, Tobi, Anna, Simona, Konstantinos, Simone, Dave, Seb, Bob, Michele, Nathan, Denzel, the Erratics CC and the Woodbury & Newton St Cyres CC.

Most importantly, I would like to thank my family, my parents, JS and Kala, and my brother Srikanth, for supporting me through this endeavour. Thank you for your patience and for always being there for me. I would like to thank Melissa, for her love and support, and tolerating me for these past 6 months. A friend in need is a friend indeed. I am very grateful for my friends, Ram, Nila, Bilal, Ashish, Varun, Sriklant, Vijay, and Ankit.

Abstract

Enzymes catalyze most of the biochemical reactions in our cells. The functionality of enzymes depends on their dynamics starting from small bond vibrations in the fs timescale to large domain motions in the microsecond-millisecond timescale. Understanding the precise and rapid positioning of atoms within a catalytic site by an enzyme's molecular movements is crucial for understanding biomolecular processes and for realizing synthetic biomolecular machines in the longer term. Hence, sensors capable of studying enzymes over a wide range of amplitudes and timescale and ideally one enzyme at a time are required. Many capable single-molecule techniques have been established in the past three decades, each with its pros and cons. This thesis presents the development of one such single-molecule sensor. The sensor is based on plasmonically enhanced whispering gallery mode resonators and is capable of studying enzyme kinetics and large-scale dynamics over the timescale of ns-seconds. Unlike fluorescence techniques which require labeling of the enzymes with dyes, the technique presented in this work detects single enzymes immobilized on the surface of plasmonic gold nanoparticles. A fast, low-noise, lock-in method is utilized to extract sensor signals in the microsecond timescale. Using a model enzyme, the ability of the sensor to detect conformational fluctuations of single enzymes is shown. Further, the thermodynamics of the enzyme is studied and the relevant thermodynamic parameters are extracted from the single-molecule data. Additionally, we extract the heat capacity changes associated with the enzyme using the single-molecule data. The sensor system presented in this thesis in the future could enable a fast, real-time, rapid throughput, lab-on-chip sensor system for studying single enzymes for both research and clinical use.

keywords: enzymes, dynamics, single molecule, plasmonics, whispering gallery mode

Contents

1	Introduction	1
1.1	Why single-molecules?	1
1.2	Proteins as dynamic molecules	3
1.3	Methods for studying protein dynamics	4
1.4	Plasmonic and optical microcavity single-molecule sensors	6
1.4.1	Plasmonic sensing approaches	6
1.4.2	Optical microcavities	8
1.5	Thesis outline	10
2	Theory	13
2.1	Optical whispering gallery modes	13
2.1.1	Whispering gallery modes in spherical resonators	14
2.1.2	Utilizing WGMs for sensing applications	18
2.2	Plasmonic nanoparticles	24
2.2.1	Spherical nanoparticle in an electric field	25
2.2.2	Tuning LSPRs	28
2.2.3	LSPR based sensing	29
2.3	WGM-plasmon hybrid sensing	30
3	Experimental design	32
3.1	Experimental setup	32
3.2	Fabrication of glass microspheres	33
3.3	Efficient coupling to optical WGMs	34
3.4	Acquisition of the WGM spectra	36

3.5	Implementation of the Pound-Drever-Hall lock	36
3.6	Data acquisition and analysis	37
3.7	Standard protocol for single-molecule experiments	39
4	Sensing with WGMs: Nanoparticles to single molecules	42
4.1	Detection of single gold nanoparticles	42
4.1.1	Dependence of the WGM wavelength shifts on the polarizability of nanoparticles	43
4.1.2	Binding of gold nanoparticles to the WGM cavity	44
4.2	Single-molecule detection using a plasmon-enhanced WGM microcavity	46
4.2.1	Immobilization of single molecules	46
4.2.2	Measuring the hybridization kinetics of DNA oligonucleotides	48
4.3	Conclusions	53
5	Single-molecule sensing by effective linewidth shifts of WGMs	55
5.1	Introduction	55
5.2	Frequency splitting of WGMs due to the presence of multiple surface scatterers	55
5.3	Detection of single molecules using linewidth shifts of WGMs	58
5.4	Conclusions	61
6	Fast detection of nanoparticles and single molecules	63
6.1	Introduction	63
6.2	Frequency lock-in using the Pound-Drever-Hall (PDH) method	64
6.3	Measurement of the diffusion of gold nanoparticles in water	67
6.4	Conclusions	68
7	Studying the thermodynamics of single enzymes using WGM-plasmonic sensors	69
7.1	Introduction	69
7.2	Specific immobilization of the enzyme	71
7.3	Molecular dynamics simulations of the enzyme-gold interactions	74
7.4	Measuring the enzyme-substrate interaction	76
7.5	Temperature dependent kinetics of the enzyme	78

7.6	Conclusions	81
8	Conclusions and Outlook	83
A	Maxwell's equations in spherical coordinates	86
B	Notes on sensor assembly and gold nanorod functionalization	89
C	All-atom molecular dynamics simulations in GROMACS	91
C.1	Creating the simulation geometry	94
C.2	Topology file, solvation and neutralization	98
C.3	Energy minimization	99
C.4	Temperature equilibration	100
C.5	Production MD run	102

List of Figures

1.1	Examples of domains where single-molecule measurement prove useful.	2
1.2	Energy landscape of a protein showing the hierarchy of dynamics over various timescales and the techniques to probe them.	4
1.3	Plasmonic sensing approaches to study single molecules.	7
1.4	Optical microcavity based sensing of single molecules.	9
1.5	Representation of the sensor system presented in this thesis.	11
2.1	Photograph of the whispering gallery in the Temple of Heaven, Beijing, China. Photograph by Steve Langguth©.	14
2.2	A simple geometric optics representation of a whispering gallery resonance.	15
2.3	WGM radial profile and mode field distributions in a spherical resonator.	16
2.4	WGM spectra in spheroidal resonators and Quality factor of WGMs.	18
2.5	Evanescent field decay of WGMs in the host medium.	19
2.6	Illustration of the WGM shifts introduced by single nanoparticles.	20
2.7	Mode splitting in WGMs due to a single scatterer.	22
2.8	Detection limits using the frequency shift of a WGM resonator based on thermorefractive and shot noise.	23
2.9	Part of the stained glass window Rosace Nord in the Cathédrale Notre-Dame de Chartres, Paris, France. Photograph by Eusebius (Guillaume Piolle)©.	24
2.10	Schematic illustration of the excitation of the LSPRs in sub-wavelength metallic nanoparticles.	25
2.11	Wavelength dependent permittivity and polarizability of gold.	26
2.12	Intensity enhancement and extinction spectrum of a gold nanosphere.	27
2.13	Intensity enhancement and extinction spectra of rod-shaped gold nanoparticles.	29
2.14	Shift of the plasmonic resonance of a rod shaped particle of aspect ratio 3.5 and diameter 10 nm upon a $\Delta n = 0.005$ change in host refractive index.	29

2.15	Sensing using a combined WGM-plasmonic sensor.	30
3.1	Schematic of the experimental setup for studying single molecules using a WGM-plasmonic sensor.	33
3.2	Schematic of the setup for the fabrication of the resonators	34
3.3	Schematic of a microsphere resonator evanescently coupled via a prism and the WGM transmission spectrum obtained.	35
3.4	Wiring diagram and acquisition of the WGM spectra.	36
3.5	Circuit diagram and acquisition of WGM resonance using a PDH lock.	37
3.6	Data analysis script to characterize single-molecule events.	38
3.7	Sketch of the standard protocol of single-molecule experiments using the opto-plasmonic sensor.	40
4.1	Interaction of single gold nanoparticles with a WGM.	43
4.2	Dependence of the WGM shifts on the polarizability of single nanoparticles.	45
4.3	Binding of gold nanoparticles to the WGM.	46
4.4	Binding of single-molecules to the sensor.	47
4.5	Hybridization kinetics of ssDNA monitored using the sensor.	50
4.6	Distributions of various parameters extracted from the single-molecule events obtained from the hybridization of ssDNA.	51
4.7	Dependence of the various event properties on concentration of COMP22M3.	52
5.1	Schematic of the coupling of light into the WGM and the cross coupling of clockwise (CW) and counter-clockwise (CCW) modes due to the presence of surface scatterers.	56
5.2	Magnetic field intensity distributions of disk resonators with gold nanoparticles near the resonator surface.	58
5.3	Sketch of the unresolved mode split and the corresponding direction of shift of the WGM resonance wavelength and the linewidth depending on the interaction of small sub-kDa molecules with nanoparticle I or II, respectively.	59
5.4	Experimentally measured shift of the WGM lineshape upon binding of Dithiobis(C2-NTA molecules) to the plasmonic gold nanorods attached to the WGM.	60
5.5	Comparison of the magnitude of the shifts in $\Delta\lambda$ and κ and position sensing using the ratio of the shifts.	61
6.1	Schematic representation of cavity ring-up spectroscopy (CRUS).	64

6.2	Measured WGM spectrum with side-bands at 377 MHz and the corresponding error signal.	65
6.3	Measurement of the background fluctuations of the WGM resonance position in ultrapure water.	66
6.4	Interaction of gold nanorods with the WGM measured using the PDH error signal.	67
7.1	Representation of the Molecular mechanical rate theory (MMRT).	70
7.2	Representation of S135c MaL and comparison with the wildtype enzyme.	72
7.3	Diffusion interaction of S135C MaL with the gold nanorod surface.	73
7.4	Binding of the S135C MaL to the gold nanorod surface.	74
7.5	Simulation setup for the molecular dynamics simulations of S135C MaL.	75
7.6	Molecular dynamics simulations of S135C MaL on a gold $\langle 111 \rangle$ surface.	76
7.7	Plots of the sensor signals at various steps of experiment, before and after binding of the enzyme to the sensor.	77
7.8	Survivor functions of time between events and event duration.	78
7.9	Proposed mechanistic scheme of the catalytic reaction.	78
7.10	Temperature dependence of the event heights.	79
7.11	Temperature dependence of the enzymatic rates.	80
B.1	Instability of nanorods attached on the resonator in the presence of high amounts of a surfactant such as SDS.	90

List of Tables

3.1	Immobilization of nanorods with different surface functionalizations, and their pros and cons.	41
4.1	Sequences of DNA oligomers used in our experiments. The DNA oligos were purchased lyophilized from Eurofins Genomics Germany GmbH.	49
7.1	Parameters extracted from fits to (7.2) for the temperature data shown in Figure 7.11.	80

Chapter 1

Introduction

Single-molecule techniques are revolutionizing biology. Single-molecule techniques such as current measurements across a nanopore (Oxford Nanopore Technologies, Oxford, UK) and single-molecule fluorescence microscopy (Illumina Inc., San Diego, USA) are already available as commercial products and enabling the study of biology at unprecedented resolution and throughput. Super-resolution microscopy with techniques based on photoactivated localization microscopy (PALM),¹ stochastic optical reconstruction microscopy (STORM),² and stimulated emission depletion (STED)³ and many variants⁴ have started to provide previously unattainable insights into protein folding, DNA sequencing, enzyme kinetics, and cellular function. In the domain of optics, advancements in the fields of nanophotonics, laser technology and micro/nano fabrication has resulted in a cascade of single-molecule sensing technologies that do not require fluorescent labelling of molecules. This thesis presents the development of one such single-molecule technique based on the combination of optical whispering gallery modes (WGMs) and plasmonic nanoparticles.

This chapter provides an introduction to the work presented in this thesis. The chapter is organized as follows. Firstly, a motivation for developing single-molecule sensors is presented. Secondly, an introduction to proteins as a class of molecules with dynamics in space and time that would benefit from the single-molecule analysis is presented. Thirdly, the state-of-the-art techniques of studying proteins over various spatial and temporal scales are discussed. Fourth, the state-of-the-art plasmonic and microcavity based sensors that have achieved single-molecule sensitivity are described in brief. Finally, an overview of the sensor system established in this thesis is presented and the major outcomes are listed.

1.1 Why single-molecules?

The modern scientific and quantitative form of studying chemical reactions is at least a century old. The unit of measurement in physical chemistry is a mole, where 1 mole is approximately 10^{23} molecules. Typical experiments involve using analyte concentrations in the range of nM – mM, that is, 10^{14} – 10^{20} molecules. The physics of these reactions can be studied

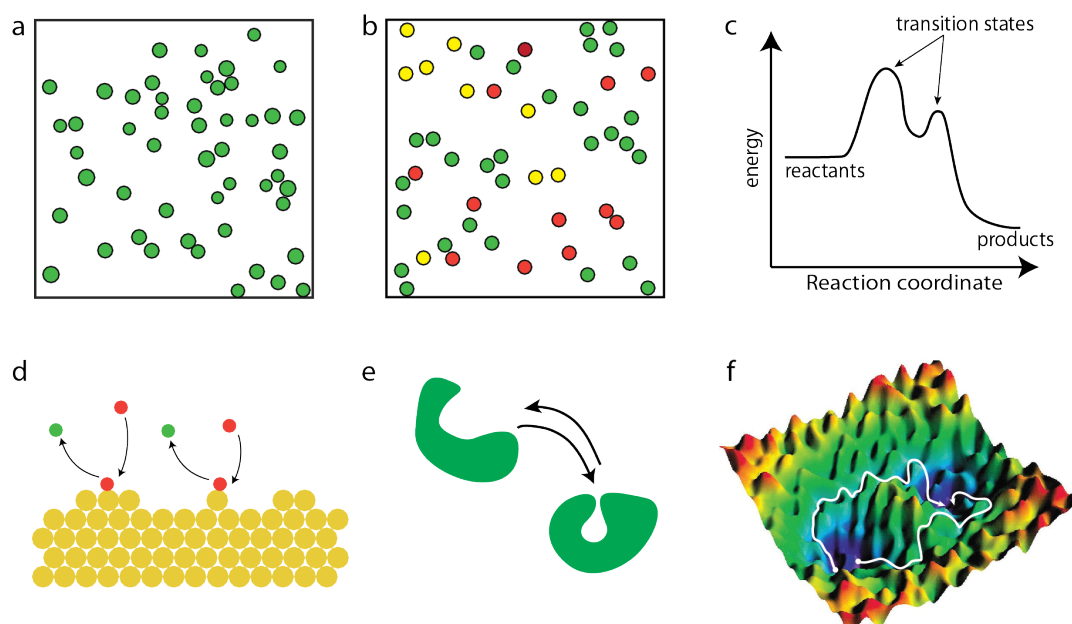


Figure 1.1. Examples of domains where single-molecule measurements are useful. (a) A representation of molecular heterogeneity. In real systems, especially biological, there is considerable variation among individual macromolecules of the same species. (b) A schematic representation of molecular sub-populations. In many systems, different molecules of the same species can exist in different states forming sub-populations of molecules. (c) A schematic of a two-state transition reaction. The reactants have to cross two energy barriers to form products. Studying such reactions are greatly benefited by single-molecule techniques. (d) A schematic of non-uniform kinetics in chemical reactions. Reactions with the same reactants in almost identical conditions can have very different rates, depending on local environment. (e) A schematic of molecular mechanics of macromolecules like large polymers or proteins. Single-molecule studies simplify the study of mechanical and thermodynamic behaviour of these motions. (f) A schematic representation of reaction having a "rough" energy landscape where reactions can take multiple paths. Single-molecule experiments can help identify the probability for a reaction to explore certain paths and study 'rare' events. Image adapted with permission from Dellago and Bolhuis⁵ Copyright 2007 Springer Publishing Group.

by defining ensemble properties such as entropy and temperature. These 'ensemble' or 'bulk' methods work extremely well for capturing the physics of reactions involving simple molecules containing tens to hundreds of atoms in most cases. However, in the regime of macromolecules such as synthetic polymers, DNA, RNA, proteins, and enzymes containing tens to hundreds of thousands of molecules, these ensemble studies are inadequate to provide a fundamental physical picture. By averaging over the ensemble of molecules, the information on the heterogeneity of the sample becomes inaccessible. Another regime where ensemble studies fall short is reactions on surfaces such as metal layers acting as catalysts or electrodes, lipid bilayers, and cell membranes. Both these regimes are critical in modern science. Understanding polymers, biomacromolecules, and reactions on surfaces are key for industrial applications, health, and research. These are some key areas where single-molecule studies can help bridge the gap between theory and experiments. Figure 1.1 shows sketch representations of some domains where single-molecule experiments are useful.

A seemingly homogeneous sample of a macromolecule, although chemically identical, can have considerable variation in its function due to variations in the 3D structure and dynamics of individual molecules. The sketch in Figure 1.1a illustrates this using various green circles where the color indicates the chemical homogeneity, and the varying sizes indicating heterogeneity in the organization. Alternatively, as represented in Figure 1.1b molecular sub-populations could be formed (different colors) which may be spatially localized, for example, distribution of various proteins within cells. Studying these individual or small population variations in molecules requires the ability to visualize individual molecules. Reactions involving biomolecules and reactions on surfaces often go through multiple transition states where the rate-limiting step is often difficult to identify as sketched in Figure 1.1c. Catalytic reactions at heterogeneous surfaces are influenced by the local environment of the catalytic site resulting in a non-uniform reaction kinetics. For example reactions on the surface of a gold nanoparticle are influenced by the local structure of the gold surface and the presence of ad-atoms as represented in Figure 1.1d. Single-molecule experiments provide a direct way of measuring the kinetics at catalytic surfaces and through different transition states. Most proteins and enzymes undergo large-scale conformational changes during their function (Figure 1.1e). The amplitudes and timescales of these motions are critical to understanding their function. Processes involving biomacromolecules can be represented by an energy landscape picture where a process such as protein folding starts with the unfolded polymer in a high energy state and falls through a funnel-like energy landscape to reach the stable configuration represented by the bottom of the funnel. In some cases, these processes can take multiple paths to reach the lowest energy configuration if the energy landscape is 'rough' as represented in Figure 1.1f. Single-molecule experiments offer a direct method to measure molecular mechanics, the probability of processes to explore certain paths and hence aid in the study of 'rare' molecular events.

1.2 Proteins as dynamic molecules

The previous section provided some key fields where single-molecule experiments prove extremely useful. In this section, we will focus on a particular class of single molecules, proteins. We will look at why proteins are interesting to study at the single-molecule level. Proteins are macromolecules that perform numerous important functions such as catalyzing reactions, transporting molecules, and cellular signaling. Proteins gain their functionality from a complex three-dimensional structure and the ability to change this structure over time. X-ray crystallography has led to the identification of the three-dimensional structure of a large number of proteins to a single-digit Å resolution. A comprehensive database of static protein structures is available via the Protein Data Bank (PDB).⁷ However, proteins are not static. They are in constant motion and can be viewed as sampling a large ensemble of conformations around an average structure due to thermal energy. Moreover, proteins exhibit changes in these conformations on a variety of time scales which is now recognized as key to their functionality. A complete description of proteins requires a multidimensional energy landscape that defines the relative probabilities of the conformational states and the energy barriers between them.⁶ Frauenfelder *et al.* first hypothesized that the functionality of a protein (rebinding of carbon

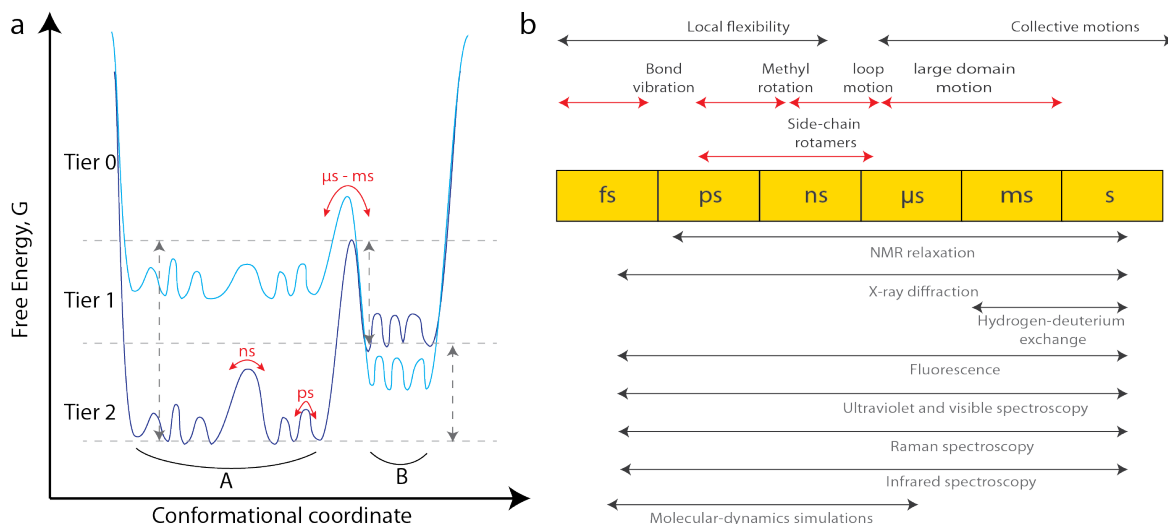


Figure 1.2. (a) One-dimensional cross-section through the energy landscape of a protein showing the hierarchy of dynamics and the energy barriers. (b) Timescale of dynamic processes in proteins and the experimental methods capable of detecting motions in each timescale. Image adapted from Henzler-Wildman *et. al.*⁶ Copyright 2007 Springer Nature

monoxide and oxygen to Myoglobin) can be described by an energy-landscape picture.⁸ Subsequent studies^{9–12} reinforced the energy landscape picture to describe protein function and suggested that both solvent and ligands influence the landscape. The dynamics of proteins are complex involving varied timescales, amplitudes, and direction of the fluctuations. The energy landscape is hence multidimensional and also tied to a particular set of temperature, pressure, and solvent conditions. Henzler-Wildman⁶ classifies protein motions into different tiers (0,1,2) based on their timescales and free energy. Figure 1.2a shows a one-dimensional cross-section through the energy landscape of a protein indicating the hierarchy of protein dynamics and energy barriers. Figure 1.2b shows the timescales of motions and experimental methods capable of detecting fluctuations on each timescale.

1.3 Methods for studying protein dynamics

Various experimental and simulation techniques are available to describe the structure and dynamics of proteins in the last few decades. X-ray crystallography,^{13,14} cryo-electron microscopy (cryo-EM),¹⁵ small-angle X-ray scattering (SAXS),¹⁶ Nuclear Magnetic Resonance (NMR) spectroscopy^{17–20} and mass spectroscopy have provided the bulk of the information regarding the dynamics of proteins often with atomic resolution. However, the above mentioned experimental techniques are ensemble measurement techniques requiring synchronization of millions of molecules. In this section, we will mainly focus on the single-molecule techniques that are now being used to answer questions previously inaccessible by these ensemble methods.

Force spectroscopy using optical or magnetic tweezers and atomic force microscopy²¹ has provided detailed measurements of the elasticity of nucleic acids, measurement of bond energies,

lifetimes, and entire energy landscapes. Single-molecule force spectroscopy, in general, measures the extension of a molecule attached to the force probe when mechanical tension is applied across the molecule. Woodside *et al.*²² provide a detailed guide on the reconstruction of energy landscapes from various types of single-molecule force spectra. The main concern with force spectroscopy is that the natural dynamics of the protein might be hindered due to the external forces applied and the attachment protocols. Hence, alternative techniques to monitor proteins in the native state are sought. The most popular technique in this class is based on the fluorescence from single-molecules.^{23,24} The large range of fluorescent dyes, combined with optimized optics, efficient detectors, and algorithms have made single-molecule fluorescence spectroscopy the method of choice for dynamic studies in the past decade. Additionally, single-molecule Förster resonance energy transfer (smFRET), can accurately measure Å distances allowing characterization of distance over time.²⁵ Single-molecule fluorescence experiments have finally reached a stage where critical molecular and biological questions are being answered. For example, Chung *et al.* recently studied the dynamics of barrier crossing in small α -helical proteins using single-molecule fluorescence experiments.²⁶

Complementary to the experimental methods, computational techniques have been pivotal in understanding protein dynamics. Although experimental methods provide information on the conformation sub-states, an atomic-resolution description of the change from one 'valley in the energy landscape to another' is currently out of experimental reach, due to extremely low probability and short lifetimes of the high energy conformers.⁶ Computation has the key advantage of being capable of describing the position of each atom in a protein over time starting from a known atomic-resolution 3D structure. An accurate description of all transitions can be obtained provided a perfect description of the protein-solvent system is given by the force field (a parameter set describing the potential energy of all atoms).²⁷ Molecular dynamics simulations have evolved as a means of studying protein dynamics with massively parallelized open-source solvers such as NAMD,²⁸ LAMMPS,²⁹ and GROMACS.³⁰ However, even with high computational resources all-atom, long-timescale ($> 1 \mu\text{s}$) simulations of even small proteins is challenging. To overcome this limitation, several simplifications to the force-fields have been developed such as normal mode analysis,³¹ Gaussian network models,³² FIRST (Floppy inclusion and rigid substructure topography),³³ and Gō models.³⁴ D.E. Shaw and co-workers recently designed Anton, a massively-parallel, specialized supercomputer for molecular dynamics simulations³⁵ and reported picoseconds to millisecond dynamics of Human Ubiquitin with all atomic simulations.³⁶ Although computational methods can provide critical insights into protein dynamics, experimental validation is always necessary.

1.4 Plasmonic and optical microcavity single-molecule sensorsⁱ

In the following section, we will look at the state-of-the-art of two relatively recent systems to achieve single-molecule detection capability, namely optical microcavities, and plasmonic nanoparticles. These platforms although not established like fluorescence techniques, show great potential for label-free, real-time, single-molecule sensing over timescales of picoseconds to hours. The work presented in this thesis uses both optical microcavities and plasmonic nanoparticles to develop a sensor system capable of studying single protein dynamics.

Optical microcavities and plasmonic nanoparticles fall in the general category of resonance based sensors. Specific boundary conditions in these systems result in the formation of optical or plasmonic resonances. Similar to a tuning fork, the frequency of the resonances is morphology dependent, that is, dependent on the geometry of the structures, the properties of the material, and the surrounding medium. The interaction of a biomolecule with these resonances results in a change in the resonance spectral properties which can be used to infer details about the interacting species. The amplification of the signal provided by these resonances has enabled the detection down to single molecules. In the optical domain, these resonances can be broadly classified into two main categories, plasmon resonance in metal nanostructures and optical micro- and nano- resonances in dielectric materials. The following sections provide a summary of the state-of-the-art in single-molecule plasmonic,^{37,38} microcavity^{39,40} and optoplasmonic (a combination of plasmonic and microcavity)⁴¹ sensors.

1.4.1 Plasmonic sensing approaches

Localized surface plasmon resonances (LSPRs) are collective oscillations of surface electrons in metal nanostructures such as silver and gold. These oscillations can be directly excited using visible/near-infrared light and lead to extremely high localization of electric fields near the surface of these nanostructures. Interaction of biomolecules with this enhanced field can be used for sensing applications. Although biosensing using plasmonic properties of metal nanostructures has been well established, achieving single-molecule sensitivity has been relatively recent.

Figure 1.3a shows the state-of-the-art techniques for detecting single biomolecules using plasmonic nanostructures. Figure 1.3a shows the work by Zijlstra *et al.*⁴² who achieved single-molecule sensitivity using photothermal microscopy of single gold nanorods. The change in polarizability of the gold nanorod is monitored as a shift in the resonance peak position when a molecule interacts with its near-field (see inset). The plots in Figure 1.3a show the plasmon peak shift measured due to the binding of single streptavidin (53 kDa), antibiotin (150 kDa), and a streptavidin-R-phycoerythrin conjugate (300 kDa) to biotin coated gold nanorods. The plasmon resonance shift sensing was further improved by monitoring the scattering from

ⁱThis section has appeared in part in Subramanian, S., Wu, H.-Y., Constant, T., Xavier, J., and Vollmer, F., “**Label-Free Optical Single-Molecule Micro- and Nanosensors**,” *Advanced Materials* 30(51), 1801246 (2018).

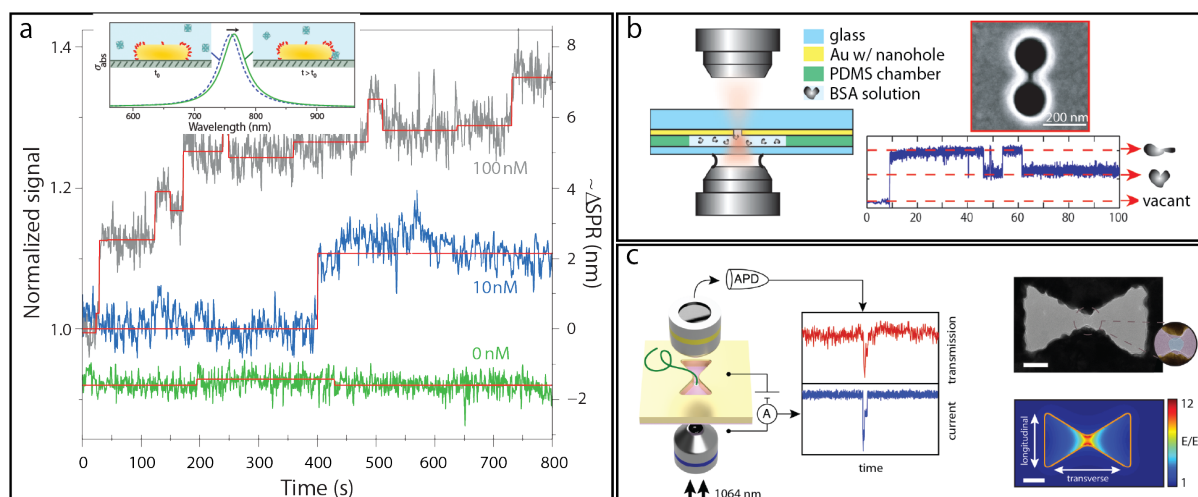


Figure 1.3. Plasmonic sensing of single molecules. (a) Photothermal sensing of single molecules at the tips of plasmonic gold nanorods. Plot shows the time traces of localized surface plasmon shift measured for the binding of streptavidin–R-phycoerythrin conjugate at different concentrations. Inset shows a schematic of the sensing principle based on shift of the LSPR due to the binding of a molecule. Adapted with permission from Zijlstra *et al.*⁴² Copyright 2012, Springer Nature. (b) Double nanohole optical trap for single molecule trapping. (i) Schematic presentation of the setup for trapping single proteins using plasmonic nanohole traps. (ii) An SEM micrograph of the dumbbell shaped nanohole structure milled in a gold film coated on a glass substrate. (iii) Example trace of step events in the transmission signal obtained due to trapping of a single BSA molecule. Adapted with permission from Pang *et al.*⁴³ Copyright 2012, American Chemical Society. (c) Plasmonic nanopore sensing of single molecules. (i) Schematic of the experimental setup for detecting DNA translocation through a plasmonic nanopore. (ii) An TEM micrograph of the plasmonic inverted bowtie structure with a nanohole drilled in its gap. Zoom inset shows a false colored image of the gap. (iii) Normalized electric field distribution of in a bowtie plasmonic nanostructure indicating a 12 fold enhancement of the electric field in the gap. Scale bars are 50 nm. Adapted with permission from Verschueren *et al.*⁴⁴ Copyright 2019, American Chemical Society.ⁱⁱ

hundreds of nanoparticles simultaneously using a dark-field microscopy setup.⁴⁵

Another approach shown in Figure 1.3b uses optical trapping of single proteins in a dumbbell-shaped double nanohole milled into a gold-coated glass substrate. Figure 1.3b,i shows the schematic of the setup. The trapping of the molecule is monitored as a change in the transmission across the plasmonic nanostructure.⁴³ Figure 1.3b, ii shows an SEM micrograph of the double nanohole structure milled on thin gold (Au) film using focussed ion-beam milling. The sub-wavelength scale confinement of light and the corresponding enhancement in the local field-intensity provides the required potential landscape for trapping entities as small as single proteins. Pang and Gordon achieved trapping of single bovine serum albumin (BSA) proteins using this method (Figure 1.3b, iii). Once the protein is trapped additional information on the protein could be obtained from the fluctuations of the transmitted light due to the thermal motion of the protein in the trap. Wheaton *et al.* used the electrostriction (restoring force due to charge displacement in an external electric field) force to excite low frequency (GHz) vibrational modes in the protein using an amplitude-modulated beam.⁴⁶ The increased fluctuation of the molecule in the optical trap is used to obtain the acoustic Raman spectra of the molecule.

Yet another recent approach combines nanopore sensing with plasmonic nanostructures to provide multiple detection channels.^{44,47} In this technique a bow-tie structure is fabricated on a gold-coated substrate using electron-beam lithography (see Figure 1.3c,i). The bow-tie structure provides a 12-fold signal enhancement as shown by the simulation in Figure 1.3c,ii. For creating the nanopore, a hole is drilled in the center of the bow-tie antenna using TEM drilling. The experimental schematic is as shown in Figure 1.3c,iii. The transmission of light across the antenna is monitored using a high NA objective, and the current across the nanopore is monitored simultaneously. The translocation of a λ -DNA across the nanopore results in signals in both the optical and current channels. The signals in the optical channel arise due to the change in transmission across the antenna due to a shift of the plasmonic resonance. The signals in the measured current arise due to a change in the resistance across the membrane. Combining the two different modes of single-molecule detection will overcome the limitations of each. Mainly, for nanopore sensing, the often fast uncontrolled transport of small molecules across the membrane results in low signal-to-noise ratio (SNR). The limited temporal response of the high-gain detectors required to obtain these signals reduces the SNR and prevents detection of small molecules.⁴⁸ The use of bow-tie nanostructures provides ample readout times by optical trapping of the molecules in the plasmonic hotspots.⁴³ On the other hand, approaches based on plasmonic nanostructures have long wait times or require high molecular concentrations^{49–51} as they depend on free diffusion for molecules to reach the sensing site. The electrophoretic transport of molecules due to the voltage bias in nanopore sensing overcomes this limit enabling smaller wait times and detection of lower concentrations.

1.4.2 Optical microcavities

Optical microcavities are resonant structures in dielectric materials typically with the dimensions of micrometers. Due to the low losses in the dielectrics, optical microcavities can have extremely high-quality factors Q (defined as the ratio of the energy stored by the energy dissipated per oscillation of the electromagnetic field). They also have relatively low mode volume V due to their small sizes. Here, Q quantifies the temporal confinement of light, whereas, V quantifies the spatial confinement. The ratio of Q/V is proportional to the enhancement provided by the microcavity to detect molecules. Typically, these cavities are inserted into a solution containing the analyte of interest, and the interaction of the molecules with the evanescent field on the microcavities results in a change in the optical spectrum of the cavities. The changes in the spectra are then used to infer about the molecules interacting with the cavity.

Figure 1.4 shows three different schemes using optical microcavities that have achieved single-molecule detection sensitivity. Figure 1.4a shows an optical WGM microcavity sensor enhanced by a plasmonic nanorod that has been utilized to studying the conformational dynamics of single enzymes. Figure 1.4a,(i) shows the schematic of the optical setup. A spherical glass microcavity placed in the sample chamber with a gold nanorod attached on its surface acts as the sensor. Figure 1.4a,(ii) shows an illustration of a Pfu polymerase enzyme attached to a gold nanorod. The conformational movements on the enzyme and its interaction with its ligands translated into a shift of the resonance frequency of the WGM. This is observed as signal peaks in the

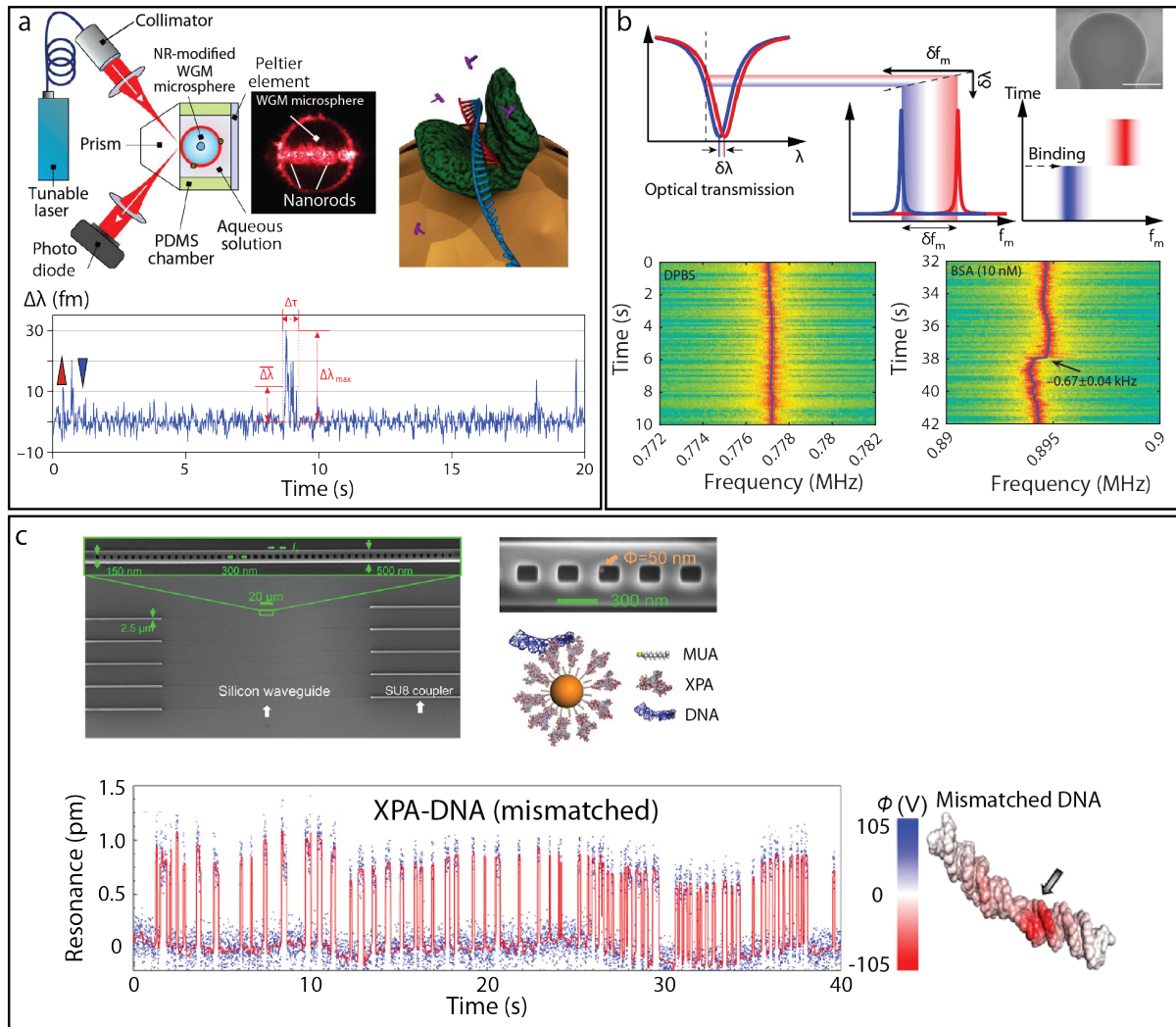


Figure 1.4. Optical microcavity based sensing of single molecules. (a) A single-molecule sensor based on a plasmonic nanoparticle enhanced whispering-gallery mode resonator. (i) Schematic of the setup to excite WGMs in spherical microcavities. (ii) Illustration of an enzyme on the sensor. (iii) Typical single-molecule signals obtained from the sensor. Adapted from Kim *et al.*⁵² ©The Authors, some rights reserved; exclusive licensee AAAS. Distributed under a CC BY-NC 4.0 License. (b) Single-molecule sensing using optomechanical coupling in a spherical WGM resonator. (i) Schematic of the sensing principle. Optomechanical coupling results in a large shift in the narrow mechanical resonance compared to the relatively small shift in the optical resonance. (ii) Spectrogram of the background in phosphate buffered saline (PBS). (iii) Spectrogram of the resonance indicating a binding step for the binding of a single BSA molecule on the sensor. Reprinted with permission from Yu *et al.*⁵³ under the CC-BY-4.0 licence 2016 Springer Nature (c) Single-molecule sensing in a photonic crystal nanocavity enhanced by spherical gold nanoparticle. (i) SEM micrograph of the photonic crystal nanocavity. (ii) A zoom-in on the SEM micrograph showing a gold nanoparticle within the cavity. (iii) Typical single molecule DNA hybridization signals obtained using the sensor. Adapted from Liang *et al.*⁵⁴ ©The Authors, some rights reserved; exclusive licensee AAAS. Distributed under a CC BY-NC 4.0 License.

time traces of the position of the WGM frequency as shown in Figure 1.4a,(iii). These signals are measured at various temperatures to estimate the rate and amplitude of the conformational

dynamics of the enzyme.³⁹

Figure 1.4b shows another scheme using optical WGMs. In this method, instead of a plasmonic enhancement, the optomechanical coupling of a WGM to the mechanical modes of the resonator is used for sensing.⁵³ As shown in Figure 1.4b,(i) a small shift in the WGM resonance due to the binding of single biomolecules translated into a much larger shift of the mechanical resonance frequency due to the much high-quality factor of the mechanical resonance. Using this technique, Yu *et al.* could monitor the binding of single BSA molecules to the glass resonator surface as shown by the step changes in the spectrogram in Figure 1.4b,(iii).

Finally, resonant structures based on the periodic variation of refractive index on a substrate known as Photonic Crystal (PhC) micro or nanocavities have been employed for single-molecule detection. In a PhC, the periodic structure leads to a constructive and destructive superposition of light resulting in only certain allowed frequencies to propagate within the structure. Breaking the symmetry of PhC in a local region allows confinement of light within the region resulting in resonant structures. Fabrication of these structures in low loss dielectric, using common CMOS techniques has enabled the creation of high Q (typically 10^6) and ultra-low mode volume \mathcal{V} ($\sim \text{nm}^3$) resonators. An example of such a structure in 1D is shown in Figure 1.4c),i.⁵⁴ Combining the PhC nanocavity with the enhancement from a gold nanosphere, Liang *et al.* have demonstrated single-molecule sensitivity. They were able to detect single protein-DNA dynamics with and without the use of fluorescent labels (Figure 1.4c),(ii)) and discern the effects of the fluorescent label on the dynamics.

1.5 Thesis outline

In this thesis, we develop a single-molecule sensor system with the final aim of studying the large scale (μs - ms) conformational changes in proteins. Figure 1.5 shows an illustration of the sensor system. The sensor is composed of a spherical whispering gallery mode (WGM) cavity with a plasmonic nanorod attached to its surface. The binding and interaction of single proteins and ligands on the surface of the gold nanoparticle are translated into a shift in the resonance frequency of the optical whispering gallery mode. Monitoring this shift over time provides the kinetics of the interactions of single molecules. Kim *et al.*⁵² recently reported a WGM based sensor that was capable of monitoring signals from the conformational dynamics of a DNA-polymerase. In the work of Kim *et al.*, the sensor system was limited in the time resolution to 20 ms. Additionally, the enzyme was immobilized by adsorption on the sensor which might affect the dynamics of most enzymes.

Here, we overcome the above limitations by implementing new technical and biochemical schemes. Specifically, we have implemented schemes to obtain the sensor signals with a high time resolution (down to μs) with the possibility to even achieve ns signal acquisition. The improved time resolution is obtained without any additional increase in the noise. Hence, the new sensor with the improved time resolution is capable of monitoring single-molecule events at the μs timescale. We also discuss schemes for reducing the sensor noise to enable higher signal-to-

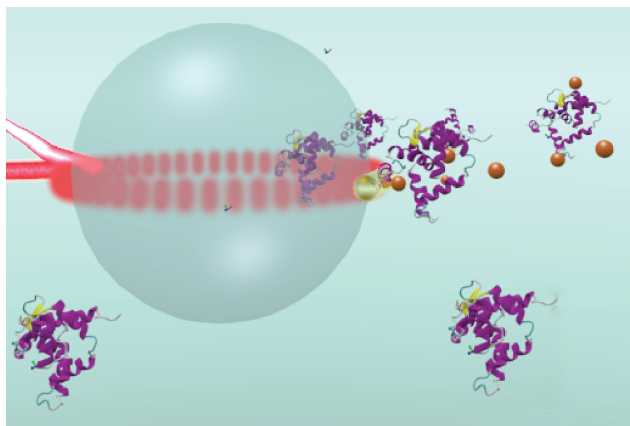


Figure 1.5. Representation of a dielectric sphere with optical whispering gallery modes. The protein to be observed is bound to a gold nanoparticle attached to WGM. Image not to scale

noise ratios at these timescales. We implement a split-mode based sensing technique to detect single molecules which provides robust long-term detection of the molecules. Further, we have implemented new specific immobilization strategies for single-enzymes that enable acquisition of repeatable signal-patterns from conformational fluctuations of single enzymes. In this thesis, we also explore the fundamental physics of the sensor system to provide a better understanding of the sensing mechanism.

The thesis outline is as follows: **Chapter 2** provides the theoretical background of the sensor system presented in this thesis. First, the theory of optical whispering gallery modes in spherical dielectric geometries and the principles of biosensing using WGMs are described briefly. Then, the theory of electric field enhancement by plasmonic nanoparticles is described and the principle refractive index sensing based on the near-field enhancement is explained. Finally, the WGM-plasmonic hybrid sensor is introduced and the origin of its exceptional sensitivity is explained.

Chapter 3 provides the aspects of the experimental design for the sensor system presented in this thesis. The aspects such as the experimental setup, circuit, and wiring diagrams, fabrication of resonators, data acquisition and analysis, and the typical experimental protocol are explained in detail.

Chapter 4 explores the mechanism of the WGM based sensor. Specifically, it is shown that the WGM shifts do track the polarizability⁵⁵ of the nanoparticles on its surface using gold nanoparticles of different polarizabilities. The origin of both positive and negative shifts in WGM resonance frequency due to the interaction of gold nanoparticles with a WGM is described. The WGM-plasmonic hybrid sensor is presented and the ability of the sensor to detect small single molecules as shifts in the WGM resonance frequency is shown. The hybridization kinetics of DNA oligonucleotides is used as a test system to establish the sensor system.

Chapter 5 explores an alternate mechanism for detecting single molecules using a WGM-plasmonic hybrid sensor. This chapter, in part, has been the subject of a recent publication in Applied Physics Letters.⁵⁶ The unequal splitting of standing wave modes caused due to interaction of small sub-kDa molecules with plasmonic nanorods on a WGM cavity surface translate into effective shifts in the WGM linewidth. This occurs when multiple nanorods are

attached to the WGM resonator and the splitting of the standing wave modes are unresolved. Sensing of single molecules using the linewidth enables a robust mechanism for sensing that is insensitive to long-term noise sources.

Chapter 6 introduces the concept of Pound-Drever-Hall locking of the laser to the WGM cavity resonance for high bandwidth and low-noise acquisition of the WGM spectra. Using the PDH lock-in technique, the diffusion interaction of small plasmonic gold nanorods with a WGM microcavity is monitored. Signals with interaction duration as small as 15 μ s and amplitude less than 1 fm (3 times lower noise than the traditional laser scanning technique) could be monitored. The PDH lock-in technique thus enables the detecting of fast events that are of interest in biology such as the conformational fluctuations of enzymes.

Chapter 7 applies the WGM-plasmonic hybrid sensor and the PDH lock-in measurement technique to study the thermodynamics of enzyme catalysis at the single-molecule level. A model enzyme, Mall, is mutated to obtain a solvent-exposed thiol group. The enzyme is then immobilized on the sensor surface and the turnover of an artificial substrate 4-Nitrophenol- β -D-glucopyranoside (pNPG) is monitored at various temperatures. The catalytic rate of the enzyme is shown to have a strong negative curvature that provides support for the recently hypothesized macromolecular rate theory (MMRT).⁵⁷ The protein expression and ensemble experiments were performed by Hannah Jones in the lab of Dr. Christopher Pudney at the University of Bath. The results presents show that the WGM-plasmonic hybrid sensor can be applied to solve actual problems in biochemistry for the first-time.

Chapter 8 concludes the thesis. Key results are summarized and an outlook for future work is provided.

Appendix A-C provide more detail on various aspects of the theory, sensor assembly, and simulations performed in this thesis.

Chapter 2

Theory

This chapter provides the necessary theoretical background to understand the functionality of the sensor system presented in this thesis. The chapter is organized as follows. First, the theoretical framework for obtaining whispering gallery modes (WGMs) in spherical resonators is presented. The main focus of this section will be on the important parameters to consider when using WGMs for sensing applications. Next, the theoretical framework for exciting surface plasmon resonances (SPRs) in metal nanoparticles is provided. Again, the focus of this section will be on the key parameters for sensing applications. Finally, the hybridized WGM-plasmon system is considered and the parameters for sensing applications are explored.

2.1 Optical whispering gallery modes

Optical whispering gallery modes are resonances formed in dielectric geometries with circular symmetry such as disks,⁵⁸ rings,⁵⁹ torroids,^{60–62} bottles,⁶³ cylinders,⁶⁴ and spheres.⁶⁵ The term whispering gallery mode was first used in the context of the guiding of sound waves in the dome of St. Paul's Cathedral in London by Lord Rayleigh.^{66,67} He observed that whispers could be heard between the far ends of the dome due to the nearly lossless guiding of certain frequencies of sound waves. This guiding of sound waves is attributed to the formation of acoustic resonances by constructive interference of sound waves. Figure 2.1 shows a photograph of the acoustic whispering gallery at the Temple of Heaven, Beijing, China (photo courtesy of Steve Langguth) as an example. Similarly, in the optical domain, resonances occur due to the constructive interference of light that undergoes multiple total internal reflections at the boundary of a curved dielectric. The concept is illustrated in Figure 2.2. For the sake of simplicity and relevance to our work, a spherical micro-resonator geometry is considered. Total internal reflection occurs for a ray of light propagating inside a sphere of radius $a \gg \lambda$ with an angle of incidence $i > i_c$, where i_c is the critical angle for total internal reflection. Spherical symmetry makes all further incidence angles the same, creating consecutive reflections. If the ray strikes the sphere at near glancing angles $i \approx \pi/2$, it propagates a distance equal to the perimeter of the sphere, that is, $2\pi a$. If one round trip of light equals an integer multiple l of

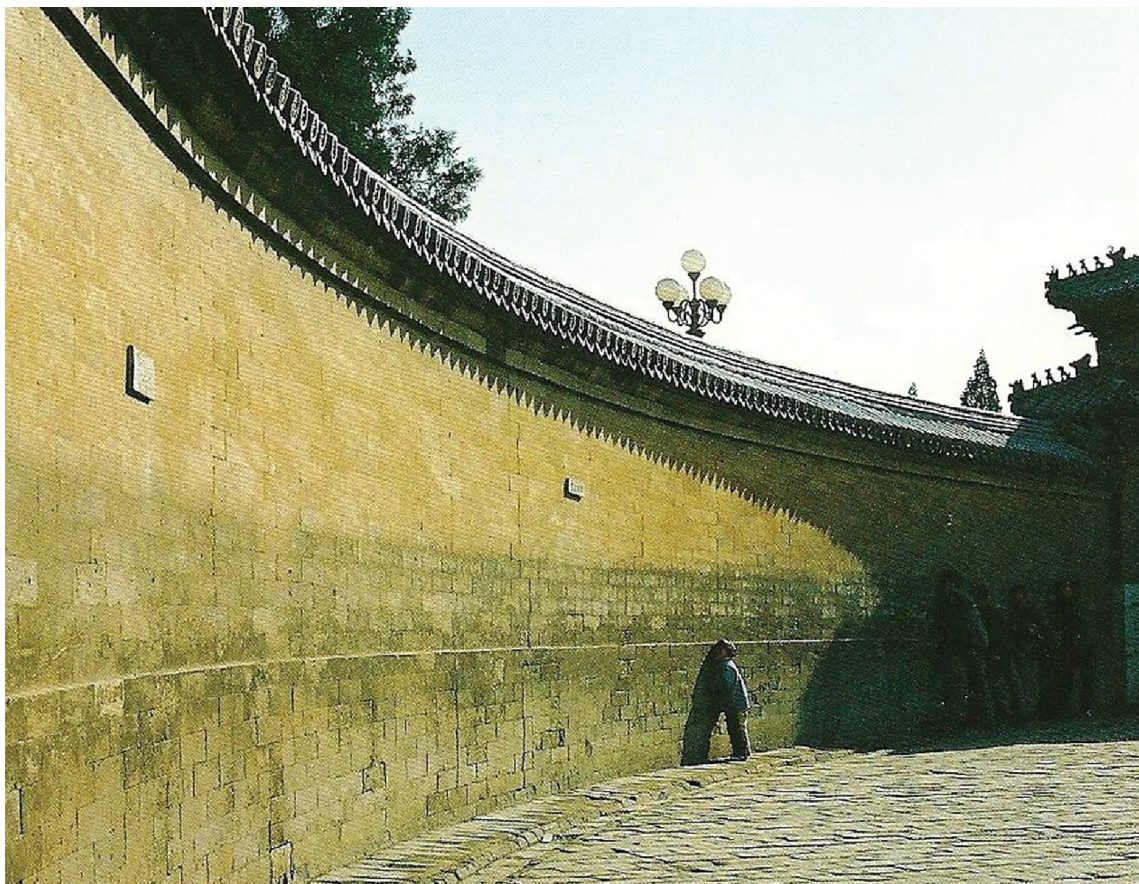


Figure 2.1. Photograph of the whispering gallery in the Temple of Heaven, Beijing, China. Photograph by Steve Langguth©.

the wavelength of light in the sphere medium, then constructive interference occurs. Therefore, the condition for resonance is $2\pi a = l \frac{\lambda}{n_s}$, see Figure 2.2. Here, n_s is the refractive index of the sphere material.

2.1.1 Whispering gallery modes in spherical resonators

Whispering gallery modes in spherical resonators can be described by the solutions of the vectorial Helmholtz equation (see Appendix A for more details). The solutions to the electric and magnetic fields within and outside the resonator can be divided into two types according to the polarization of the oscillation, *transverse electric* (TE) where $\mathbf{r} \cdot \mathbf{E} = 0$ and *transverse magnetic* (TM) where $\mathbf{r} \cdot \mathbf{B} = 0$, where \mathbf{E} and \mathbf{B} are the electric and magnetic fields, respectively

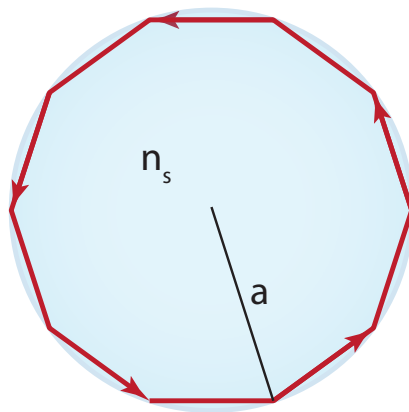


Figure 2.2. A simple geometric optics representation of a whispering gallery resonance.

and \mathbf{r} is a vector in space. The fields for both polarizations can be expressed as,⁶⁸

$$\mathbf{E}_{\text{lm}}^{\text{TE}}(\mathbf{r}) = E_0 \frac{f_l(r)}{k_0 r} \mathbf{X}_1^{\text{m}}(\theta, \phi) \quad (2.1a)$$

$$\mathbf{B}_{\text{lm}}^{\text{TE}}(\mathbf{r}) = \frac{E_0}{ic} \left(\frac{f_l'(r)}{k_0 r} \mathbf{Y}_1^{\text{m}}(\theta, \phi) + \sqrt{l(l+1)} \frac{f_l(r)}{k_0^2 r^2} \mathbf{Z}_1^{\text{m}}(\theta, \phi) \right) \quad (2.1b)$$

$$\mathbf{E}_{\text{lm}}^{\text{TM}}(\mathbf{r}) = \frac{E_0}{N^2} \left(\frac{f_l'(r)}{k_0 r} \mathbf{Y}_1^{\text{m}}(\theta, \phi) + \sqrt{l(l+1)} \frac{f_l(r)}{k_0^2 r^2} \mathbf{Z}_1^{\text{m}}(\theta, \phi) \right) \quad (2.1c)$$

$$\mathbf{B}_{\text{lm}}^{\text{TM}}(\mathbf{r}) = -\frac{iE_0}{c} \frac{f_l(r)}{k_0 r} \mathbf{X}_1^{\text{m}}(\theta, \phi) \quad (2.1d)$$

where, $N = n_s/n_m$ is the relative index of refraction, c is the speed of light in vacuum, $\mathbf{X}_1^{\text{m}}, \mathbf{Y}_1^{\text{m}}, \mathbf{Z}_1^{\text{m}}$ are the vectorial spherical harmonics, and $f_l(r) = \psi_l(Nk_0 r)$ for $r < a$ and $f_l(r) = A\psi_l(k_0 r) + B\chi_l(k_0 r)$ for $r > a$. Here, ψ_l and χ_l are solutions to the Ricatti-Bessel equation. The vectorial spherical harmonics provide the angular distribution of the fields, while the Ricatti-Bessel functions provide the radial component. The number l is an integer value that provides the order of the spherical harmonic Y_l^m and is termed the mode number. The number m can take $2l+1$ integer values from $-l$ to l and is termed the azimuthal mode number.

Modal equations and eigenfrequencies

Equations (2.1a) to (2.1d) provide the field distributions for TE and TM polarizations within and outside the sphere. The fields within and outside the sphere are related via the continuity relations for linear isotropic media,

$$\mathbf{E} \times \hat{r} = 0 \quad (2.2a)$$

$$\mathbf{B} \cdot \hat{r} = 0 \quad (2.2b)$$

$$\epsilon \mathbf{E} \cdot \hat{r} = \rho \quad (2.2c)$$

$$\frac{1}{\mu_0} \mathbf{B} \times \hat{r} = \mathbf{j}. \quad (2.2d)$$

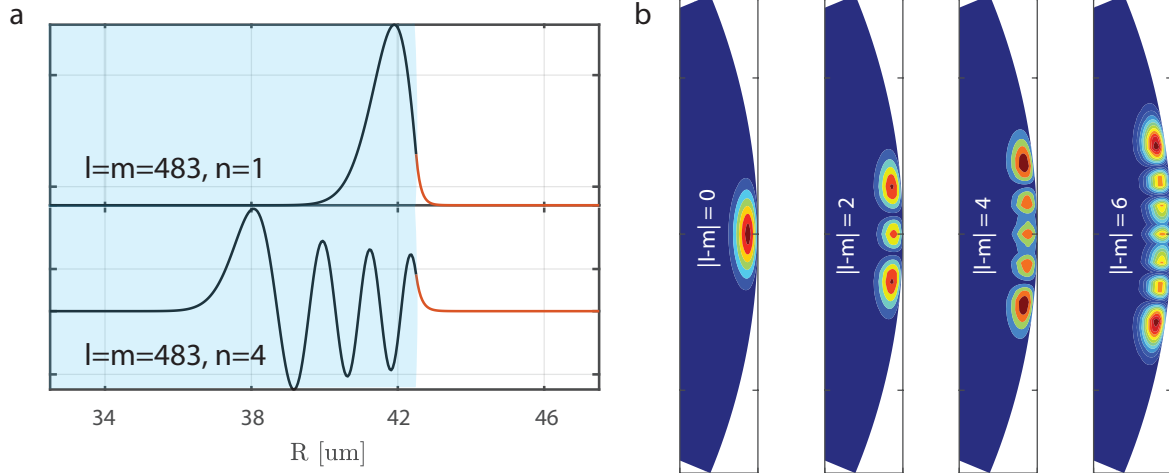


Figure 2.3. WGMs in a spherical resonator with radius $a = 42.5 \mu\text{m}$ and $l = 483$. (a) Radial profile of a WGM mode with $m = l, n = 1$ and $m = l, n = 4$ with the corresponding potential functions. (a) Mode field distributions for WGMs of the first few azimuthal orders.

Equations (2.1a) to (2.1d) and (2.2) assuming no free charges ($\rho_0 = 0$) and no free currents ($\mathbf{j} = 0$) provide the equations for the position of the resonances,

$$A^{TE} \psi_l(ka) + NB^{TE} \chi_l(k_0a) = 0 \quad (2.3a)$$

$$A^{TE} \psi_l'(ka) + B^{TE} \chi_l'(k_0a) = 0 \quad (2.3b)$$

$$A^{TM} \psi_l(ka) + B^{TM} \chi_l(k_0a) = 0 \quad (2.3c)$$

$$A^{TM} \psi_l'(ka) + NB^{TM} \chi_l'(k_0a) = 0. \quad (2.3d)$$

Equations (2.3) have non-trivial solutions if and only if the determinant is zero and hence they provide

$$P \frac{\psi_l'(ka)}{\psi_l(ka)} = \frac{\chi_l'(k_0a)}{\chi_l(k_0a)} \quad (2.4)$$

where the index $P = N$ for TE modes and $P = 1/N$ for TM modes. Equation (2.4) is called the modal equation and relates the wave number k to the radius a . The modal equations provide a possible infinite set of solutions for the WGMs. Hence, another index n has to be defined to identify the number of the solution where $n \in \mathbb{N}$, the set of natural numbers. The set of numbers l, m, n and P fully define whispering gallery modes in spherical resonators. For obtaining the field distribution inside spherical WGMs, the roots of the modal equations have to be first obtained, typically using numerical methods. Analytic solutions have however been attempted in literature. For large mode index l , Lam et al.⁶⁹ developed an approach by approximating the Bessel functions and their derivatives as an asymptotic series with the use of Airy functions. For large sphere radii, the eikonal approach has also been used to narrow the search for the solutions. Figure 2.3a plots the radial dependence of the electric field for mode numbers $l = m = 483$ and $n = 1, 4$. The plot shows the evanescent tail (orange) extending for about 100 nm in the medium outside the resonator. This evanescent field is important in using WGMs for sensing applications as will be seen later. Figure 2.3b plots the electric field distributions for different mode numbers l and m obtained using a numerical solver developed by Balac and Féron.⁷⁰

It has to be noted that (2.4) has no dependence on the azimuthal mode number m and hence the solutions are degenerate over this index for perfectly spherical resonators. However, in practice resonators always have a small eccentricity and hence the degeneracy over this index is broken. For prolate or oblate spheroids with a small eccentricity $e = (r_p - r_e)/a$, where r_p and r_e are the polar and equatorial radii, respectively, the new solutions can be obtained as,⁶⁸

$$Nx_{l,m,n}^P \approx Nx_{l,n}^P \times \left[1 + \frac{e}{3} \left(1 - 3 \frac{l - |m|}{l} \right) \right] \quad (2.5)$$

where $x = 2\pi a/\lambda$ is the size parameter that provides the eigenfrequencies of the WGM and l, m, n and P are as defined above. The degeneracy over the sign of m remains however, that is counter-propagating modes are degenerate. This degeneracy is lifted when scatterers are attached to the resonator. The phenomenon of the scatter-based lifting of degeneracy can also be used for sensing applications as shall be seen in the following sections.

Cavity spectrum, quality factor, and mode volume

Figure 2.4a shows the typical WGM spectra obtained by scanning a tunable laser over a small bandwidth around the WGM resonance frequency. Light couples from the waveguides (TIR at a prism surface in this case) at the WGM resonance frequency forming Lorentzian dips. Since the resonator deviates slightly from a perfect sphere, the different azimuthal orders m are non-degenerate and can be resolved in the spectrum. The cavity spectrum in the frequency domain is given in the form of a Lorentzian function

$$P(\omega) = P \frac{(\kappa/2)^2}{(\omega - \omega_0)^2 + (\kappa/2)^2}, \quad (2.6)$$

where P is the power, κ is the full-width-at-half-maximum (FWHM) of the cavity resonance spectrum, and ω_0 the resonance frequency.

The parameter termed quality factor Q can then be defined as

$$Q = \frac{\omega_0}{\kappa} = \omega_0 \tau, \quad (2.7)$$

where τ is the cavity lifetime. Hence, Q quantifies the temporal confinement of light in the resonator. The intrinsic quality factor of the resonator is composed of various contributions due to losses from many processes and can be written as,

$$Q_{int}^{-1} = Q_{mat}^{-1} + Q_{surf}^{-1} + Q_{scat}^{-1} + Q_{rad}^{-1}. \quad (2.8)$$

Here, Q_{int} is the intrinsic quality factor of the resonator, Q_{mat} describes the intrinsic material absorption, Q_{surf} surface absorption losses, Q_{scat} describes the scattering losses (such as due to imperfections in the form of surface roughness) and Q_{bend} describes bending loss (or radiation loss or tunnel loss). For a perfectly smooth silica microsphere, the contributions from Q_{mat} (low absorption losses in the material) and Q_{scat} (no surface roughness) can be ignored. The major contributors for the resonator losses are then from the absorption of the surrounding medium

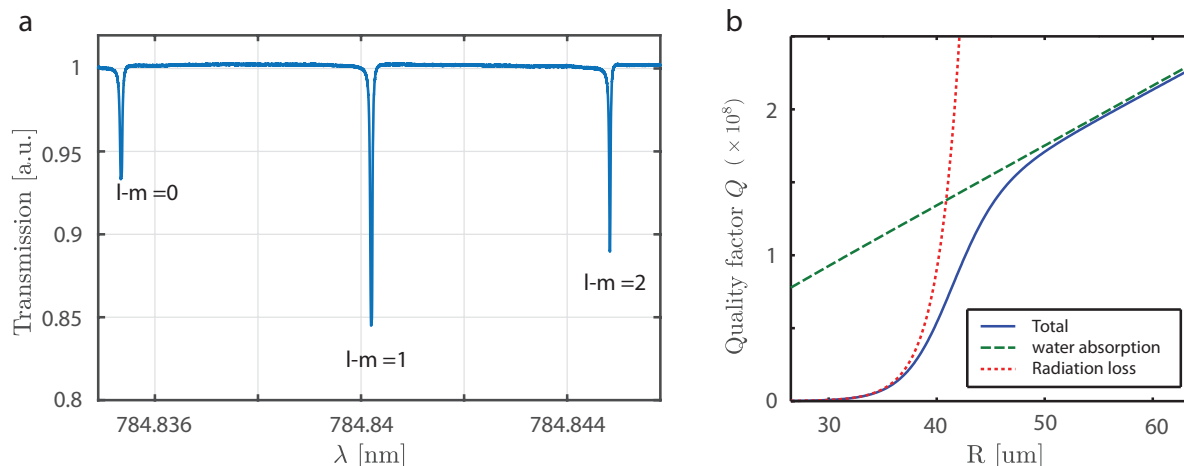


Figure 2.4. (a) WGM spectra obtained from a spheroidal resonator of radius $\approx 42 \mu\text{m}$ (b) Intrinsic quality factor contributions from absorption in the surrounding medium and radiation losses due to the curvature of the resonator. Image adapted from Foreman *et al.*⁷¹ Copyright 2014 Optical Society of America

and the radiation or bending losses due to the finite curvature of the resonator. Figure 2.4b plots contributions from these loss mechanisms providing the practical quality factors of $10^6 - 10^8$ depending on the radius and the surrounding medium for fused silica spheres.⁷²

Another parameter describing the spatial confinement of light in the resonator is the mode volume \mathcal{V} . Many definitions are found in the literature to quantify the mode volume of a resonator. For high Q resonators considered in this work, the mode volume can be defined as the energy density integrated over the whole space normalized to the maximum within the mode. Hence, the mode volume is given as,

$$\mathcal{V} = \frac{\int_v \epsilon(\mathbf{r}) |\mathbf{E}(\mathbf{r})|^2 dV}{\max[\epsilon(\mathbf{r}) |\mathbf{E}(\mathbf{r})|^2]}. \quad (2.9)$$

The mode volume of a fundamental TE WGM in a resonator with $R = 42.5 \mu\text{m}$ and $n_s = 1.4537$ excited at around 780 nm is $\mathcal{V} \approx 816 \mu\text{m}^3$. The mode volume was estimated using the MATLAB code by Balac and Féron.⁷⁰

For sensor systems based on optical resonances, the parameter Q/V is proportional to the sensitivity of the system and provides a qualitative way of categorizing resonant sensor systems. The typical Q values for resonators in this work are $10^6 - 2 \times 10^7$ and the mode volumes \mathcal{V} are in the range 800-1200 μm^3 .

2.1.2 Utilizing WGMs for sensing applications

Numerous examples of WGMs applied to sensing can be found in the literature. The principle of sensing in the most general terms is based on the change in the spectral properties of the WGM. In particular, the change in resonance frequency (wavelength), resonance linewidth (FWHM), and resonance mode splitting have been utilized for sensing applications.

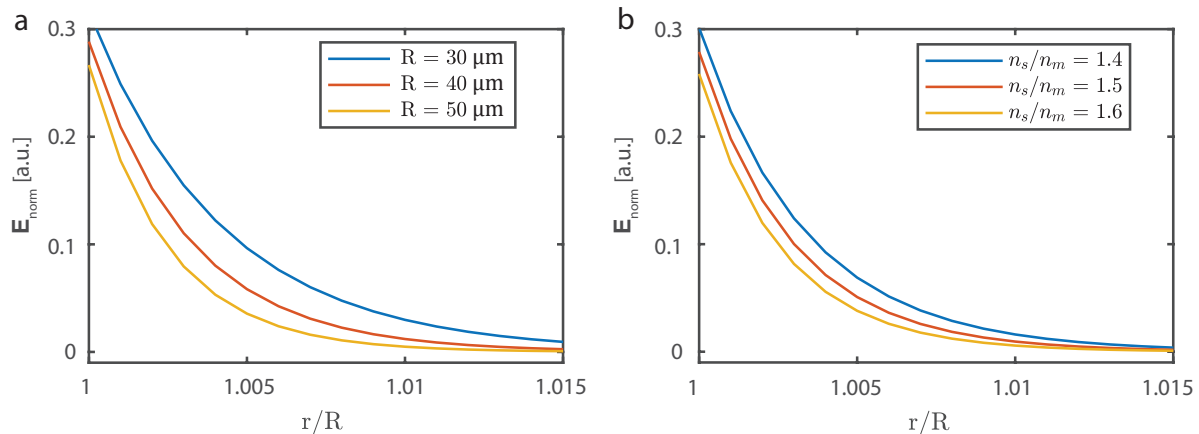


Figure 2.5. Evanescent field decay in the host medium. (a) Dependence of evanescent field decay length with radius of resonator R . (b) Dependence of evanescent field decay length on the relative refractive index n_s/n_m .

Frequency shifts based sensing

The most common method of sensing is using the resonance shift of the WGM frequency. Consider the spherical resonator illustrated in Figure 2.2 with radius R , refractive index of the material n_s immersed in a host medium of refractive index n_m . Shifts in the resonance wavelength (frequency) of the WGMs in this resonator can occur due to changes in the refractive in n_m , n_s or R . The fractional change in the resonance wavelength can be associated to changes in these parameters as,⁷³

$$\frac{\delta\lambda}{\lambda} = \frac{\delta R}{R} + F \frac{\delta n_m}{n_m} + (1 - F) \frac{\delta n_r}{n_r}, \quad (2.10)$$

where F is a sensitivity function related to the phase change due to reflection at the resonator surface. Equation (2.10), shows that WGMs can be used as refractive index sensors. Indirectly via changes in refractive index of the host medium or the resonator, various physical parameters such as temperature, pressure and pH can be measured.

The sensitivity of a TE WGM for bulk changes in the host refractive index is approximately given by,⁷⁴

$$\frac{\partial x}{\partial n_m} = -\frac{n_m^2}{(n_s^2 - n_m^2)^{3/2}} \left[1 - \frac{\alpha_a}{2^{1/3}} \frac{n_s^2}{n_s^2 - n_m^2} \nu^{-2/3} \right], \quad (2.11)$$

where, $\nu = l + 1/2$ and α_a are the roots of the Airy function $Ai(-z) = 0$. From (2.11), it follows that the sensitivity for bulk changes in host refractive index is higher for smaller resonators (smaller l) and lower contrast between host and resonator refractive indices. Figure 2.5 plots the radial decay of the evanescent field in the host medium as a function of the distance from the resonator surface for a TE polarized WGM excited by a 780 nm source. It can be seen that for smaller resonators and lower refractive index contrast, the evanescent field extends farther into the host medium. The field probes more of the host refractive index providing a greater contribution to the effective index of the WGM and thus increases the sensitivity of bulk changes in the host refractive index.

In the present work, we are interested in utilizing WGMs as sensors for detecting single biomolecules,

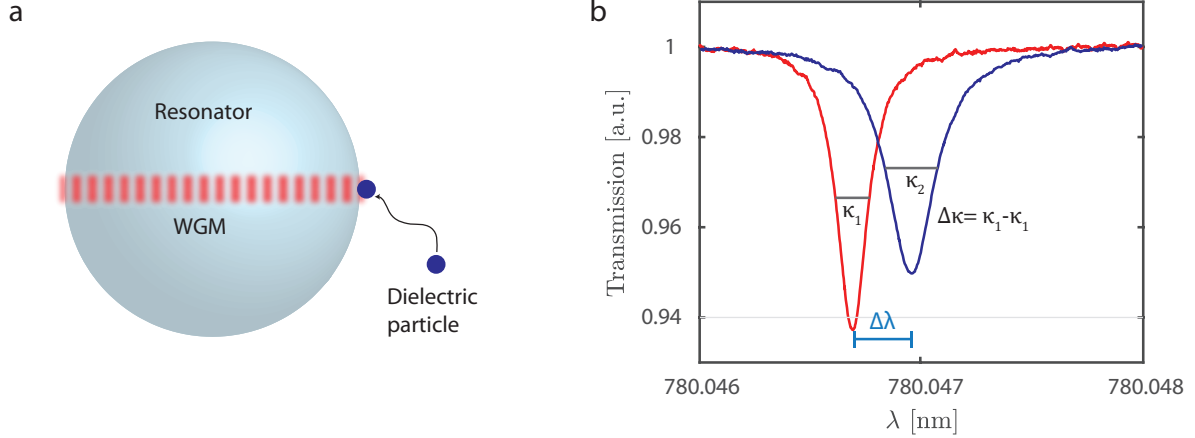


Figure 2.6. Interaction of a dielectric nanoparticle with the WGM. (a) Illustration of the interaction of a spherical dielectric particle with a WGM. (b) Resonance shift and linewidth broadening of the WGM upon interaction a dielectric particle.

rather than monitoring bulk changes in host refractive index. Equation (2.11) provides a good fit to sensing bulk changes in refractive index, but does not include all factors influencing the sensitivity for single biomolecules. The case of small particles such as micro/nanoparticles of dielectrics as well as biomolecules such as proteins can be considered using a perturbation theory approach.^{55,75} Consider the small dielectric particle diffusing into the evanescent field of the WGM depicted in Figure 2.6. Assuming the interaction of the particle with WGM is in the weak coupling regime (as opposed to strong coupling which can occur in the case of two coupled resonances), the fractional shift in WGM wavelength (frequency) can be given as,^{72,76}

$$\frac{\Delta\lambda}{\lambda} = -\frac{\Delta\omega}{\omega} \approx \frac{\int_{V_p} (\epsilon_p(\mathbf{r}) - \epsilon_m) \mathbf{E}(\mathbf{r})^* \cdot \dot{\mathbf{E}}(\mathbf{r}) d\mathbf{r}}{2 \int_V \epsilon(\mathbf{r}) \mathbf{E}(\mathbf{r})^* \cdot \dot{\mathbf{E}}(\mathbf{r}) d\mathbf{r}} \quad (2.12)$$

where $\mathbf{E}^*(\mathbf{r})$ is the Hermetian adjoint of $\mathbf{E}(\mathbf{r})$, $\epsilon_p(\mathbf{r})$ is the permittivity of the dielectric particle, V is volume of all space, V_p is the volume of the particle, $\mathbf{E}(\mathbf{r})$ is the electric field before the perturbation, $\dot{\mathbf{E}}(\mathbf{r})$ is the perturbed electric field, $\epsilon(\mathbf{r}) = \epsilon_s$ for $r < R$ and $\epsilon(\mathbf{r}) = \epsilon_m$ otherwise. Equation (2.12) can be rewritten in terms of the difference in polarizability of the particle and surrounding medium α_{ex} as,

$$\frac{\Delta\lambda}{\lambda} = -\frac{\Delta\omega}{\omega} \approx \frac{\Re[\alpha_{ex}]}{2} \frac{f |\mathbf{E}(\mathbf{r}_p)|^2}{\int_V \epsilon(\mathbf{r}) |\mathbf{E}(\mathbf{r})|^2 d\mathbf{r}} \quad (2.13)$$

where f is a correction term to account for the exponential decay of the evanescent field.⁷² For very small nanoparticles, $f \approx 1$. Figure 2.6b shows an example of an WGM initially at position λ shifted by an amount $\Delta\lambda$ when the nanoparticle enters the evanescent field of the WGM.

Loss based sensing

Similar to the resonance frequency, molecules can also cause additional losses in the WGM due to absorption and scattering. Single-particle induced linewidth changes ($\Delta\kappa$) associated with

absorption and scattering losses are given by

$$\frac{\Delta\kappa_{abs}}{\omega_0} \approx \Im[\alpha_{ex}] \frac{|\mathbf{E}(\mathbf{r}_p)|^2}{\int_V \epsilon(\mathbf{r}) |\mathbf{E}(\mathbf{r})|^2 d\mathbf{r}} \quad (2.14)$$

$$\Delta\kappa_{sca} \approx \frac{\omega^4 n_m^5 \epsilon_0}{6\pi c^3} \frac{|\alpha_{ex}|^2 |\mathbf{E}(\mathbf{r}_p)|^2}{\int_V \epsilon(\mathbf{r}) |\mathbf{E}(\mathbf{r})|^2 d\mathbf{r}} \quad (2.15)$$

respectively.³⁹ Figure 2.6b shows an illustration of the cavity spectrum of WGM before and after binding of a absorbing nanoparticle. The initial FWHM of the resonator κ_1 is increased to κ_2 .

Other sensing modalities

Another mechanism for sensing with WGMs is to use the lifting of degeneracy between counter-propagating WGMs due to the binding of a small scatterer. We previously mentioned that the WGMs with azimuthal indices $+m$ and $-m$ are degenerate. This degeneracy can be lifted when a scatterer binds to the WGM and scatters light into the direction opposite to the original propagation direction (see Figure 2.7a). The two counter-propagating WGMs interfere and standing wave modes (SWMs) are formed which are shifted from the original frequency by different amounts leading to split frequency modes Figure 2.7d. The strength of the mode split between the two SWMs is given as $2g$, where $g = \Delta\omega$ from (2.13) and the additional loss induced due to scattering is given as κ_{sca} from (2.15). The strength of the mode splitting and the resulting increase in linewidth has been previously used to detecting small dielectric nanoparticles.⁷⁷ However, sensing of single molecules has not been achieved using frequency splitting of WGMs. For multiple scatterers, the mode formation is more complex⁷⁸ and can be utilized for sensing single molecules as will be seen in Chapter 5.

Apart from these modalities, single molecules have been detected using coherent optomechanical oscillations of the resonator (OMO).^{53,79} This is achieved by exciting the WGM with a slightly blue-shifted frequency with sufficient power exciting the mechanical eigenmodes of the cavity. These modes have sub Hz linewidths and exhibit extremely high shift to linewidth ratio, high enough to detect adsorption of single bovine serum albumin (BSA) molecules to the surface of an unmodified fused silica microsphere.⁵³

Sensitivity and detection limits

WGMs have exceptional sensitivity for detecting small nanometer sized objects such as small gold nanoparticles^{80,81} and viruses.^{65,82} An important question to address is then about the ultimate detection limits of a WGM sensor. The fundamental limit of the detection in the classical regime is the shot noise limit that arises from the quantum nature of light. Although it is possible to circumvent this limit using the quantum properties of light,^{83,84} applications of such methods for sensing is challenging and has not yet been shown. For a sensor based on the

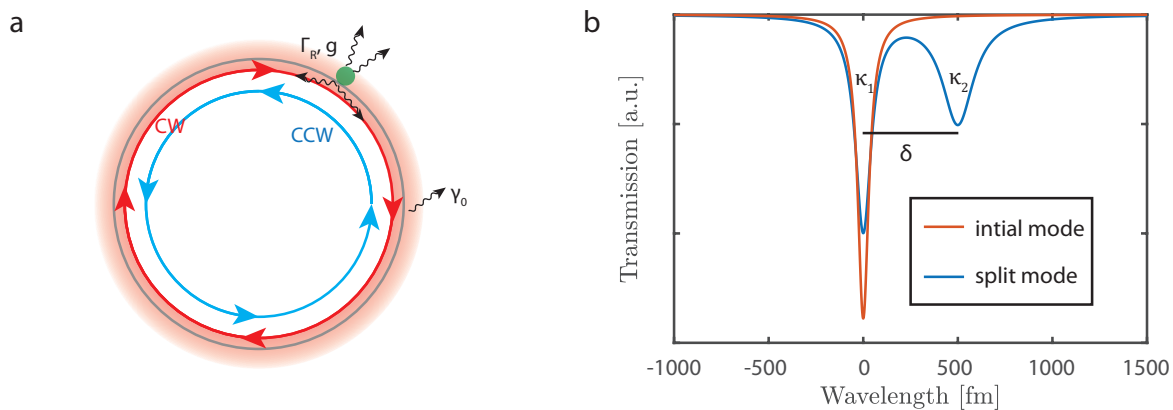


Figure 2.7. Mode splitting in WGMs. (a) Illustration of the interaction of a spherical scatterer with the WGM. The scatterer (green) couples light into the counter-propagating direction (CCW) resulting in standing wave modes. The scatterer also induces an extra loss κ_R due to light scattered away from the resonator and κ_0 is the initial intrinsic loss of the WGM. The coupling strength of the scatterer to WGM is quantified by g . (b) WGM spectrum before (orange) and after (blue) a scatterer binds to the WGM. The standing wave mode with its antinode symmetrical about the particle is red shifted and increases in FWHM whereas the mode with its node at the particle position is unaffected.

resonance shift of the WGM, the shot noise detection limit is given as,⁸⁵

$$\frac{\delta\omega_{min}}{\omega} \geq \frac{1}{Q} \sqrt{\frac{\hbar\omega}{P_0\beta\eta\tau}} \quad (2.16)$$

where, $\delta\omega_{min}$ is the minimum resolvable shift, Q is the quality factor of the cavity, \hbar is the Planck's constant, ω is the laser frequency, P_0 is the input power, β is the coupling efficiency, η is the photodetector quantum efficiency and τ is the integration time. For a typical WGM with $Q = 1 \times 10^7$, $\omega/2\pi = 3.84 \times 10^4$ Hz, $P_0 = 100 \mu\text{W}$, $\eta = 0.9$, $\beta = 0.1$ and $\tau = 20$ ms, the shot noise limited minimum detectable shift is $\delta\omega_{min} = 5.75$ Hz. The expected resonance shift from a single protein of diameter = 10 nm and refractive index $n_p = 1.54$ is much higher and is approximately 1.8 kHz (from (2.13) assuming a fundamental mode with $R = 42.5 \mu\text{m}$ in a fused silica resonator and $\lambda = 780$ nm). Hence, for a shot noise limited system using high Q WGMs, sensing of single proteins should be easily achievable. However, in reality, each measurement system is affected by other noise sources depending on the timescales of interaction. Biological sensors typically have to work in the μs -s timescale, where noise sources other than the shot noise limit the detection. Figure 2.8 plots the Allan variance measured for two microtorroid resonators at various integration times.⁸⁶ The theoretically estimated detection limit based on thermorefractive noise⁸⁷ and shot noise from (2.16) for a resonator of radius $R = 40 \mu\text{m}$ excited at $\lambda \approx 780$ nm are also plotted for reference. The figure is reprinted from Foreman *et al.*⁷² The figure shows that, at the μs -ms timescale, the so called thermorefractive noise^{72,87} limits sensitivity. Another factor that affects the noise at these timescales is the laser frequency jitter. This puts the minimum detectable shift to much higher values in the range of 10 – 100 kHz. At longer time scales in the range of 1 s or longer, other noise sources such as thermal and laser drifts increase the noise further putting the minimum detectable shift to > 1 MHz. It

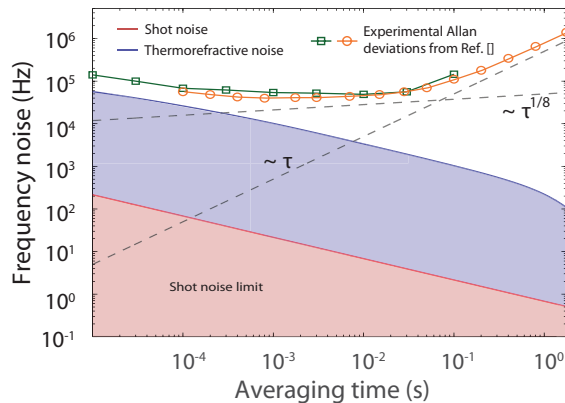


Figure 2.8. Allan variance of the a WGM resonance frequency for two microtorroid resonators measured by Dobrindt.⁸⁶ The theoretical detection limits estimated based on the thermorefractive noise⁸⁷ and shot noise are plotted for reference. Image reprinted from Foreman *et al.*⁷²

has to be noted here that these long-term drifts can be corrected by good thermal isolation, temperature control and utilizing multiple WGMs as reference. In Chapter 6 we will see how the Allan variance of a microsphere resonator scales with integration time τ when measured using a commercial diode laser and discuss the sources of noise in the system.

The detection limits for sensing single viruses for a realistic sensor was considered by Arnold *et al.*⁸⁸ A more rigorous estimate of of the detection limit for small biomolecules based on the Cramer-Rao Lower Bound was estimated by Foreman *et al.*⁷¹ The minimum number of small biomolecules (considered spherical) with polarizability α required to produce a detectable frequency shift for a WGM sensor where spectra are acquired by laser scanning as,⁷¹

$$N = \frac{(n_s^2 - n_m^2)}{\Re[\alpha]} \frac{R^3}{|Y_l(\pi/2)|^2} \frac{F}{Q_0} \frac{(1 + Q_c/Q_0)^3}{4Q_c^2/Q_o^2} \quad (2.17)$$

where, n_s is the refractive index of the cavity material, n_m is the refractive index of surrounding medium, Q_0 is the intrinsic quality factor of the WGM, Q_c is the coupling quality factor, Y_l the usual spherical harmonic function and F is an sensitivity factor that depends on experimental configuration . The minimum number of molecules that causes a detectable shift to a WGM excited a spherical resonator with $R = 40 \mu\text{m}$ and $\lambda \approx 780 \text{ nm}$ is approximately 10^5 . Hence, achieving single molecule detection using WGMs under physiological conditions requires enhancement of the WGM signal as will be discussed in Section 2.3.

2.2 Plasmonic nanoparticles

In the previous section, we looked at the physics of resonances in spheroidal dielectric cavities and their application to sensing. In this section, we will describe a complementary type of resonance that has been extensively used for biosensing in the past few decades, namely, Localised Surface Plasmon Resonance (LSPR). LSPRs are the resonances occurring in nanostructures (size $\ll \lambda$) of metals such as silver, gold, and copper due to the collective oscillations of the surface electrons in these metals. These oscillations can be excited directly by incident electromagnetic radiation and lead to the often bright colors seen in aqueous solutions of these particles. The bright colors of metal nanoparticle suspensions have been used for millennia for various works of art. Famous examples are the Lycurgus cup from the Late Roman period and the amazing stained glass windows of the Gothic Churches in various parts of Europe. Figure 2.9 shows part of the north rose window in the Cathédrale Notre-Dame de Chartres, Paris, France. The brilliant colors in the stained glass arise due to scattering from various sized silver and gold nanoparticles. Although the ability of these nanoparticles to scatter different colors was used in art, the actual physics of these were only understood more recently in the 20th century. Apart from enhancing the scattering cross-section, these LSPRs also lead to an amplification of the field both inside the particle and in the immediate vicinity (near-field). This enhancement in the near-field amplitude has been extensively explored for sensing⁸⁹ and therapeutic applications in the past two decades.^{90,91}

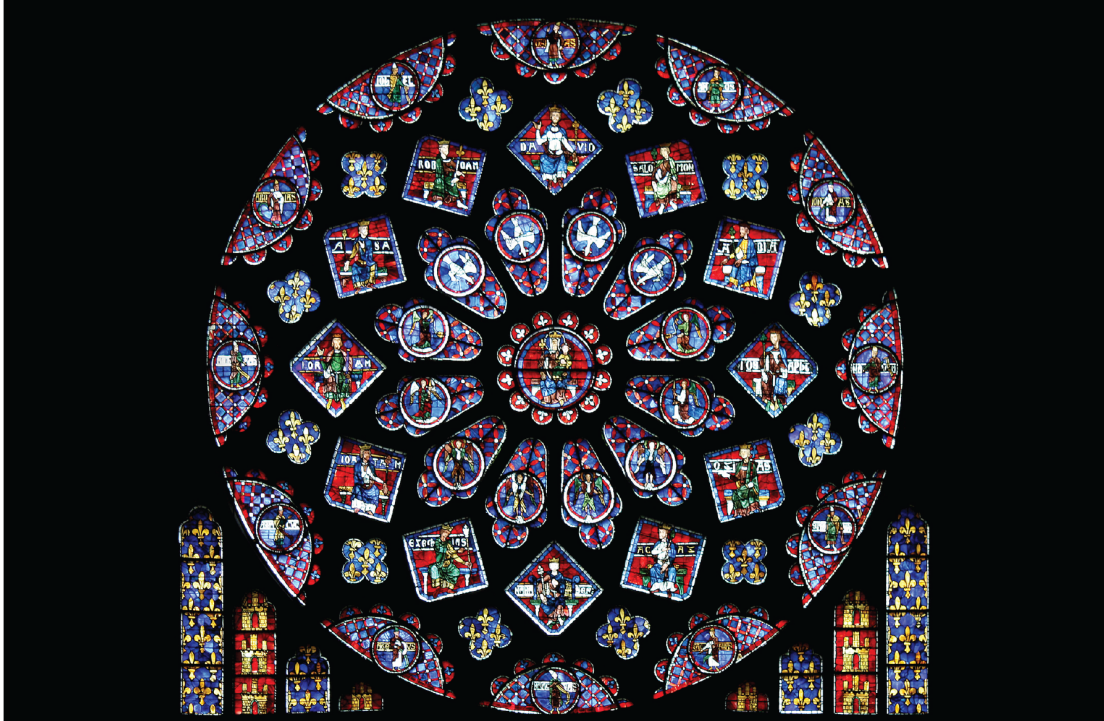



Figure 2.9. Part of the stained glass window Rosace Nord in the Cathédrale Notre-Dame de Chartres, Paris, France. Photograph by Eusebius (Guillaume Piolle) .

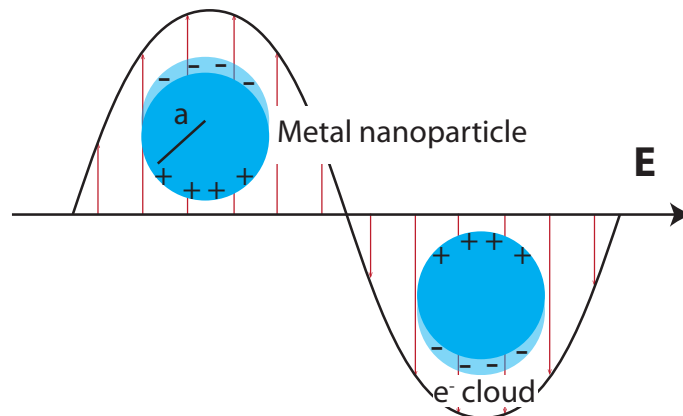


Figure 2.10. Schematic illustration of the excitation of the LSPRs in sub-wavelength metallic nanoparticles. The displacement of the conduction electrons with the varying electric-field and an effective restoring force by the curved surface induces resonance in the particles.

2.2.1 Spherical nanoparticle in an electric field

In this section, we will briefly describe the physical origin of these LSPRs in spherical sub-wavelength particles. Again the aim of this section is not to provide a rigorous theoretical description, but rather to provide an intuition for some key parameters such as the enhancement of the scattering, extinction cross-sections, and the near-field. Figure 2.10 shows an illustration of a metal nanoparticle in an oscillating electric field. The conduction band electrons are displaced with the oscillating electric field as they are only loosely bound to the metal. If the frequency of these oscillations matches the plasmonic resonance frequency, the amplitude of these oscillations can be enhanced.

The problem of describing LSPRs in spherical metal nanoparticles is related to the problem of scattering by metallic nanoparticles. For simplicity, let's assume that the spherical particle's radius $a \ll \lambda$, where λ is the wavelength of the oscillations of the EM field, and that the material of the particle and the surrounding media are isotropic with relative permittivity $\epsilon_p = \epsilon_p(\omega)$ and ϵ_m , respectively. Here, the permittivity of the material is dependent on the frequency of the electric field oscillations ω . Since $a \ll \lambda$, the phase of the oscillating field is practically constant over the particle. Hence, we can consider the particle to be in an static electric field $\mathbf{E}_0 = E_0 \hat{\mathbf{z}}$ (quasi-static approximation) and add the harmonic oscillations later. For electrostatic problems,⁹² we can solve the Laplace equation for the potential $\Delta V = 0$, where Δ is the Laplacian operator. The electric field can then be calculated as $\mathbf{E} = -\nabla V$. The solution of the Laplace equation in spherical coordinates is given as,⁹³

$$V(r, \theta) = \sum_{l=0}^{\infty} [A_l r^l + B_l r^{-(l+1)}] P_l(\cos \theta) \quad (2.18)$$

where $P_l(\cos \theta)$ are the Legendre Polynomials of order l , θ the polar angle, r the radial distance, A_l and B_l are constants to be determined.

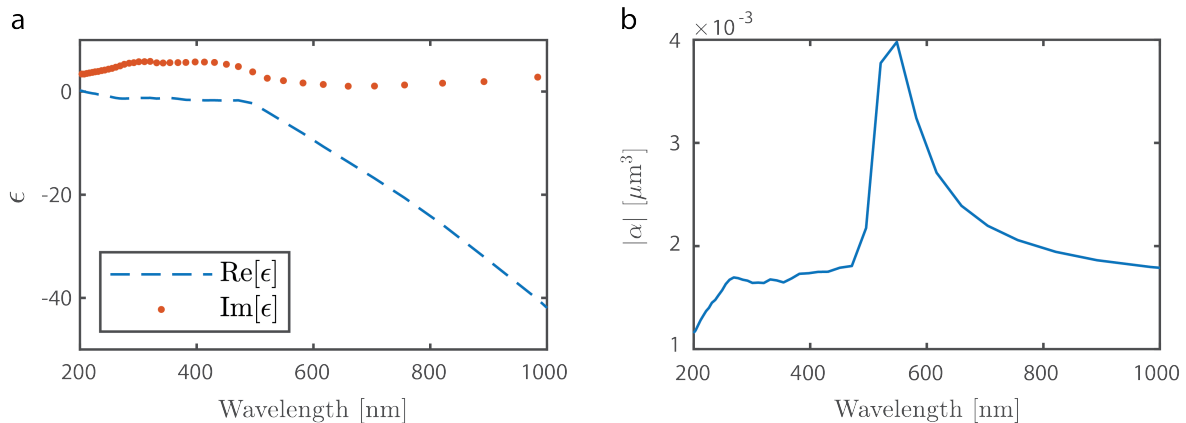


Figure 2.11. (a) Real and imaginary part of the relative permittivity of gold.⁹⁴ (b) Polarizability of a gold nanosphere of radius 50 nm at different wavelengths plotted using (2.22).

The following boundary conditions apply,

$$V_{in} = V_{out} \quad \text{for } r = a \quad (2.19a)$$

$$\epsilon_p \frac{\partial V_{in}}{\partial r} = \epsilon_m \frac{\partial V_{out}}{\partial r} \quad \text{for } r = a \quad (2.19b)$$

$$\lim_{r \rightarrow \infty} V_{out} = -E_0 r \cos \theta = -E_0 z \quad (2.19c)$$

where V_{in} and V_{out} are the potentials inside and outside the spherical particle. Applying the boundary conditions in (2.19), the potentials inside and outside the sphere can be given as,⁹²

$$V_{in} = -\frac{3\epsilon_m}{\epsilon_p + 2\epsilon_m} E_0 r \cos \theta \quad (2.20a)$$

$$V_{out} = -E_0 r \cos \theta + \frac{\epsilon_p - \epsilon_m}{\epsilon_p + 2\epsilon_m} E_0 a^3 \frac{\cos \theta}{r^2} \quad (2.20b)$$

Equation (2.20b) can be rewritten as,

$$V_{out} = \left(-1 + \frac{\alpha}{4\pi r^3} \right) E_0 r \cos \theta \quad (2.21)$$

where α is the polarizability of the nanoparticle and is given as,

$$\alpha = 4\pi a^3 \frac{\epsilon_p - \epsilon_m}{\epsilon_p + 2\epsilon_m}. \quad (2.22)$$

It can be seen from (2.22) that resonance occurs when the denominator is minimized, that is when $\Re[\epsilon_p] = 2\epsilon_m$ and is known as the Frölich resonance condition. Figure 2.11a plots the relative permittivity of gold at different wavelengths.⁹⁴ Figure 2.11b plot the magnitude of the polarizability for a Au sphere of radius 50 nm showing a resonance enhancement of the polarizability around $\lambda = 550$ nm.

The electric fields inside and outside the spherical nanoparticle can be calculated from (2.20b)

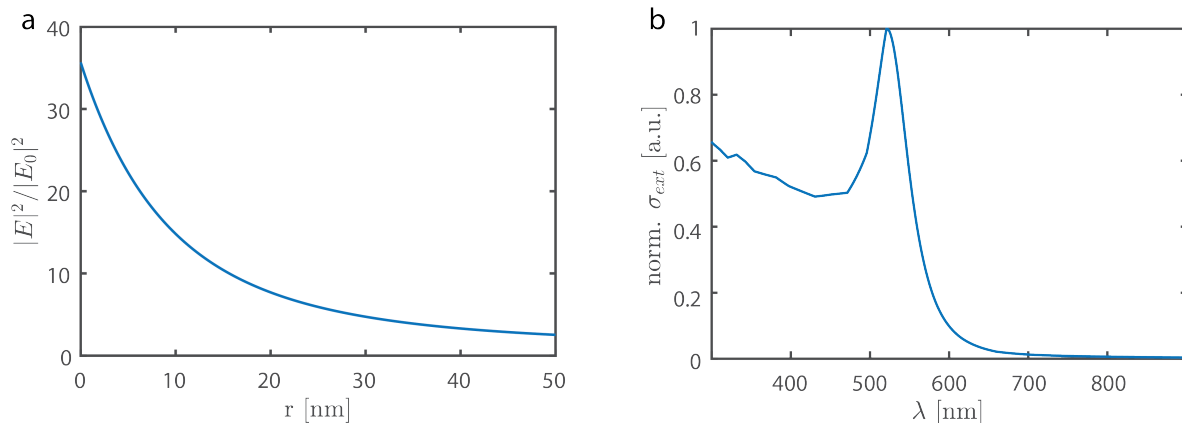


Figure 2.12. (a) Radial dependence of the intensity enhancement outside the metal nanosphere. (b) Calculated normalized extinction spectrum of a spherical gold nanoparticle of diameter 10 nm.

and (2.21) as,

$$\mathbf{E}_{\text{in}}(\mathbf{r}, \theta) = \frac{3\epsilon_m}{\epsilon_p + 2\epsilon_m} E_0 (\cos \theta \hat{e}_r - \sin \theta \hat{e}_\theta) \quad (2.23a)$$

$$\mathbf{E}_{\text{out}}(\mathbf{r}, \theta) = E_0 \left[\left(1 + \frac{2\alpha}{4\pi r^3}\right) \cos \theta \hat{e}_r + \left(-1 + \frac{\alpha}{4\pi r^3}\right) \sin \theta \hat{e}_\theta \right] \quad (2.23b)$$

where \hat{e}_r and \hat{e}_θ are the unit vectors in r and θ directions respectively. Equation (2.23b) shows that the electric field outside the nanoparticle is maximized at $\theta = 0, \pi$. From (2.23b), the ratio of the excitation field intensity $|\mathbf{E}_0|^2$ and the intensity outside the particle $|\mathbf{E}_{\text{out}}|^2$ at $\theta = 0, \pi$ is,

$$\frac{|E_{\text{out}}|^2}{|E_0|^2} = \left|1 + \frac{\alpha}{2\pi r^3}\right|^2. \quad (2.24)$$

Equation (2.24), provides a simple relationship for the enhancement of the electric field by metal nanospheres. The intensity enhancement is proportional to the polarizability of the particle and quickly decays with distance from the surface as r^{-3} (see figure 2.12a). Sensing using metal nanoparticles relies on this enhancement of the near-field to provide an increased sensitivity to the analytes.

So far we have only described the real part of the nanoparticle polarizability. The imaginary part of the polarizability of the nanoparticle takes into account the losses in the metal and leads to the broad linewidth (FWHM) of the LSPR. Then, similar to the WGM resonators described in the previous section, LSPRs in metal nanoparticles can also be characterized by a quality factor Q_{np} and an effective mode volume \mathcal{V}_{np} , where the subscript np stands for nanoparticle. Typically, the quality factor of LSPRs is in the range of $q \approx 10 - 100$ owing to the large absorption and radiative losses in these particles. The effective mode volume of metal nanoparticles can be defined by (2.9). Khurgin and Sun estimated the effective mode volume for the first dipolar resonance to be,⁹⁵

$$\mathcal{V}_{np} = \frac{4\pi a^3}{3} \left(1 + \frac{1}{2\epsilon_m}\right). \quad (2.25)$$

From (2.25), we can estimate an effective mode volume in the range of $0.003 \mu\text{m}^3$.

In experiments, the scattering or extinction of light by these metal nanoparticles are usually monitored. Hence, it is useful to calculate the scattering and absorption cross-sections of the metal nanosphere. The scattering σ_{sca} and absorption σ_{abs} cross-sections are given as,⁹²

$$\sigma_{sca} = \frac{k^4}{6\pi} |\alpha|^2 \quad (2.26a)$$

$$\sigma_{abs} = k\Im[\alpha] \quad (2.26b)$$

$$\sigma_{ext} = \sigma_{sca} + \sigma_{abs} \quad (2.26c)$$

The normalized extinction spectrum of a metal nanosphere of diameter 10 nm is plotted in Figure 2.12b.

2.2.2 Tuning LSPRs

It is clear from the above description that the polarizability α is the key parameter associated with the enhancement of the near-field and extinction cross-sections. Hence, these parameters can be optimized by tuning the polarizability of these nanoparticles. In experiments, we would like to be able to excite the nanoparticles using various wavelengths of light. We can achieve the tuning of the resonance wavelength of LSPRs by changing the morphology of nanoparticles. For example, a rod-shaped particle has a longitudinal (along the longer axes) LSPR that is at a higher wavelength than that of a spherical particle.

Here, we will consider an ellipsoidal particle shape with the semiaxes $a_1 \leq a_2 \leq a_3$ to obtain a simple analytic expression for the resonance wavelength of these longitudinal LSPRs. The polarizabilities α_i of an ellipsoidal particle along the different axes is given by the expression,⁹²

$$\alpha_i = \frac{4}{3} \pi a_1 a_2 a_3 \frac{\epsilon_p - \epsilon_m}{\epsilon_m + L_i (\epsilon_p - \epsilon_m)}, \quad (2.27)$$

where $i = 1, 2$ or 3 and L_i is a shape parameter given as,

$$L_i = \frac{a_1 a_2 a_3}{2} \int_0^\infty \frac{ds}{(a_i^2 + s) \sqrt{(s + a_1^2)(s + a_2^2)(s + a_3^2)}}, \quad (2.28)$$

and $\sum L_i = 1$. The new resonance condition is now,

$$\Re[\epsilon_p] = \left(1 - \frac{1}{L_i}\right) \epsilon_m. \quad (2.29)$$

For a sphere, $L_1 = L_2 = L_3 = 1/3$ and (2.29) boils down to the Frölich condition. For the case of a spheroid with $a_1 = a_2$ and $a_3 = e \times a_1$, where e is the aspect ratio of the spheroid, the longitudinal LSPR, that is for excitation along the longer dimension (along a_3 when $e > 1$ and along a_1, a_2 when $e < 1$), is shifted to longer wavelengths (see Figure 2.13a). Although it possible to derive analytical equation for simple geometries, numerical methods have to be employed for more complex geometries. Many numerical methods such as Discrete Dipole Approxima-

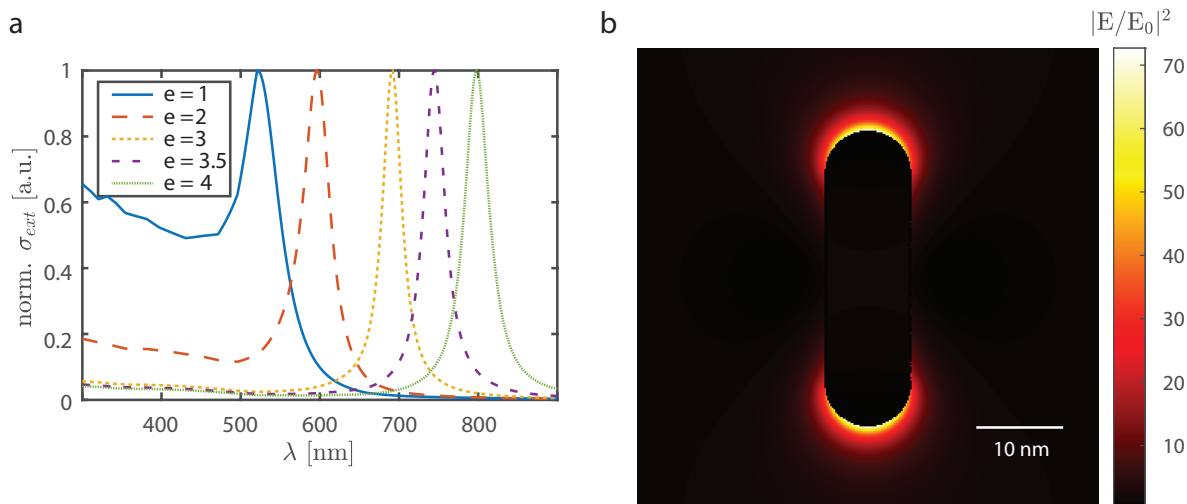


Figure 2.13. (a) Near-field intensity enhancement by a rod-shaped plasmonic gold particle simulated using MNPBEM.⁹⁶ (b) Calculated normalized extinction spectra of ellipsoidal nanoparticles with various aspect ratios e . The plasmon resonance frequency is shifted to longer wavelengths as the aspect ratio increases.

tion, Finite-Element Method, Finite-difference time-domain (FDTD), and Boundary Element Method (BEM) have been utilized to simulate LSPRs in arbitrary shaped metal nanoparticles. Figure 2.13b plots the near-field intensity enhancement of a Au plasmonic nanorod (cylinder with two hemispherical end caps) of diameter 10 nm and height 35 nm simulated using a BEM approach (MNPBEM⁹⁶). Such nanorods are utilized in this work to provide the necessary signal enhancements for studying single biomolecules.

2.2.3 LSPR based sensing

The frequency of LSPRs is dictated by the polarizability α which is dependent on the permittivity of the host medium. Hence, a change in the local permittivity or a small inclusion of

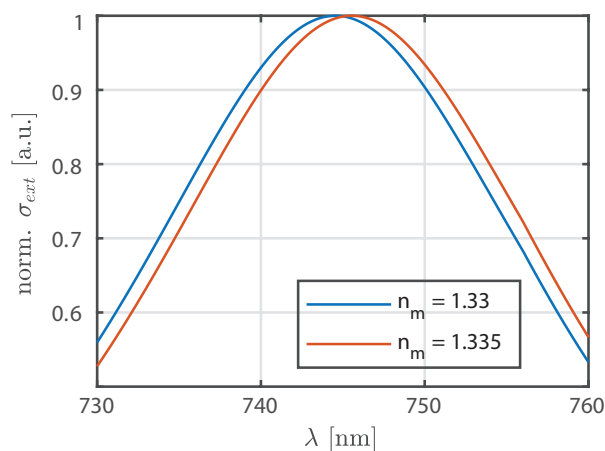


Figure 2.14. Shift of the plasmonic resonance of a rod shaped particle of aspect ratio 3.5 and diameter 10 nm upon a $\Delta n = 0.005$ change in host refractive index.

biomolecules to the near-field results in a shift of the LSPR. Figure 2.14 plots the redshift of the longitudinal LSPR for the plasmonic nanorod plotted in figure 2.13b upon a change in host medium refractive index of $\Delta n = 0.005$.

2.3 WGM-plasmon hybrid sensing

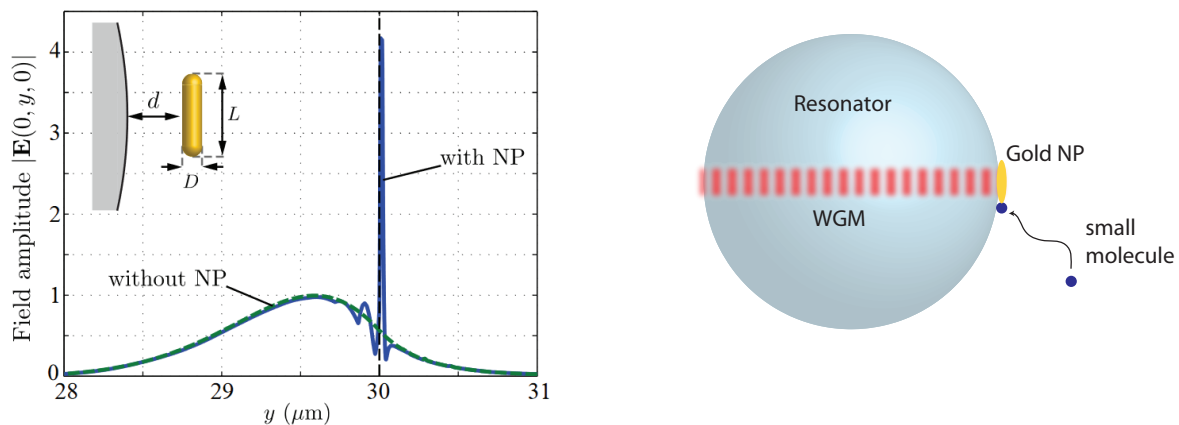


Figure 2.15. (a) Normalized field amplitude within and outside a spherical WGM microcavity of radius $30 \mu\text{m}$ with and without the presence of a plasmonic gold nanorod on its surface. Figure adapted from Supplementary Info of Baaske *et al.*⁸¹ (b) Illustration of the interaction of a small molecule with the nanorod immobilized on a WGM surface.

The previous sections described the theory and working principle of two types of resonance based sensors, namely optical WGMs and plasmonic nanoparticles. Both systems have exceptional sensitivity for changes in the local refractive index. Although fundamentally, both systems are capable of detecting down to single molecules, SM sensing with either system is limited in practice due to various sources of noise (see Section 2.1.2). This section describes the working principle of a WGM-plasmonic hybrid sensor that utilizes the advantages of both systems to enable real-time detection of extremely small (down to single ions) individual entities in solution.

For the interaction of small nanometer sized objects with the evanescent field of a fundamental WGM, (2.13) can be rewritten as,

$$\frac{\Delta\omega}{\omega_0} = \frac{-\Delta\lambda}{\lambda_0} \approx -\frac{\Re[\alpha]}{2} \frac{\epsilon_m f^2(\mathbf{r}_p)}{\mathcal{V}} \quad (2.30)$$

where, $f^2(\mathbf{r}_p) = |\mathbf{E}(\mathbf{r}_p)|^2 / \max[\epsilon(\mathbf{r})|\mathbf{E}(\mathbf{r})|^2]$ is the normalized mode distribution, $\mathcal{V} = \int_V \epsilon(\mathbf{r})|\mathbf{E}(\mathbf{r})|^2 d\mathbf{r} / \max[\epsilon(\mathbf{r})|\mathbf{E}(\mathbf{r})|^2]$ is the mode volume and $\epsilon(\mathbf{r})$ is the permittivity of glass inside the resonator and of the surrounding medium outside. The fractional shift in the wavelength (or frequency) is then proportional to the factor $f^2(\mathbf{r}_p)/\mathcal{V}$. For a bare WGM cavity, the value of $f(\mathbf{r}_p) \ll 1$ as the magnitude of the electric field at the particle location (WGM cavity surface) is much smaller than the maximum of the field within the cavity (see Figure 2.3).

Figure 2.15a shows the normalized field amplitude of a WGM cavity with and without plasmonic

enhancement (figure adapted from the Supplementary Information of Baaske et al.⁸¹). The boundary of the WGM cavity is at $y = 30 \mu\text{m}$. When a plasmonic nanoparticle is added to the WGM cavity surface as shown in Figure 2.15b, the maximum of the electric field is shifted to the near-field of the plasmonic nanoparticle due to the plasmonic enhancement. The local field enhancement of the nanoparticle can now be considered in (2.30) without including any effects of the hybridization of the WGM and plasmonic resonances as the coupling between the two resonances is weak. The weak coupling assumption is valid in this case as the two resonators have orders of magnitude difference in their decay rates. When a small molecule now binds to the tips of the nanoparticle, the shifts induced in the WGM resonance are higher than when the molecule binds directly to the WGM surface. The value of $f^2(\mathbf{r}_p)$ is now equal to 1 as the maximum field intensity is at the particle location. Further, the mode volume of the combined system \mathcal{V} is much smaller than the bare WGM as the maximum field intensity is enhanced by the nanoparticle. Equation (2.30) provides an intuitive expression to understand the working principle of a WGM-plasmonic hybrid sensor. Thus, the sensor presented in this thesis enables sensitive single-molecule detection by leveraging the high-quality factor for the WGM resonance with the small mode volume of the localized surface plasmon resonance.

Chapter 3

Experimental design

In the previous chapter, we described the necessary theory required to utilize optical WGMs and plasmonic nanoparticles as sensors for studying single molecules. In this chapter, we will look at the practical implementation of the experimental system and the standard protocols required to fabricate, assemble, and utilize the WGM-plasmonic sensor. First, the schematic of the experimental setup is provided and the components are listed. Second, the setup and method for fabricating fused silica microsphere cavities are presented. Third, a brief description of efficient light coupling into WGMs using frustrated total internal reflection (FTIR) is provided. Fourth, the wiring diagrams for the acquisition of the complete WGM spectra using a laser scanning method is provided. Fifth, the connection diagram for establishing a fast lock-in to track the WGM resonance position is provided. Next, the extraction of the WGM position and full-width-at-half-maximum (FWHM) time traces and the analysis of the signal peaks are described. Finally, a brief description of the standard protocols for assembling the sensor and performing single-molecule measurements are provided.

3.1 Experimental setup

Figure 3.1 shows the schematic of the setup used to detect single molecules. An external cavity diode laser (Toptica TA pro 780HP, Toptica GmbH, Munich, Germany) is used as the excitation laser. The laser is modulated at 238 – 380 MHz using an electro-optic phase modulator (EOM) (NIR-MPX800-LN-05, Ixblue Photonics, France). Frustrated total internal reflection (FTIR) at the surface of a high refractive index prism made of N-SF11 glass ($n_{780\text{ nm}} \approx 1.77$) is used for efficient coupling of light into the WGM. The coupling optics consists of a collimator (F260APC-780 Thorlabs Inc.), a half-wave plate (WPH05M-780, Thorlabs Inc.), a beam expander (BE02-05-B, Thorlabs Inc.), and a focusing lens (AC254-075-B-M L, Thorlabs Inc.) placed on an XYZ manual translation stage. A photodetector (PDA10AZ-EC, Thorlabs Inc.) is used for collecting the light reflected off the prism surface. The WGM microcavity is an 80-90 μm diameter glass microsphere fabricated at the end of a single-mode optical fiber (SMF 28e, Corning GmbH, Germany). An imaging system with an Olympus 10x objective with a $f = 200\text{ mm}$ objective

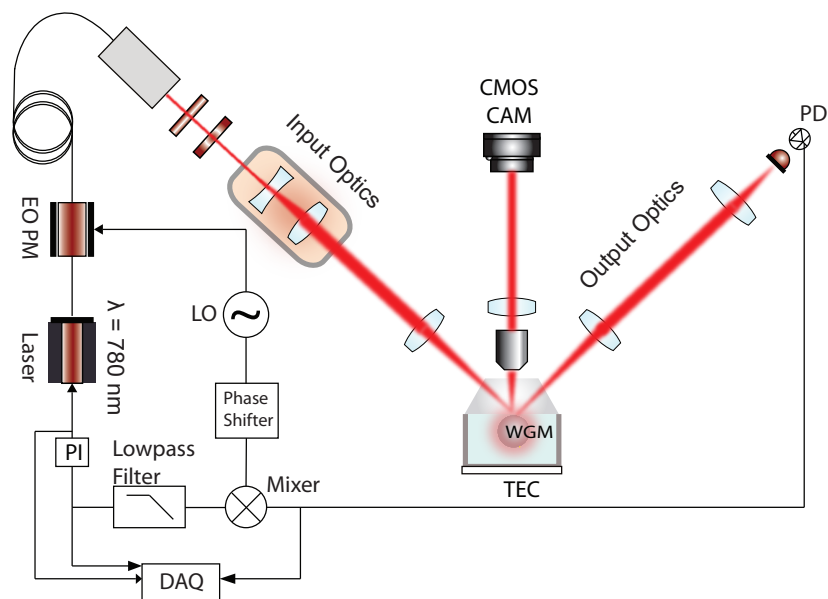


Figure 3.1. Schematic of the experimental setup for studying single molecules using a WGM-plasmonic sensor. Light from a tunable CW external cavity diode laser reflected off a high refractive index prism. The spherical glass resonator is brought close to the surface of the prism using micrometer stages and light is coupled into the cavity due to frustrated total internal reflection. The glass microsphere sits in a PDMS cuvette where samples are injected.

lens (AC254-200-B, Thorlabs GmbH, Germany) and a CMOS camera (DCC1545M, Thorlabs GmbH, Germany) is used to image the laser spot and the microcavity. A v-shaped chamber cut from polydimethylsiloxane (PDMS) is used for sample loading. The sample chamber volume is 300-400 μl in all experiments so as to allow easy injection of samples and rinsing of the chamber manually. A thermoelectric element (32 W TEC, Thorlabs GmbH, Germany) is used to seal the other end of the v-shaped chamber as shown in the figure. A PID temperature controller (5310 TECSorce, Arroyo Instruments LLC, USA) and a pt-100 (362-9799, RS PRO, RS Components Ltd., UK) temperature sensor are used to control the chamber temperature between 15 – 50 $^{\circ}\text{C}$ with a temperature control stability of $\pm 0.2\text{ K}$.

3.2 Fabrication of glass microspheres

High Q microresonators are fabricated using a CO_2 laser system shown in Figure 3.2. A 30 W CO_2 laser, $\lambda \approx 10.6\ \mu\text{m}$ (Synrad 48-2, Novanta Inc., WA, USA), is used at 10 – 15% peak power and is focussed using a focal length $f = 50\ \text{mm}$, ZnSe lens onto a single-mode optical fiber (SMF 28e, Corning GmbH, Germany). The optical fiber is stripped off its protective coating user a fiber stripper and cleaned with lint-free wipes (Kimwipes, Delicate Science wipes, Kimberly-Clark Professional) soaked first in acetone and then Isopropanol. The fiber is then inserted into a fiber optic ferrule (O.D. = 2.5 mm, I.D = 126 μm , Thorlabs GmbH, Germany). The fiber is cleaned again with acetone and Isopropanol after insertion. A small weight (typically another ferrule) is attached to the free end of the fiber. The fiber with the ferrules is then mounted on a manual stage and positioned at the focus of the CO_2 laser system. The fiber is

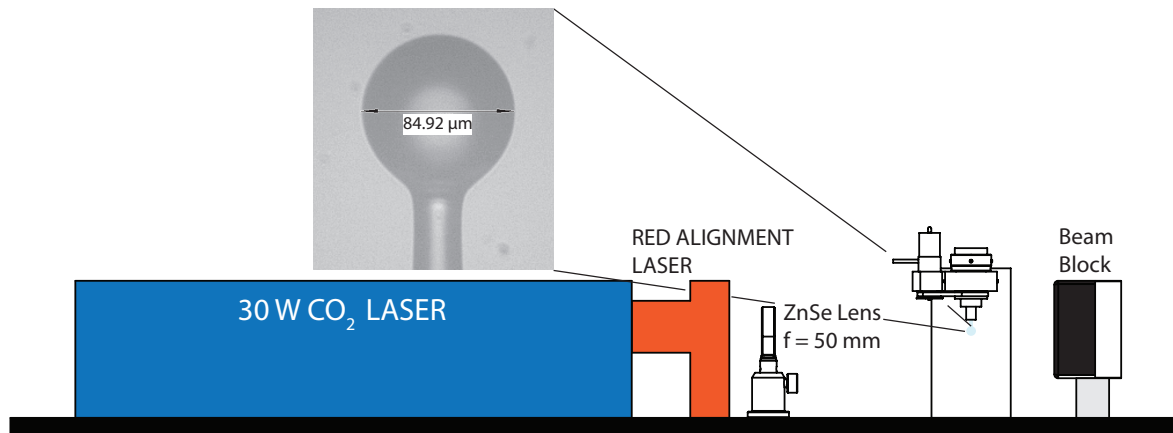


Figure 3.2. Schematic of the resonator fabrication setup. A focussed CO₂ laser is used to melt a single-mode optical fiber into a spherical resonator. Inset shows a photograph of a resonator fabricated in the setup.

first tapered using a power of $P \approx 3$ W and then a glass sphere is melted at a slightly higher laser power of about $P \approx 3 - 4$ W until a spherical shape is obtained. The inset of Figure 3.2 shows a photograph of a glass microsphere fabricated with a diameter of ≈ 85 μm. Typically, microspheres with diameters in the range of 80-90 μm are used in this work.

3.3 Efficient coupling to optical WGMs

Efficient and controllable coupling of light to and from the resonator is crucial for practical applications. There exist a myriad of methods to couple light into a WGM resonator such as free-space coupling, fluorescent coupling, scatterer-based coupling, and evanescent coupling using tapered/polished fibers or prisms. Amongst these methods, evanescent coupling is by far the most robust, efficient, and controllable method. The most efficient method of evanescent coupling is to use tapered fibers. Under critical coupling conditions when the resonator losses equal the waveguide coupling loss, efficiencies up to 99.99%⁹⁷ can be achieved. Nonetheless, the major disadvantage of tapered fibers is their mechanical stability, which is critical for practical sensing applications. Also, particles binding to the taper changes the coupling radically and the transmission through the fiber reduces drastically upon binding of plasmonic nanoparticles.

Since, the robustness of the coupling is an important criteria for practical sensing applications, we use a prism based coupling setup (see Figure 3.1). Although initial alignment is time consuming, coupling efficiencies of up to 80% can be achieved⁹⁸ with robustness against mechanical, thermal and pressure noise sources. Coupling using a prism is based on frustrated total internal reflection (FTIR). Light tunnels from a prism to a WGM resonator when the evanescent field of the latter is overlapped with the evanescent field due to total internal reflection at a prism surface and the phase matching condition is met. Using a coupled mode approach, Gorodetsky

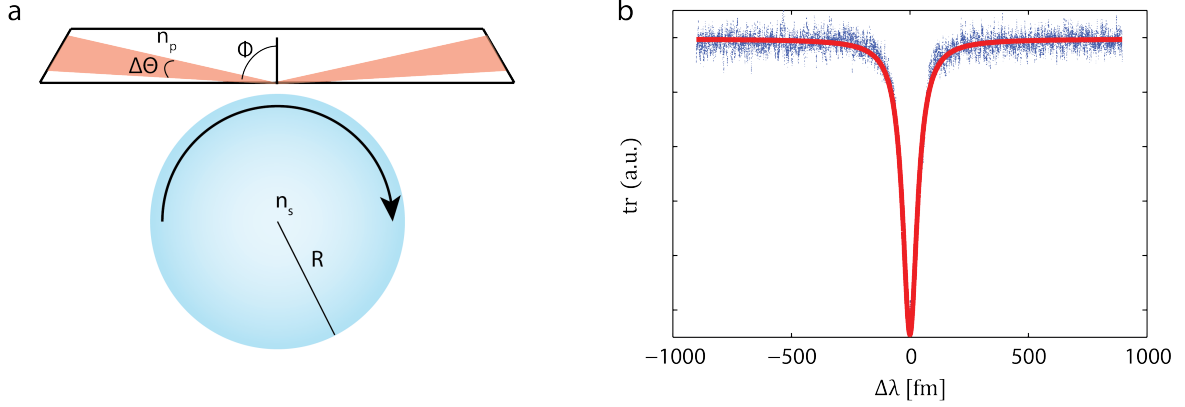


Figure 3.3. (a) Schematic of a microsphere resonator evanescently coupled via a prism. (b) Normalized transmission spectrum (blue) and the corresponding fit (red) obtained from a silica microsphere of $d \approx 98 \mu$ coupled via a prism coupling scheme.

et al. derive the conditions for coupling as,⁹⁸

$$\sin \Phi = \frac{l}{n_p k R} \quad (3.1a)$$

$$\Delta \Phi^2 = \frac{\sqrt{n_s^2 - 1}}{n_p^2 k R \cos^2 \Phi} \quad (3.1b)$$

$$\Delta \Theta^2 = \frac{n_s + \sqrt{n_s^2 - 1}}{n_p^2 k R} \quad (3.1c)$$

where n_p is the refractive index of the prism material, n_s is the refractive index of the sphere, $k = 2\pi/\lambda$ is the wavenumber, R is the sphere radius, l is the mode number, Φ is the angle of incidence at the prim surface, $\Delta \Phi$ and $\Delta \Theta$ are the divergence angles of the Gaussian input beam in the Φ and Θ directions (see Figure 3.3).

For a fundamental $l = m$ mode, (3.1a) reduces to $\sin \Phi = n_s/n_p$. In this work a high refractive index prism $n_p \approx 1.77$ at $\lambda = 780 \text{ nm}$ is used. The input angle for coupling to fundamental modes is thus $\Phi \approx 55.21 \text{ deg}$, the divergence angles are $\Delta \Phi \approx 3.11 \text{ deg}$ and $\Delta \Theta \approx 2.29 \text{ deg}$. The energy transfer between the prism and WGMR is reversible, taking place in both directions. The coupling strength is dependent on the distance between the prism and the resonator. The loaded quality factor Q_L for the coupler-resonator system is,

$$Q_L^{-1} = Q_{int}^{-1} + Q_{coup}^{-1}, \quad (3.2)$$

where Q_{int} is the intrinsic quality factor of the resonator and Q_{coup} is the quality factor of the coupler. Maximum energy transfer occurs when the intrinsic Q_{int} equals the coupling quality factor Q_{coup} . In this work, coupling efficiencies of $\approx 40 - 70\%$ were routinely achieved and hence coupled input powers of $60\text{-}100 \mu\text{W}$ were achieved.

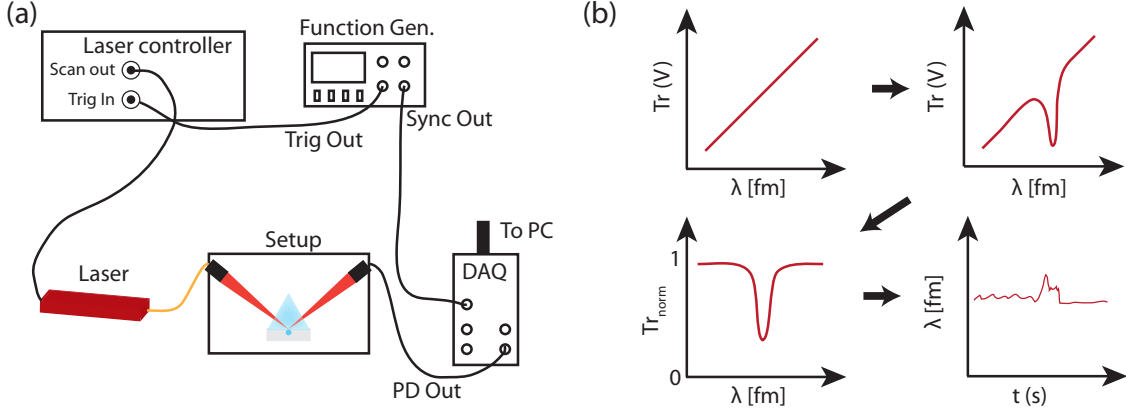


Figure 3.4. (a) Wiring diagram of the setup for acquiring the WGM spectra. (b) Illustrations of the different stages in the acquisition. First, the photodetector (PD) output during a piezo up-scan without WGM coupling is recorded. Then, light is coupled into the WGMs and a transmission dip is obtained. The PD output with the WGM dip is normalized using the background PD output. Finally, the position and full-width-at-half-maximum (FWHM) of the transmission dip are extracted for each piezo up-scan using the algorithm presented by Baaske and Vollmer.⁹⁹

3.4 Acquisition of the WGM spectra

The complete WGM spectrum is obtained by scanning the external cavity diode laser (EDCL, TA Pro 780, Toptica GmbH, Munich, Germany) at a scan rate of 50 Hz. Figure 3.4a shows the wiring diagram of the setup. The piezo scan controller of the EDCL is triggered using a function generator (Agilent 33500B) at 50 Hz. The scan controller then provides symmetric triangular waveforms as input to the piezo of the EDCL. The data acquisition (DAQ, National Instruments PCI 6132) is synchronized to the scanning using the SYNC OUT of the function generator. Figure 3.4b shows sketches of the different stages in the acquisition of the WGM time traces. First, the photodetector voltage (PD) out is recorded without coupling to WGMs to obtain the background level. Then, WGMs are initially identified as transmission dips by a large scan bandwidth of ≈ 50 GHz and/or using a manual coarse tuning of the laser grating. The bandwidth is reduced to 2 – 5 GHz around the desired WGM transmission dip for experiments as shown. The PD output is then normalized with the background to obtain a normalized transmission spectrum. Finally, a centroid fitting algorithm is used to identify the resonance position and full-width-at-half-maximum (FWHM) of the WGM transmission dip. A Labview program developed by Martin Baaske is utilized for acquiring the raw WGM spectra and the estimation of the position and width of the WGM resonance. A detailed description of the algorithm is provided in Supplementary Section 1 of Baaske and Vollmer.⁹⁹

3.5 Implementation of the Pound-Drever-Hall lock

High bandwidth (MHz) data acquisition is performed by locking the laser to the WGM transmission dip using a Pound-Drever-Hall (PDH) lock. More details on the PDH lock is provided

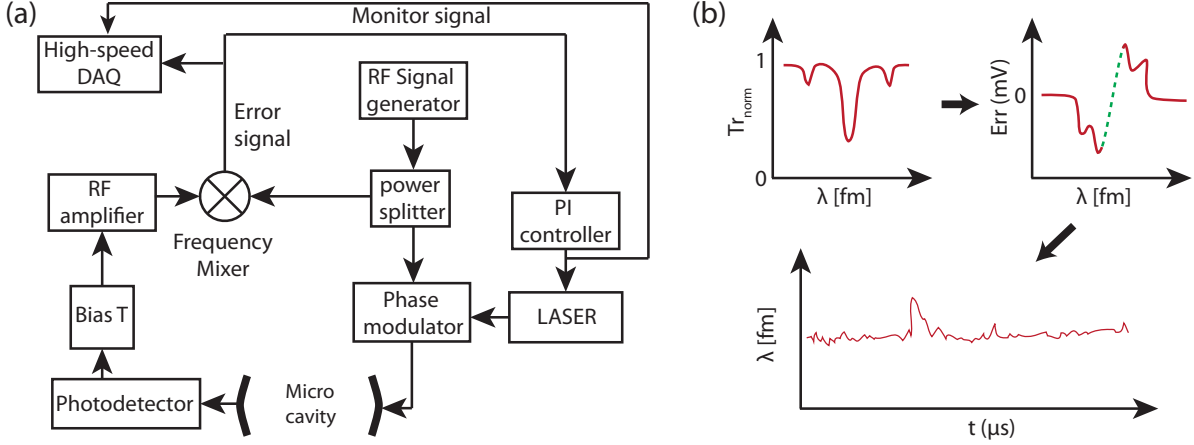


Figure 3.5. (a) Schematic of the circuit for realizing the PDH lock. (b) Illustration of the various stages in acquisition of the WGM resonance position using the PDH lock-in.

in Chapter 6. The schematic of a circuit for realizing a PDH lock is shown in Figure 3.5a. The input from the laser is modulated using an electro-optic phase modulator (EOM, Photline NIR-MPX800-LN-05, iXblue Photonics) to add side-bands on the WGM transmission dip as shown in Figure 3.5b. An RF generator (SMC100A, Rhode & Schwarz, Germany) is used as the local oscillator to drive the EOM. The signal from the RF generator is split using a 50:50 power splitter (ZMSC-2-1+, Minicircuits Inc., USA) and used as the local oscillator for the frequency mixer (ZLW-2, Minicircuits Inc., USA). The transmitted light from the prism is collected using a Silicon amplified photodiode (PD015A, Thorlabs Inc., USA) and split using a Bias-Tee (ZFBT-4R2G+, Minicircuits Inc. USA). The low-frequency component is used for aiding in setting up the lock, while the RF component is amplified again using a low-noise RF amplifier (ZX60-P103LN+, Minicircuits Inc., USA). The amplified signal is then mixed with the local oscillator using the frequency mixer to obtain the error signal as shown in Figure 3.5b. The linear part of the error signal (green, dashed) is then used as feedback to lock the laser to the WGM frequency using a high-speed PID controller (FALC or Digilock, Toptica Photonics GmbH, Germany). The WGM position information is then obtained real-time with a μs time resolution as sketched in Figure 3.5b.

3.6 Data acquisition and analysis

A graphical user interface is developed in MATLAB (Mathworks Inc, USA) for processing the WGM time traces. First, drift correction is applied to remove the slow variation of the resonance position ($\Delta\lambda$) if required. The drift of $\Delta\lambda$ occurs due to slow variation of temperature and pressure in the sample chamber. In the case of the PDH signal, most of the drift is automatically accounted for by the PID feedback to the laser. However, large amplitude changes in pressure and temperature are still measured by the error signal. A first-order Savitzky-Golay filter¹⁰⁰ with a window length depending on the sampling rate is applied to the signal.

Figure 3.6a shows the WGM resonance time traces obtained after drift correction has been

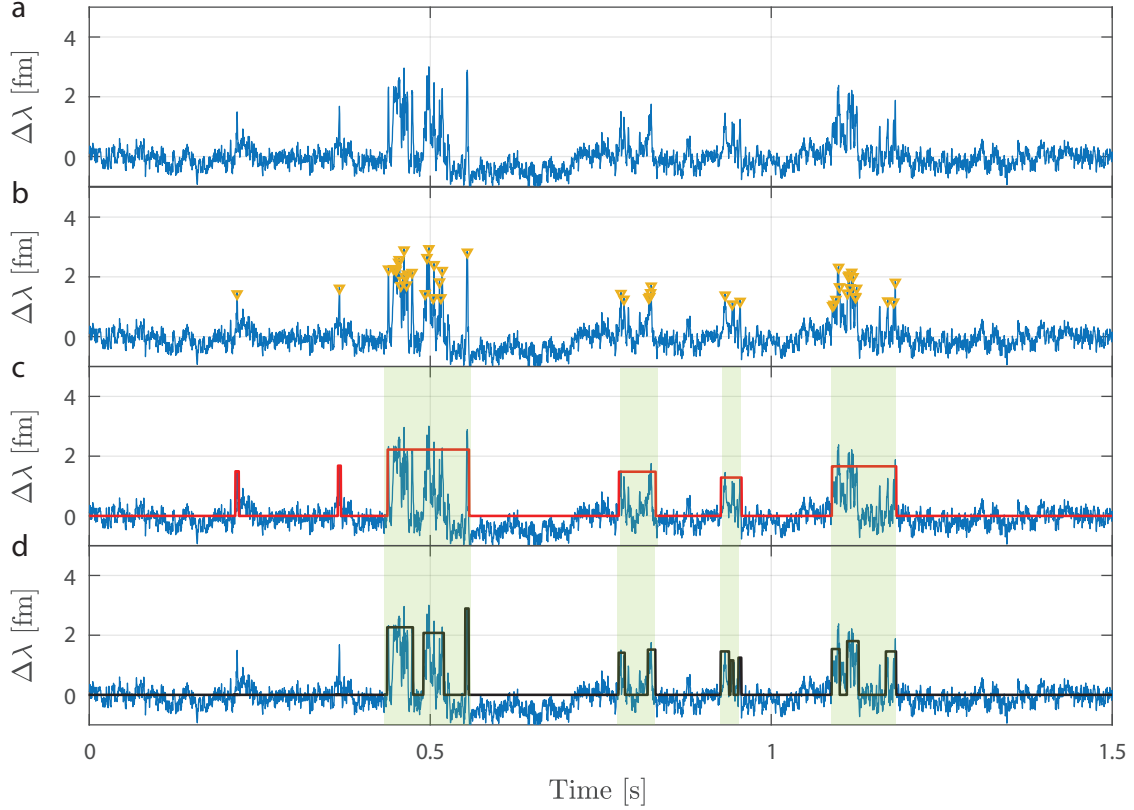


Figure 3.6. a) WGM time traces after drift correction. (b) Individual peaks detected using the peak-detection algorithm. (c) Grouped peaks (solid line) with a time threshold of 50ms. (d) Re-grouping peaks to identify sub-domains with a smaller grouping threshold of 20 ms.

applied. Next, a peak detection algorithm based on the MATLAB function *findpeaks* is used to find the $\Delta\lambda$ values corresponding to single-molecule events. The 'spike' like transitions seen in Figure 3.6a are defined as the signals. Hence, the signal is similar in character to the noise but has a higher amplitude. We quantify as signal peaks, all 'spikes' with amplitude higher than $3 - 5\sigma$ (where σ is the standard deviation of the background). The value of σ is evaluated by dividing the WGM time trace into windows of N points and evaluating the standard deviation of each N -point window. The value of N is set between 10 – 1000 depending on the frequency of the data acquisition, where higher values are set for higher DAQ frequencies. The minimum value of the standard deviation obtained is taken as the σ of the background.

Then, the threshold for detecting peaks using *findpeaks* is chosen manually between $3 - 5\sigma$. Figure 3.6b shows the peaks detected in a segment of the WGM time trace. The triangles show all the individual peaks detected above the threshold. The detected peaks are then classified into single-molecule 'events'. A single molecule 'event' defines the set of signal peaks that belong to one set of interactions. The detected peaks are coalesced into 'events' using a nearest-neighbor search based on a grouping threshold. Essentially, any consecutive peaks within a time separation of Δt are coalesced into one single-molecule 'event'. The grouping threshold Δt used in this work is between 50 – 150 ms. Figure 3.6c shows the peaks detected from Figure 3.6b grouped into single-molecule events using $\Delta t = 50$ ms. Further, single-molecule events can contain sub-domains. These are extracted by using a smaller grouping threshold of

10 – 30 ms (Figure 3.6d). The source code of the GUI can be obtained from https://github.com/ssubram905/WGM_DataAnalysis.git.

3.7 Standard protocol for single-molecule experiments

The protocol for utilizing the sensor for single-molecule detection varies depending on the experiment. However, a standard framework can be provided that can be adapted to individual experimental requirements. Figure 3.7 shows a sketch of the various steps in the standard protocol for performing single-molecule experiments. The steps are as follows:

- A glass microsphere with a diameter of $\approx 80 \mu\text{m}$ is fabricated using the protocol described in Section 3.2. The resonator is then placed in the setup and aligned to the optical beam to enable coupling to WGMs.
- Commercially available plasmonic gold nanorods are attached to the microsphere from a suspension of gold nanorods. The gold nanorods are coated with either a positive, negative, or neutral surfactant. For positively coated nanorods, attachment is performed directly to bare resonators at a solution pH of 1.6. For neutral or negatively coated nanoparticles, an intermediate positive coating is applied to the resonator using a monolayer of amino silane. Excess gold nanorods are removed and the sample chamber is washed multiple times to remove the remaining nanorods.
- Depending on further experimental requirements, a monolayer of anti-fouling polymer usually containing long side chains of polyethyleneglycol (PEG) is added to the regions without gold nanoparticles to prevent any biomolecules from attaching to the microsphere surface. The functionalization with PEG can be applied in different ways depending on the charge on the resonator surface and gold nanorods. When bare resonators (negative charge on glass) and CTAB coated nanorods (positive charge) are used, a positively charged molecule, PLL-g-PEG (5 KDa PEG, SuSoS AG, Switzerland) is used for functionalization. After the immobilization of the the gold nanorods, the resonator is submerged in a solution of approximately $2 \mu\text{g/ml}$ of PLL-g-PEG in 20 mM HEPES, pH 7.4 for 30 mins. The resonator is then washed with DI water to remove any loosely bound PLL-g-PEG. When aminosilanized resonators (positive charge and free amine group on glass) and citrate capped nanorod (negative charge on nanorods) are used, a 100nM solution of PEG containing succinimidyl carboxymethyl ester (NHS-PEG, JKA3016-1G, Sigma Aldrich) in 20mM HEPES, pH 7.4 is used. The NHS ester reacts with the free primary present on the glass surface.
- Single molecules of a linker/molecule 1 with either thiol or amine functionalizations are attached to the gold nanoparticles using different buffers. The type and pH of buffers depend on specific requirements of the experiment and are provided in later chapters.

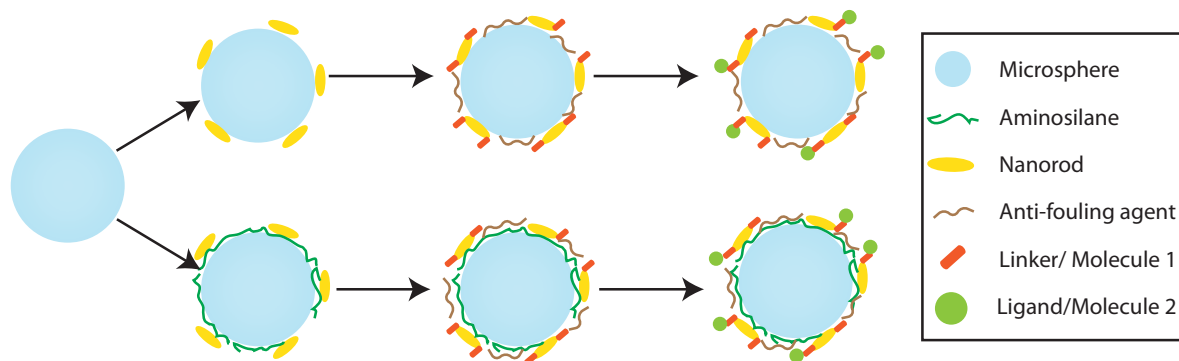


Figure 3.7. Sketch of the standard protocol of single-molecule experiments using the optoplasmonic sensor. First, the microsphere is fabricated using a CO_2 laser melting method. Then, plasmonic gold nanoparticles are typically attached electrostatically from a solution either with or without amino-silanization of the sphere. Next, single thiolated or amine-functionalized linker molecules are attached to the gold surface. Finally, the interaction of the biomolecule of interest with the linker or the gold surface is studied. This final step can be extended by forming a cascade of the molecule on the gold surface similar to the previous step.

- The sample chamber is rinsed and the next buffer is added for further experiments. The ligand/molecule 2 is added to the sample chamber and the interactions of the ligand with the linker are monitored via shifts in the WGM. The previous steps are repeated to form a cascade of molecules on the gold nanoparticle surface if required.

Table 3.1 lists the common nanorod functionalizations used for immobilizing the nanorods on the resonator. The pros and cons of each functionalization are also listed. Typically, CTAB (Cetrimonium bromide) or citrate capped nanorods are easily available via commercial sources. MPTMS ((3-Mercaptopropyl)trimethoxysilane) functionalized nanorods have to be synthesized in the lab starting from citrate capped nanorods and exchanging the ligand. CTAB capped nanorods are used in this work as they can be attached via a one-step immobilization procedure. This reduces measurement time significantly while increasing the likelihood of obtaining a high Q resonator before nanorod attachment. Citrate capped resonators require the resonator surface to be pre-functionalized with aminosilanes. This process can result in reduction of the Q due to non-uniform coating of the aminosilanes. Additional issues with aminosilanization of the resonators arise due to the high positive charge on the surface. Biomolecules having negative charged regions attach to the resonator surface in bulk further reducing the Q . Hence, anti-fouling agents have to be added to the resonator. However, perfect coverage of the surface with an anti-fouling agent is very difficult.

Table 3.1. Immobilization of nanorods with different surface functionalizations, and their pros and cons.

Nanorod functionalization	Immobilization method	Pros	Cons
CTAB	Van der Waal's/ Electrostatic	Simple one-step process Relatively stable over pH 3-8 Well tested protocols for SM studies in lab	Not stable above pH 8 CTAB prevents easy binding of molecules CTAB toxic to many biomolecules
MPTMS	Covalent	High stability over the entire pH range Molecules of interest can be pre-functionalized	Multi-step process Nanorods functionalization to MPTMS required MPTMS surface density tuning is tricky
Citrate	Electrostatic/ covalent	Very stable over large pH range Citrate allows easy binding of molecules Most protocols in the literature use citrate capped nanorods	Silanization required. Multi step process Silanization often ruins Q Positive charge on resonator. Screening is difficult.

Chapter 4

Sensing with WGMs: Nanoparticles to single molecules

This chapter provides a first look at sensing single entities using WGMs. First, we study the interaction of small gold nanorods with the WGM and show the dependence of the WGM wavelength shifts on the polarisability of the particles. Next, the assembly of the gold nanoparticles with different surface coatings on the WGM is presented. Then, we establish the single-molecule detection capabilities of the WGM-plasmonic hybrid system by detecting the binding of small thiolated molecules to the gold nanorods. Finally, the interaction of single molecules (DNA-hybridization) is monitored using the sensor to showcase the ability of the sensor to monitor more complex single-molecule interactions.

4.1 Detection of single gold nanoparticles

As a first step towards detecting single molecules, we detect the diffusion of plasmonic gold nanoparticles in an aqueous medium. The fractional shift of the WGM due to the presence of a small sub-wavelength nanoparticle is proportional to the polarizability of the particle according to (2.13). Hence, gold nanoparticles with their large polarizability are relatively simple to detect using the WGM sensor. A spherical WGM microcavity of diameter approximately $82\ \mu\text{m}$ was fabricated by the procedure described in Section 3.2. The resonator was then immersed in a sample chamber containing $400\ \mu\text{l}$ de-ionized (DI) water and WGMs were excited using a prism coupling setup (see Section 3.1). Plasmonic gold nanorods with LSPR $\approx 750\ \text{nm}$ (A12-10-CTAB-250, Nanopartz Inc., USA) were injected into the sample chamber to a final concentration of $1.2\ \text{pM}$. The WGM spectra were obtained by scanning a tunable EDCL at a rate of $50\ \text{Hz}$ in a small bandwidth around the WGM resonance. Figure 4.1a plots the WGM spectra obtained before and during the diffusion of a single gold nanorod across the evanescent field of the WGM. The initial WGM transmission spectrum (blue) shifts and broadens (orange) when a gold nanorod interacts with the evanescent field of the WGM.

The large deformation of the WGM spectrum from a single Lorentzian line shape is due to the

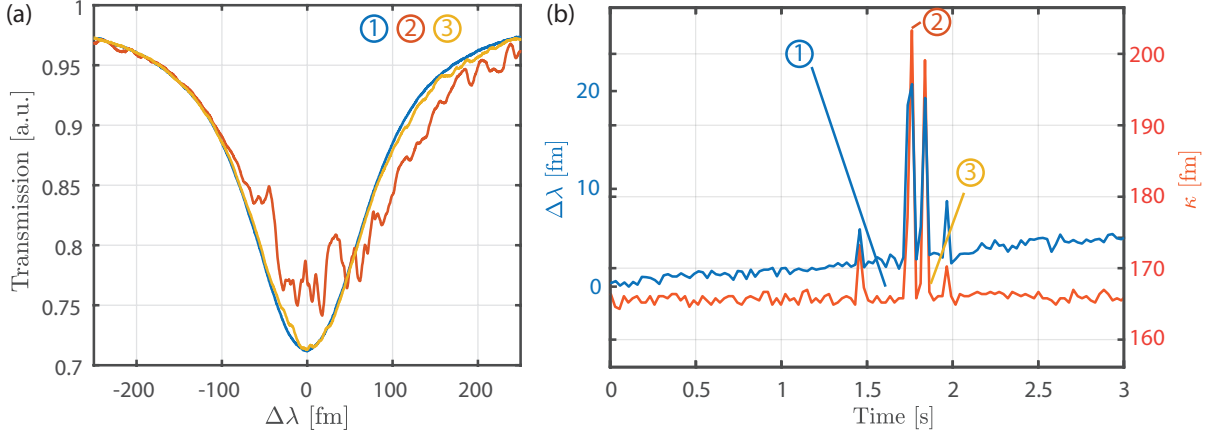


Figure 4.1. (a) WGM transmission spectra measured at different times during the diffusion of gold nanorods across the WGM cavity surface. (b) Time traces of the WGM resonance wavelength (blue) and resonance FWHM (orange) during the interaction of gold nanorods. The times of the extracted WGM spectra in (a) are denoted by numbers.

fast diffusion of the nanorod (rate of diffusion \gg laser scan rate). The complex line shape results from the different overlaps of the nanorod with the evanescent field as it moves across the WGM within one laser scan. When the gold nanorod is further away from the evanescent field of the WGM, the transmission spectrum returns the original position (Figure 4.1a, yellow). Figure 4.1b plots the time traces of the WGM resonance position and FWHM estimated using a centroid fitting algorithm as described in Section 3.4. The peaks observed in the time traces indicate the interaction of the gold nanorods with the WGM. The amplitude of the peaks is proportional to the polarizability of the nanorod at the WGM resonance wavelength and the electric field intensity at the particle's position according to (2.13) to (2.15). Since the solution of the nanorods contains a distribution of nanoparticles with slightly different polarizabilities, the influence of the polarizability and the electric field intensity cannot be separated just using resonance shifts from a single WGM.

4.1.1 Dependence of the WGM wavelength shifts on the polarizability of nanoparticles

In the previous section, we saw that the interaction of gold nanoparticles with the evanescent field of the WGM causes a shift in the WGM resonance position and FWHM. According to (2.13), the shift in the resonance position $\Delta\lambda$ is proportional to the real part of the polarizability of the nanoparticles. Hence, the $\Delta\lambda$ is positive or negative depending on $\Re(\alpha)$ of the nanoparticle. For asymmetric gold nanoparticles such as gold nanorods, the real part of polarizability along the longitudinal axes changes sign at the LSPR. Figure 4.2a plots the value of $\Re(\alpha)$ for ellipsoidal gold nanorods with LSPR from approximately 650 – 1064 nm calculated using (2.27). Here, the dimensions of the ellipsoidal nanoparticles were $a_1 = 5$ nm, $a_2 = 3$ nm and aspect ratio $e = 2.65, 3.5, 3.8, 6.3$ for the nanoparticles with longitudinal LSPRs approximately 650, 750, 780 and 1064 nm, respectively. The typical resonance wavelength of the WGM resonance used in our experiments (green vertical line) is also plotted for reference. The plot shows

that $\Re(\alpha)$ changes sign from negative to positive at the longitudinal LSPR wavelength. Hence, for a WGM with $\lambda_{WGM} \approx 780$ nm, gold nanorods with longitudinal LSPR < 780 nm provide predominantly positive shifts while gold nanorods with LSPR > 780 nm provide predominantly negative shifts and zero shifts for LSPR ≈ 780 nm. A small amount of positive shifts are observed for nanoparticles with LSPR > 780 nm. These positive shifts arise mainly due to the excitation of the transverse LSPRs of the nanoparticles. Due to the rotational diffusion¹⁰¹ of asymmetric nanoparticles such as gold nanorods in solution, different axes of the nanoparticle may align with the polarization of the WGM evanescent field. The polarizability of the nanoparticle along the transverse direction is positive (since the LSPR occurs at a lower wavelength as for spherical gold nanoparticles shown in Figure 2.11) and hence results in positive shifts when the shorter axes aligns with the WGM polarization. A small fraction of the positive shifts may also arise due to the heterogeneity of the sample, especially for the nanorods with longitudinal LSPR at 780 nm.

Figure 4.2b plots the histograms of the mean peak heights $\overline{\Delta\lambda}$ measured by a WGM microsphere resonator of diameter approximately 85 μm . CTAB coated plasmonic nanorods with different LSPRs (A12-10-650-CTAB, A12-10-750-CTAB, A12-10-1064-CTAB) were purchased from Nanopartz Inc., USA. Polyethylene glycol (PEG) capped nanoparticles (Au-800-PEG) were purchased from NanoComposix, USA. The CTAB capped nanorods were synthesized to a diameter of 10 nm and the lengths were varied to obtain different aspect ratio that provides different longitudinal LSPRs. The PEG capped nanorods were synthesized with a diameter of 14 nm. For the nanorods with LSPR ~ 650 nm, the shifts are predominantly positive as the mean LSPR is at a wavelength much lower than the WGM wavelength of ≈ 780 nm. As the mean LSPR of the nanorods increase, the percentage of negative shifts increases with the majority of the events producing negative shifts for nanorods with mean LSPR ~ 1064 nm. The histograms in Figure 4.2b show the validity of (2.13) in describing the resonance shifts of WGM due to small sub-wavelength nanoparticles. Hence, optical WGMs can be used for the qualitative characterization of nanoparticle polarizabilities.

4.1.2 Binding of gold nanoparticles to the WGM cavity

In the previous section, we showed that optical WGMs can be utilized to detect nanoparticles with relatively large polarizabilities such as plasmonic gold nanoparticles. Similarly, other large dielectric entities such as viruses (size ~ 200 nm, and dielectric particles (size ~ 100 nm) can also be detected using a bare WGM sensor.⁵⁵ However, detection of extremely small nanometer-sized objects such as single proteins or DNA is beyond the sensitivity of a bare WGM resonance shift due to practical limitations of the resonator quality and noise sources such as thermo-refractive noise and laser frequency/phase noise (see Section 2.1.2). Hence, an enhancement of the signal is required. This enhancement can be provided locally by plasmonic gold nanoparticles excited by the evanescent field of the WGM. For reliable detection of single biomolecules, the gold nanoparticles have to be attached to the WGM cavity surface robustly.

Many different protocols are available in the literature to attach nanoparticles on glass sur-

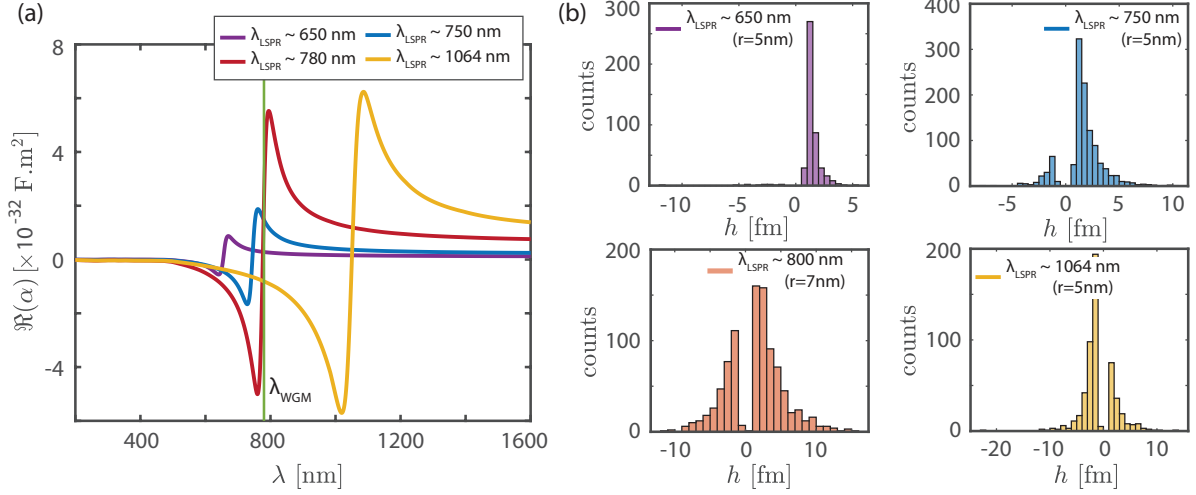


Figure 4.2. (a) Real part of the polarizability of plasmonic gold nanorods along the long axes with different longitudinal LSPRs. (b) Histogram of the event heights measured for the interaction of gold nanorods with different aspect ratios to a WGM microcavity excited at approximately 780 nm.

faces,^{102,103} however these fall broadly into the categories of electrostatic or covalent attachment procedures. The electrostatic binding schemes involve modifying the surface charge of the WGM cavity temporarily using different buffers or permanently using monolayers of charged polymers. The gold nanoparticles are used as purchased to attach them to the WGM cavity surface. The covalent binding procedures on the other hand involve modifying the WGM cavity surface permanently to contain groups such as amines or thiols exposed to the solvent and the gold nanoparticles are also modified to a complementary chemical species that form robust covalent bonds with the surface amine or thiol groups. Charge based immobilization is the simpler method due to the reduced number of steps resulting in a higher percentage of successful attachments. However, the stability of the attached nanoparticles is lower than covalently attached nanoparticles and hence the range of physiological conditions for use of these methods is restricted.ⁱ

In this thesis, we use the electrostatic method of attachment with the protocol described below unless explicitly specified otherwise. The plasmonic gold nanoparticles used in this work are rod-shaped particles that are synthesized in solution and covered with a surfactant, typically Cetrimonium bromide (CTAB), to avoid agglomeration in solution. It is well known that CTAB coated gold nanoparticles are positively charged in solution at a neutral pH due to the formation of a CTAB bilayer on the gold nanorod surface.¹⁰⁴ The CTAB bilayer provides a net positive charge to the nanoparticles due to the positively charged N head group. Nonetheless, the binding efficiency of the nanoparticles to the glass WGM cavity is extremely low at a neutral pH where glass is negatively charged. This is possibly due to the presence of the negatively charged Bromide counter-ion with a weak dissociation constant at neutral pH.¹⁰⁵ Baaske *et al.*,⁸¹ found that a reduction in the pH of the solution to approximately 1.6 resulted in the effective binding of the gold nanoparticles to the glass microcavity surface. The exact mechanism of the binding

ⁱsee Appendix B for notes on the stability of immobilized nanoparticles in buffers containing surfacts such as sodium dodecyl sulfate (SDS).

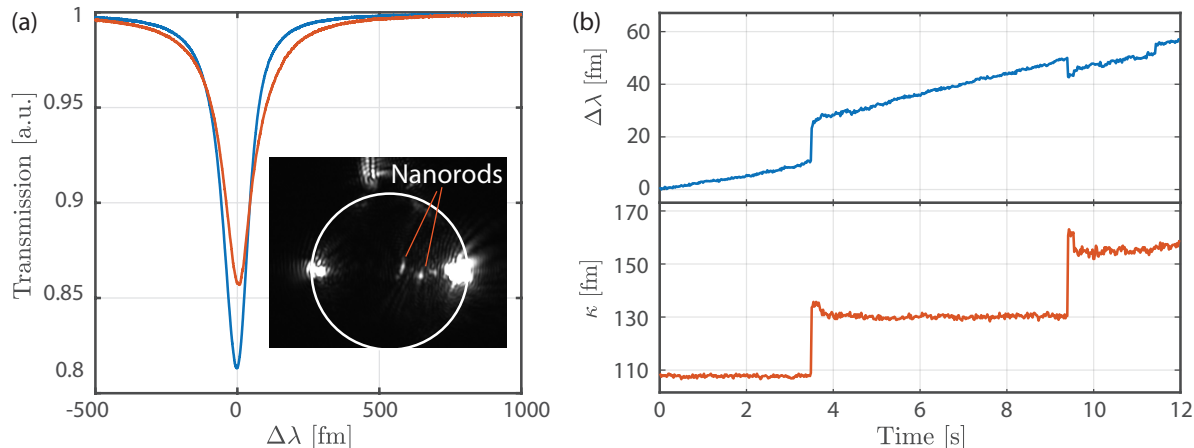


Figure 4.3. (a) WGM spectra before (blue) and after (orange) the binding of a plasmonic gold nanorod. Inset shows a photograph of the spherical microcavity resonator with the scattering from the gold nanorods. (b) Time traces of the WGM resonance wavelength and FWHM showing step like transitions indicating the binding of single gold nanorods.

of CTAB coated gold nanorods to the glass surface is not completely understood. The working hypothesis is that the neutral charge of the glass surface at this low pH enables the nanorods to get close to the glass surface to attach via Van der Waals interaction.

Figure 4.3a plots the WGM spectra before (blue) and after (red) the binding of a single CTAB coated gold nanorod at a $\text{pH} \approx 1.6$. The final nanorod concentration in the sample chamber was 500 fM and the pH of the solution was reduced to 1.6 by addition of 24 mM HCl. The inset of Figure 4.3a shows a photograph of the WGM microsphere cavity imaged in the setup. The outline of the cavity is marked with a white circle for reference. The scattering from the attached nanoparticles is visible in the photograph. Figure 4.3b plots the time traces of the $\Delta\lambda$ and κ . The step-like transitions in the time traces indicate the binding of a single gold nanorod. The steps in $\Delta\lambda$ can be positive or negative depending on the sign of the real part of the polarizability, whereas the steps in κ are typically positive as the losses increase with the addition of more particles. For single-molecule experiments, typically 5-10 gold nanorods are attached and the process is stopped by removing the solution of gold nanorods from the sample chamber. The sample chamber is then rinsed thrice with ultra-pure water for further experiments.

4.2 Single-molecule detection using a plasmon-enhanced WGM microcavity

4.2.1 Immobilization of single molecules

Detection of single molecules is performed using the WGM-plasmonic hybrid sensor assembled using the procedure described in the previous section. After rinsing the sample chamber post attachment of the gold nanorods, the sample chamber is filled with 300-400 μl of single-molecule

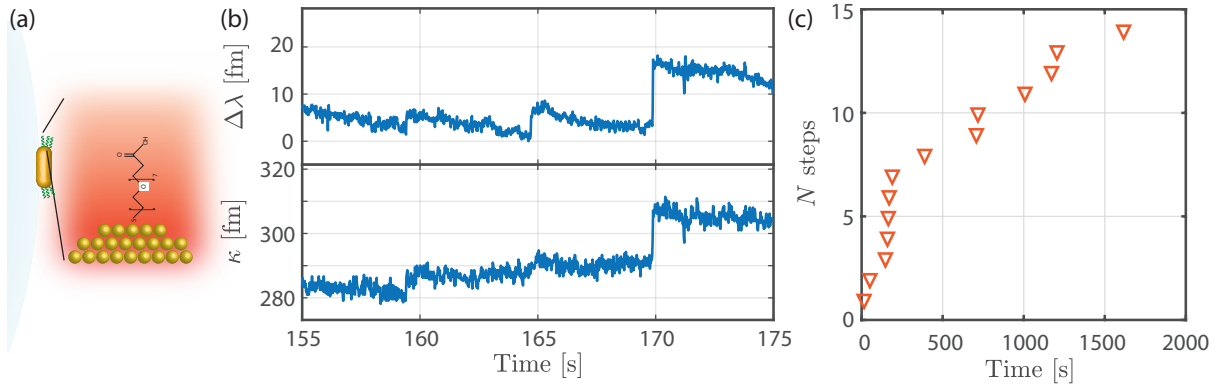


Figure 4.4. (a) Illustration of the binding of single thiolated-PEG molecules to gold nanorods attached to the WGM microcavity. (b) Time traces of the WGM resonance position and FWHM showing step like transitions due to binding of single thiolated-PEG molecules. (c) Number of binding events over time for the binding of single thiolated-PEG molecules.

loading buffer. Various protocols for functionalizing gold nanoparticles are available in literature. Commonly, molecules containing free thiol (SH) or amine (NH_2) groups are utilized. Alternatively, charge-based electrostatic functionalization schemes are also available. The covalent binding methods are preferred as these provide more robust and specific immobilization of the molecules. Although, thiol and amine species are known to covalently bind to gold easily,³⁷ the protocols vary vastly depending on the composition of the molecule as a whole.¹⁰⁶ In general, the binding of molecules to the plasmonic gold nanoparticle involves first removing or destabilizing the surfactant (CTAB) layer.

For the thiol modified molecules typically used in this thesis, loading buffers either containing 0.02% sodium dodecyl sulphate (SDS) or a sodium citrate-citric acid buffer (also known as citrate buffer) at $\text{pH} \approx 3$ with 1 M NaCl are used. Alternatively, a ultra-low pH method $\text{pH} \approx 1.8-2$ reported by Kim *et al.*⁵¹ was utilized. This method was later abandoned due to the formation of DNA aggregates under ultra-low pH conditions. It has to be noted here that gold nanoparticles attached electrostatically to the WGM microcavity using the protocol described in the previous section might become unstable in SDS containing buffers (see Appendix B). The citrate buffer avoids this issue of nanorod instability. Although, the citrate buffer works well for small thiolated polymers, the efficiency for DNA loading is dependent on various factors and careful design of the DNA sequence is required.¹⁰⁶ Additionally, most proteins containing thiol groups cannot be immobilized using this method due to the denaturation of proteins at low pH conditions.¹⁰⁷ However, owing to the relatively large size of proteins, immobilization of most proteins is straightforward even under physiological conditions.

Figure 4.4a illustrates the binding of single sub-kDa molecules of thiolated-PEG (M.W. 458.7 g/mol, $\text{HS}-(\text{PEG})_7-\text{COOH}$, ThermoFisher Scientific, USA) to the gold nanorods attached to a WGM microcavity. A WGM microcavity of diameter $82 \mu\text{m}$ was used for this experiment. CTAB coated gold nanorods were attached to the microcavity as described previously. A solution containing 0.02% SDS at pH of 3 with 1 M NaCl was used as the loading buffer. The thiolated-PEG molecules were prepared to a stock concentration of 1 mM in ultra-pure water. The thiolated-PEG was then mixed with Tris(2-carboxyethyl)phosphine (TCEP) at a ratio of

1:1 and left for 15 mins just before injected into the sample chamber. TCEP acts as a reducing agent to prevent formation of disulfide bonds in solution. The sample was then injected into the chamber containing the loading buffer to a final concentration of $1\ \mu\text{M}$. Figure 4.4b shows the time traces of the WGM resonance position $\Delta\lambda$ and FWHM κ . The distinct step-like transitions in the time traces indicate binding of single molecules of thiolated-PEG as reported previously.^{51,80} The fractional shift in the λ can still be described by (2.13), assuming that the gold nanorod only acts to locally enhance the electric field $\mathbf{E}(\mathbf{r}_p)$ experienced by the molecule as described in Section 2.1.2. However, the shift in FWHM κ is surprising as the losses induced by small single molecules are negligible.¹⁰⁸ The shift in κ arises from the phenomenon of mode splitting which will be discussed in detail in Chapter 5. Figure 4.4c plots the number of molecules attached over time. The step heights were estimated semi-manually using the MATLAB program described in section 3.6. The threshold for the minimum step height is chosen to be $> 5\sigma$, where σ is estimated as described in section 3.6.

It can be seen from the plot that the time between events becomes larger as more molecules bind leading to a saturation behavior. This is expected as the number of available sites for molecules to bind reduces with each binding event. It has to be noted here that the steps here correspond to a fraction of the actual number of thiolated-PEG molecules attached to the nanorods. For the HS-PEG₇-COOH molecules used here, a surface binding density of 4.29 molecules per nm² has been reported.¹⁰⁹ Hence, approximately 1000 molecules can be attached to the tip of each nanorod. Due to the small size of the HS-PEG₇-COOH, only a small fraction of the binding sites on the tips of the gold nanorods provide the necessary enhancement for step signals above the background noise. These binding sites are likely located on bumps or troughs on the tips of the gold nanorod where further enhancement of the near-field intensity is achieved.^{80,81}

4.2.2 Measuring the hybridization kinetics of DNA oligonucleotides

Although detecting the binding of single molecules to gold nanoparticles is a significant step, a more useful capability in terms of a biosensor is the ability to detect the interaction of multiple molecules/chemical species in solution. In this section, we will show the ability of the plasmonically enhanced-WGM sensor for detecting interactions of single molecules by measuring the hybridization kinetics of single DNA oligonucleotides. It is now well known that DNA is a molecule that stores the genetic information of living organisms, and the double helix structure of double-stranded DNA (dsDNA) is well established. The ability to synthesize arbitrary strands of small DNA sequences known as DNA oligonucleotides¹¹⁰ has found numerous applications in the fields of molecular biology, biotechnology, and biosensing. DNA oligonucleotides have also been utilized as sensor probes in single-molecule techniques such as DNA-PAINT, where fluorescently labeled single-stranded DNA are utilized together with their complementary strands for obtaining super-resolution images of samples.^{111,112}

A single strand of DNA oligonucleotide is made up of nucleotides (*nts*) containing 4 nitrogenous bases (adenine (A), thymine (T), cytosine (C), or guanine (G)) attached to a sugar-phosphate

backbone. The *nts* are covalently attached via a phosphodiester linkage. The double helix structure of double-stranded DNA is formed via hydrogen bonds between the nitrogenous bases. The complementary base pairs (bps), (A), and (T) form two hydrogen bonds, whereas the pairs (G) and (C) form three bonds. Hence, the stability of the double-helix depends on the sequence and length of the DNA. For very short DNA sequences (\sim ten bps) with low amounts of (G, C) pairs or with multiple mismatches in the complementary sequences, the duration for which the two complementary strands hybridize (dissociation time) can be short (\sim s).^{81,111} The dissociation time also depends on the other factors such as the physiological conditions, namely the ionic strength, temperature, and pH of the buffer. By varying the sequence of the oligos and changing the ionic concentration, the kinetics of the hybridization (formation of double-helix) of the two complementary DNA strands can be altered. For measurements in our sensor, complementary DNA oligos with hybridization duration in the range of 0.1 – 1 s are suitable as the data acquisition rate for the laser scan is 0.02 s (see Section 3.4).

Table 4.1 provides the DNA oligo sequences used in this work. The DNA oligos were purchased lyophilized from Eurofins Genomics Germany GmbH. The lyophilized powder was centrifuged at 14000 rpm for 60 s and re-suspended in ultra-pure H₂O to a stock concentration of 100 μ M. The DNA oligo Thiol22 contains a modification at the 5' end to contain a free thiol linker which is attached to the gold nanoparticles. The complementary DNA oligo COMP22M3 contains 3 mismatches to the docking strand marked in red in Table 4.1. The mismatches ensure that the hybridization duration of the DNA is short in the range that is easy to detect using our sensor. The four consecutive (T)'s act as a spacer to separate the DNA from the gold surface to avoid steric effects. Figure 4.5a shows an illustration of the DNA oligo Thiol22 immobilized on the tip of a gold nanoparticle attached to a glass WGM microcavity. The zoom-in shows a sketch of the reversible hybridization of Thiol22 with COMP22M3.

A resonator of diameter 85 μ m was utilized in this experiment and CTAB coated gold nanorods (A12-10-CTAB-750) were attached to the WGM as described in Section 4.1.2. The thiolated DNA oligo (Thiol22) was then immobilized on the gold nanorods in a solution containing 0.02% SDS, pH \approx 3 and 1 M NaCl. The DNA stock solution was pre-mixed with Tris(2 carboxyethyl)phosphine (TCEP) at a ratio of 1:1 for 15 mins before injecting into the sample chamber to a final DNA concentration of 1 μ M. The thiolated DNA was left to react with the nanorods in the sample chamber for 30 mins. The excess Thiol22 was then removed and the sample chamber was rinsed thoroughly thrice with ultra-pure water. Next, 400 μ l of ultra-pure water with 20 mM NaCl was added to the sample chamber. Then, the complementary DNA

Table 4.1. Sequences of DNA oligomers used in our experiments. The DNA oligos were purchased lyophilized from Eurofins Genomics Germany GmbH.

Name	Sequence
Thiol22	5'- [ThiolC6] TTTT GAG ATA AAC GAG AAG GAT TGA T - 3'
COMP22M3	3'- CTC TAT TTC CTT TTC CTG ACT A - 5'

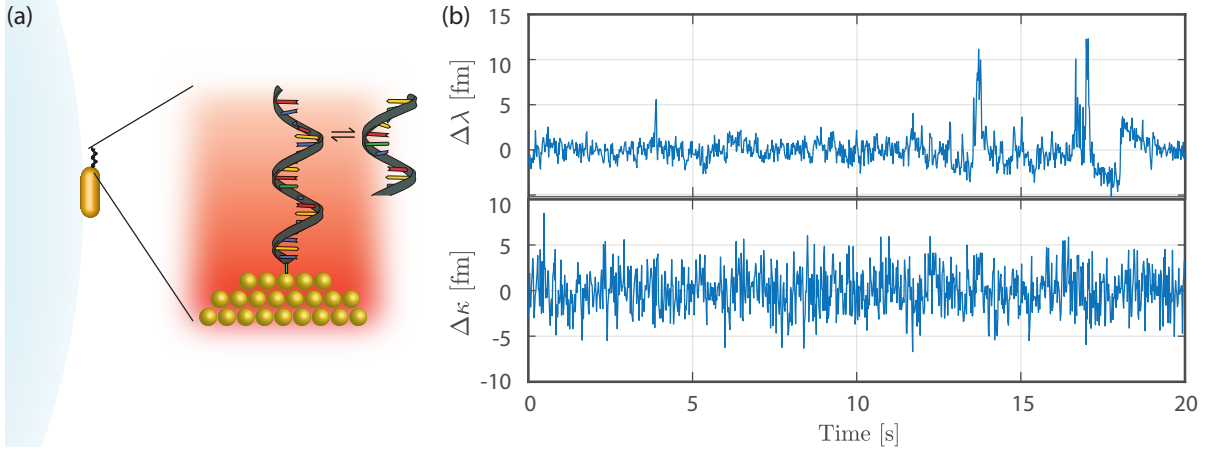


Figure 4.5. (a) Illustration of the hybridization interaction of a single complementary DNA strand with 3 mismatches to a DNA strand immobilized on the gold nanorods. (b) Time traces of WGM resonance wavelength and FWHM for single DNA interaction.

COMP22M3 was added in steps of 200 nM. At each concentration step of COMP22M3, the $\Delta\lambda$ and κ were recorded for 1 hr. Figure 4.5b plots the $\Delta\lambda$ and $\Delta\kappa$ time traces during the interaction of COMP22M3 with Thiol22 on the surface of the gold nanorods. The spike-like transitions in $\Delta\lambda$ indicate the interaction of a single COMP22M3 oligo with the docking Thiol22. These spike-like transitions are classified into 'events' using the algorithm described in Section 3.6. The transient nature of these events indicates that the COMP22M3 oligos only hybridize with the docking strand for short periods due to the mismatch in the sequences of DNA. The variation in the time duration of these interactions denotes the statistical variation of the hybridization kinetics between each single-molecule interaction.

Figure 4.6a plots the probability density function (pdf) histograms of the mean amplitude of the hybridization events at three different concentrations of COMP22M3 from 200 – 600 nM. The corresponding log-normal fits to the data (red, solid), and the 3σ noise threshold (green, dashed) are also plotted for reference. The estimation of the value of σ is as described in Section 3.6. The plots show that the noise floor 3σ increases with increasing concentration of COMP22M3. This is attributed to the saturation of some docking strands due to the high starting concentration of the complementary DNA. Hence, for the peak detection at all concentrations of COMP22M3, the σ estimated at 200 nM of the DNA was utilized. The pdf of the event mean amplitudes closely follows a log-normal distribution as indicated by the fits (red, solid). A log-normal distribution has a probability density function of the form,

$$p(x) = \frac{1}{x\sigma\sqrt{2\pi}} \exp\left(-\frac{(\ln x - \mu)^2}{2\sigma^2}\right) \quad (4.1)$$

with standard deviation σ and mean μ . Log-normal distributions are expected for data where multiple underlying processes contribute to the observed data.^{113,114} Here, two different processes contribute to the signal; (i) Multiple docking strands (Thiol22) are immobilized at different binding sites on the gold nanorods providing different enhancements for the signals, and (ii) for each docking strand the thermodynamic fluctuation of the DNA on the gold nanorod

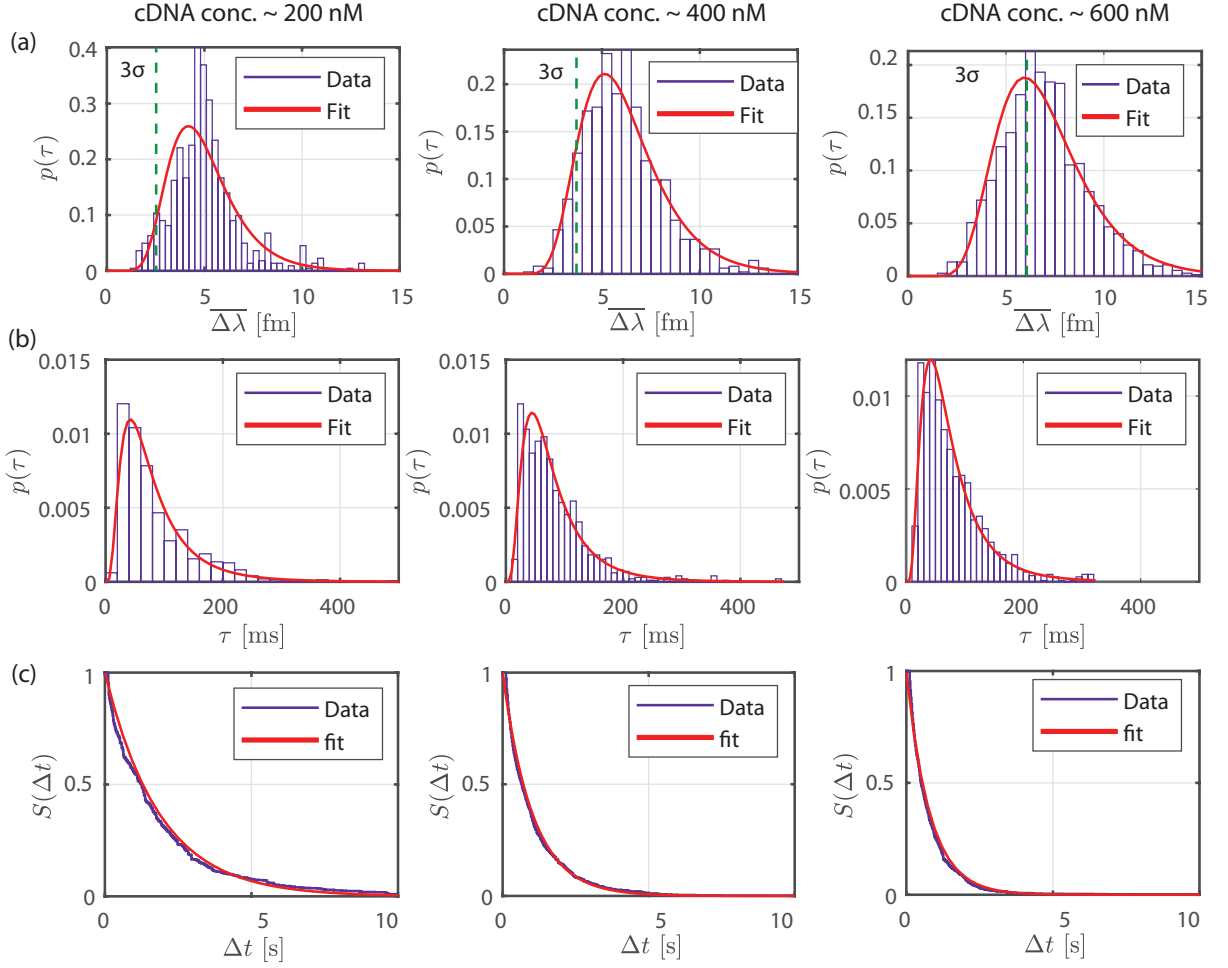


Figure 4.6. (a) Probability density function plotted as histograms of the mean amplitude $\overline{\Delta\lambda}$ of the hybridization events and the corresponding log-normal fits. The threshold value of 3σ (dashed, green) is plotted for reference. (b) Probability density function of the duration of hybridization events τ and the corresponding log-normal fits. (c) Survivor functions of the arrival time between consecutive events and the corresponding exponential fits.

provides different signal amplitudes around a mean fluctuation.

Figure 4.6b plots the histograms of the event duration τ at the three different concentrations of COMP22M3 and the corresponding log-normal distribution fits to the data using (4.1) (red, solid) are also plotted. Again, the log-normal distribution indicates a contribution to the events from multiple processes. The variation of the event duration across the different docking strands likely results in the stretched distribution. The event duration specifies the amount of time for each DNA hybridization event under the experimental conditions. In ensemble measurements, only an average event duration can be obtained, whereas the single-molecule experiments also provide the statistical variation in the hybridization of ssDNA. Figure 4.6c plots the survivor function $S(\Delta t) = P(T < \Delta t)$ of the event arrival times Δt between two consecutive hybridization events. The corresponding exponential fits to the function,

$$p(x) = a \exp(-kx) \quad (4.2)$$

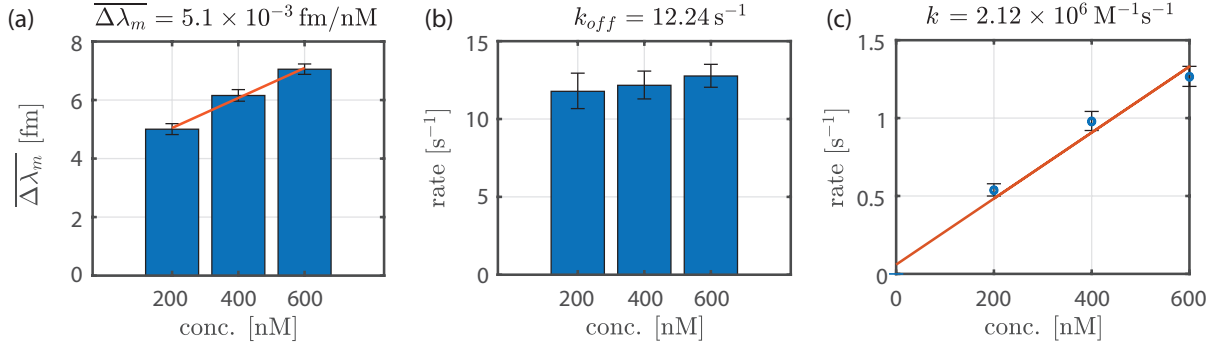


Figure 4.7. Dependence of the various event properties on concentration of COMP22M3. (a) Mean amplitude of events $\overline{\Delta\lambda}$ estimated from the log-normal fits. (b) Mean off-rate $k_{off} = 1/\tau_m$, where τ_m is the mean event duration estimated from the log-normal fit. (c) Mean arrival rate of events $k = 1/\Delta t_m$, where Δt_m is the mean arrival time between two consecutive events estimated from the exponential fit. The error bars plot the standard errors from the maximum likelihood estimation.

are also plotted where k provides the rate of events. The distribution of Δt follows a single exponential (Poissonian distribution) as expected for events occurring randomly and independently in time. The Δt data provide the on-rate of the hybridization events.

Figure 4.7 plots the dependence of the average values of the different event properties on the concentration of COMP22M3. Figure 4.7a plots the concentration dependence of the mean event amplitude $\overline{\Delta\lambda_m}$ estimated using the log-normal fits. The $\overline{\Delta\lambda_m}$ shows a small increase with concentration with a rate of 5.1×10^{-3} fm/nM. This small increase in the $\overline{\Delta\lambda_m}$ is likely due to the increase in the background noise with addition of more complementary DNA. Figure 4.7b plots the off-rate k_{off} of the events measured as $k_{off} = 1/\tau_m$, where τ_m is the mean event duration estimated from the log-normal fit. The off-rate across the three concentrations is constant within the fit errors. This is expected as the mean interaction duration of the hybridization events remains constant with the concentration of the complementary DNA. A mean off-rate $k_{off} = 12.24$ s⁻¹ is calculated from the mean of the off-rates measured at the different concentrations. This provides a mean interaction duration of $\tau_m = 81.7$ ms. The short interaction duration is expected due to the mismatches between docking and complementary strands, and the low salt concentration in the solution.

Figure 4.7c plots the concentration dependence of the rate of arrival of events $k = 1/\Delta t_m$, where Δt_m is the mean arrival time between two consecutive events estimated from the exponential fit. The error bars plot the standard errors from the maximum likelihood estimation. As expected, the rate of arrival of events increases linearly with the concentration of COMP22M3.ⁱⁱ This is characterized by a linear fit (red, solid) to the data with a coefficient of correlation $R^2 = 0.98$. The linear fit provides an association rate $k = 2.12 \times 10^6$ M⁻¹s⁻¹. It has to be noted here that the actual single-molecule on-rate k_{on} cannot be estimated from the data as the actual number of sampled sites (docking strands contributing to the signal) is unknown. The number of sites contributing to the signal is dependent on the local geometry of the gold nanorods and

ⁱⁱA small saturation behavior can be seen at COMP22M3 concentration of 600 nM. However, the data still fits well with a linear model to extract the association rate.

the overlap of the docking strands with the plasmonic near-field. This number is not directly accessible to the WGM-plasmonic sensor.

4.3 Conclusions

In this chapter, we showed the ability of optical WGMs to detect small sub-wavelength objects such as plasmonic nanoparticles and the ability of the WGM-plasmonic hybrid system to detect even single biomolecules and their interactions. Single plasmonic gold nanoparticles are easily detected in solution due to their large real and imaginary part of the polarizability. The diffusion of plasmonic gold nanoparticles across the WGM introduces a shift in the WGM resonance wavelength as well as an increase in the FWHM. The shifts in the WGM spectrum is observed as spike-like transitions in the time traces of the WGM position and FWHM. The WGM spectrum is often distorted from a Lorentzian lineshape due to the fast diffusion (faster than the scanning rate of the laser) of the nanoparticles across the WGM. The direction of the WGM wavelength shift depends on the sign of the real part of the nanoparticle's polarizability at the WGM excitation wavelength. We showed that for gold nanorods with increasing LSPRs from 650 to 1064 nm, the WGM wavelength shifts change from predominantly positive to negative tracking the change in the sign of the real part of the polarizability. Due to the surface coating of the gold nanoparticles, binding of the nanoparticles to the WGM cavity surface does not occur under physiological conditions. Binding of CTAB coated gold nanorods to the WGM was achieved by lowering the pH of the solvent to the isoelectric point of glass, that is, 1.6. The binding of the gold nanorods is observed as step-like transitions in the WGM time traces.

Single-molecule detection using WGMs was achieved by the enhancement provided by the gold nanorods attached to the WGM surface. First, detection of the binding of small sub-kDa molecules via step-like transitions in the WGM time traces was presented. The binding of the small molecules to the gold nanorods is achieved via thiol or amine modification to the molecule. Special loading buffers have to be utilized for the binding of the molecules. The conditions of the buffers vary considerably depending on the molecule of interest. However, typically a low pH (~ 3) and high salt concentration ($\sim 1\text{M NaCl}$) is required for binding of the molecules to the gold nanoparticles. The presence of surfactants such as SDS or Tween 20 also aids in the efficient binding of the molecules. Only a small subset of all the molecules attached to a single gold nanorod is observable using our sensor. This is since only a few binding sites on the tips of the nanorods provide the required enhancement to detect single molecules. Pekcevik *et al.* estimated that approximately 870 ssDNA molecules could be attached to gold nanorods of size $10 \times 38\text{ nm}$.¹¹⁵ However, Kim *et al.* observed only approximately 60 binding events per gold nanorod of a similar size using the WGM-nanorod sensor system.⁵¹ Hence, only a small percentage of molecules ($< 10\%$) attached to the tips of the gold nanoparticles provide signals sufficiently large to be detected using the WGM-plasmonic sensor. Further, the number of attached ssDNA contributing to the signals of hybridization kinetics may be smaller depending on the complementary ssDNA size, and the overlap of the hybridized DNA with the plasmonic near-field.

Once single molecules are attached to the gold nanorods, their interactions with other ligands can be monitored using our sensor. Single DNA hybridization events in the solution were monitored using the WGM-plasmonic hybrid sensor. The hybridization of a complementary DNA strand to a single-stranded DNA oligonucleotide bound to the gold surface could be monitored as spike-like transitions in the WGM wavelength shift. Peaks above 3σ were characterized as signals and the kinetics of the hybridization could be monitored by extracting the amplitudes, duration, and arrival times of the events. As expected for single-molecule events, the arrival times between events were distributed with a Poisson distribution. An exponential fit to the distribution of the arrival times provided the rate of events. Concentration-dependent measurements showed that the rate of events increased linearly with the concentration of the complementary DNA oligonucleotide as expected for independent events. The on-rate for the hybridization events could be estimated using a linear fit to the concentration dependence to be $k_{on} = 2.12 \times 10^6 \text{ M}^{-1}\text{s}^{-1}$. The off-rate of the events could be estimated from a log-normal distribution fit to the event duration. The off-rate was estimated to be $k_{off} = 12.24 \text{ s}^{-1}$. The rates estimated provided a dissociation constant of $K_d = 5.77 \text{ }\mu\text{M}$. The high dissociation constant indicates a low binding affinity of the two DNA strands as would be expected for short strands of DNA with multiple mismatches.

Chapter 5

Single-molecule sensing by effective linewidth shifts of WGMs

5.1 Introduction

Single-molecule detection using WGM based sensors typically depends on monitoring the shift of the WGM resonance frequency over time. The FWHM of the resonance does not usually provide any signals as the imaginary part of the refractive index of most small molecules is negligible at visible wavelengths. In this chapter, we show that an effective change in the WGM linewidth (FWHM) can be obtained for single-molecule sensing. Further, we will see that the change in effective linewidth does not arise from the losses introduced by single molecules. The change in linewidth rather arises from a change in the unresolved frequency splitting of WGMs due to the presence of surface scatterers. Section 2.1 briefly described the origin of frequency splitting in WGMs due to the presence of a single scatterer. This chapter further describes the theory of frequency splitting of WGMs and extends the description to the case of multiple scatterers. Then, experimental results for single-molecule sensing using the effective WGM linewidth as a proxy for frequency splitting are provided. Further, we show that the linewidth shifts are better than the resonance frequency shifts for single-molecule sensing under certain conditions.

5.2 Frequency splitting of WGMs due to the presence of multiple surface scatterers

As previously described in Section 2.1.1, the azimuthal mode number m defines two counter-propagating WGM modes, one for $+m$ and the other for $-m$. In resonators without any

The content of this chapter appeared in Subramanian, S., Vincent, S., and Vollmer, F., “Effective linewidth shifts in single-molecule detection using optical whispering gallery modes,” Applied Physics Letters 117(15), 151106 (2020).

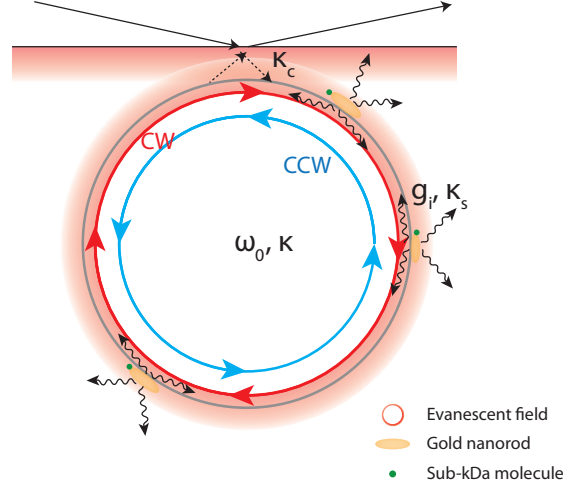


Figure 5.1. Schematic of the coupling of light into the WGM and the cross coupling of clockwise (CW) and counter-clockwise (CCW) modes due to the presence of surface scatterers.

inhomogeneity or scattering, both of these modes are degenerate in frequency. Rayleigh scattering from the gold nanoparticles present in our WGM-plasmonic system causes a transfer of power from the initially coupled mode to the counter-propagating WGM modeⁱ and leads to a frequency splitting of the two modes. The addition of multiple scatterers can cause the splitting to increase or decrease depending on the position of the scatterers. The interference of the counter-propagating WGMs leads to the formation of standing wave modes (SWMs).

Figure 5.1 shows a schematic of the WGM-plasmonic system coupled via FTIR at a prism surface with multiple gold nanorods attached to the surface. Light is initially coupled in the clockwise (CW) direction with a coupling coefficient κ_c and the presence of the gold nanoparticles introduces a coupling into the counter-clockwise direction (CCW) with a rate of g . The coupling between the CW and CCW modes can be described using a coupled mode theory^{116, 117} with the slowly varying envelope approximation.

Let us first consider the simple case of the binding of one nanoparticle to the the cavity in Figure 5.1. The cross coupling of light from the CW to the CCW directions is equivalent to the shift of resonance frequency by the particle and is given by $g = \Delta\omega$ from (2.13). Additionally, the scattering κ_s and absorption losses κ_a are given by (2.15), (2.14). The time varying amplitudes a_{cw} and a_{ccw} can then be given as,¹¹⁸

$$\frac{da_{cw}}{dt} = \left(-i(\Delta - g) + \frac{\kappa_s + \kappa_a + \kappa_0 + \kappa_{ex}}{2} \right) \cdot a_{cw} - \left(ig - \frac{\kappa_s + \kappa_a}{2} \right) \cdot a_{ccw} + \sqrt{\kappa_{ex}} s_{cw} \quad (5.1a)$$

$$\frac{da_{ccw}}{dt} = \left(-i(\Delta - g) + \frac{\kappa_s + \kappa_a + \kappa_0 + \kappa_{ex}}{2} \right) \cdot a_{ccw} - \left(ig - \frac{\kappa_s + \kappa_a}{2} \right) \cdot a_{cw} + \sqrt{\kappa_{ex}} s_{ccw}. \quad (5.1b)$$

Here, s_{cw}, s_{ccw} are the input powers in the CW and CCW directions, κ_0 is the intrinsic loss

ⁱThe scatterer causes transfer of power to all confined and radiative resonator modes. The coupling to modes other than counter-propagating mode is included in the intrinsic resonator loss defined by κ_0 .

rate of the WGM, κ_{ex} is the rate of coupling and $\Delta = \omega - \omega_0$ is the laser detuning with respect to the original WGM frequency. We can now define the normal modes of the resonator as $a_{\pm} = (a_{cw} \pm a_{ccw})/\sqrt{2}$, normal modes of the input as $s_{\pm} = (s_{cw} + s_{ccw})/\sqrt{2}$ and rewrite (5.1) as,

$$\frac{da_+}{dt} = \left(-i(\Delta - 2g) + \frac{2\kappa_s + 2\kappa_a + \kappa_0 + \kappa_{ex}}{2} \right) \cdot a_+ + \sqrt{\kappa_{ex}}s_+ \quad (5.2a)$$

$$\frac{da_-}{dt} = \left(-i\Delta + \frac{\kappa_0 + \kappa_{ex}}{2} \right) \cdot a_- + \sqrt{\kappa_{ex}}s_-. \quad (5.2b)$$

The steady-state solutions of (5.2) can be obtained by setting $da_+/dt = 0$ and $da_-/dt = 0$ as,

$$a_+ = \frac{-\sqrt{\kappa_{ex}}s_+}{-i(\Delta - 2g) + (2\kappa_s + 2\kappa_a + \kappa_0 + \kappa_{ex})/2} \quad (5.3a)$$

$$a_- = \frac{-\sqrt{\kappa_{ex}}s_-}{-i\Delta + (\kappa_0 + \kappa_{ex})/2}. \quad (5.3b)$$

Here, a_+ and a_- provide the amplitudes of the symmetric and anti-symmetric standing wave modes (SWMs), respectively. It is clear from (5.3) that the symmetric mode is shifted by $2g$ from the degenerate WGM and the anti-symmetric mode is unshifted. It has to be noted here that the shift of a WGM without a mode-split is g whereas the splitting between the SWMs is $2g$.

The case of multiple particles attaching to the resonator can be formulated as an extension of (5.3) by including the dependence of g, κ_s and κ_a on the angular position of the binding. The two SWMs are orthogonal modes with field amplitudes varying sinusoidally around the circumference of the resonator. Hence, the shift $\Delta\omega_+$ and $\Delta\omega_-$ of the SWMs upon binding of N nanoparticles can be given as,¹¹⁹

$$\Delta\omega_+ \equiv \omega_+ - \omega_0 = \sum_{n=1}^N 2g_n \cos^2(\phi_1 - \psi_n) \quad (5.4a)$$

$$\Delta\omega_- \equiv \omega_- - \omega_0 = \sum_{n=1}^N 2g_n \sin^2(\phi_1 - \psi_n), \quad (5.4b)$$

where g_n is the frequency shift introduced by the n th particle, ϕ_1 is the spatial phase difference of the first particle from the anti-node of one SWM and ψ_n is the phase distance of the n th particle from the first particle. Similarly, the increase in losses $\Delta\kappa = \kappa_s + \kappa_a$ can be given as,

$$\Delta\kappa_+ = \sum_{n=1}^N 2(\kappa_{sn} + \kappa_{an}) \cos^2(\phi_1 - \psi_n) \quad (5.5a)$$

$$\Delta\kappa_- = \sum_{n=1}^N 2(\kappa_{sn} + \kappa_{an}) \sin^2(\phi_1 - \psi_n), \quad (5.5b)$$

where, κ_{sn} and κ_{an} are the scattering and absorption losses introduced by the n th nanoparticle.

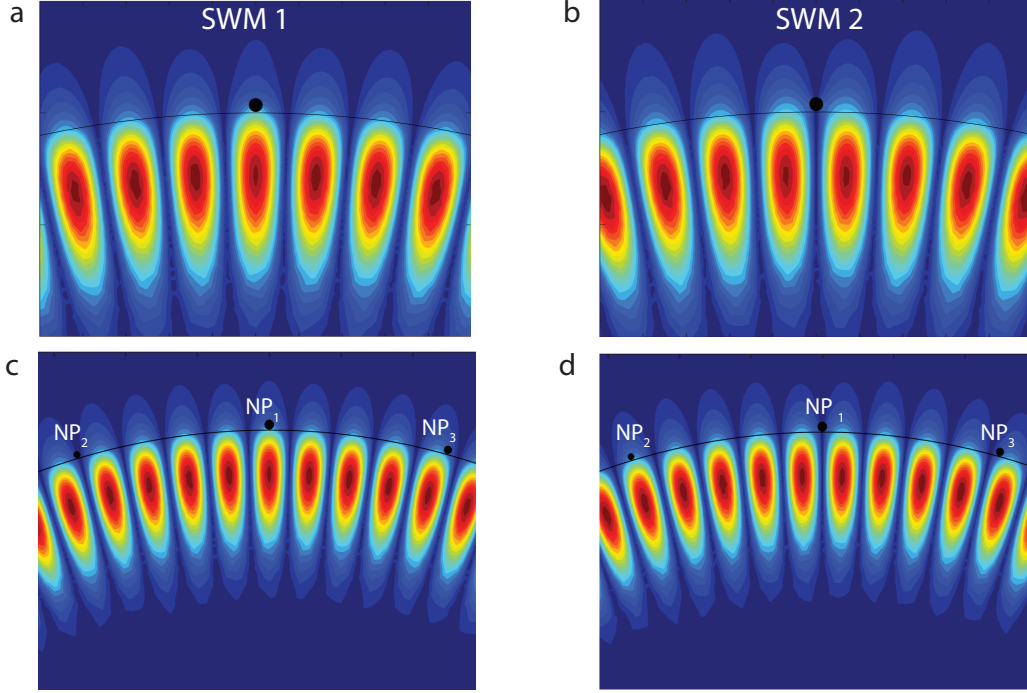


Figure 5.2. Magnetic field intensity distributions of disk resonators with $R = 5 \mu\text{m}$ with gold nanoparticles near the resonator surface. (a) Field distributions for a single nanoparticle of radius $r_p = 30 \text{ nm}$ at a distance of 5 nm from the resonator surface. (a) Field distributions for a three nanoparticles of radius $r_{p1} = 30 \text{ nm}$, $r_{p1} = 20 \text{ nm}$, $r_{p2} = 25 \text{ nm}$ at a distance of 5 nm from the resonator surface. The particles are located at azimuthal angular position $\beta_1 = 0$, $\beta_2 = 0.27$ and $\beta_3 = -0.25$.

The relative mode split between the two SWMs is given as,

$$S_N = |\Delta\omega_+ - \Delta\omega_-| = \sum_{n=1}^N 2g_n \cos(2\phi_1 - 2\psi_n). \quad (5.6)$$

The total loss induced is given as,

$$\Delta\kappa_N = \sum_{n=1}^N 2(\kappa_{sn} + \kappa_{an}). \quad (5.7)$$

Equations (5.6) and (5.7) are the key results of the chapter as discussed in the next section.

5.3 Detection of single molecules using linewidth shifts of WGMs

To study the effect of multiple scatterers on the WGM field distribution, simulations were performed using a Finite Element Modesolver (FEM) in COMSOL Multiphysics. The simulations were performed by considering small gold nanoparticles within the evanescent field of a disk shaped WGM resonator to reduce simulation complexity and computational time. However, the

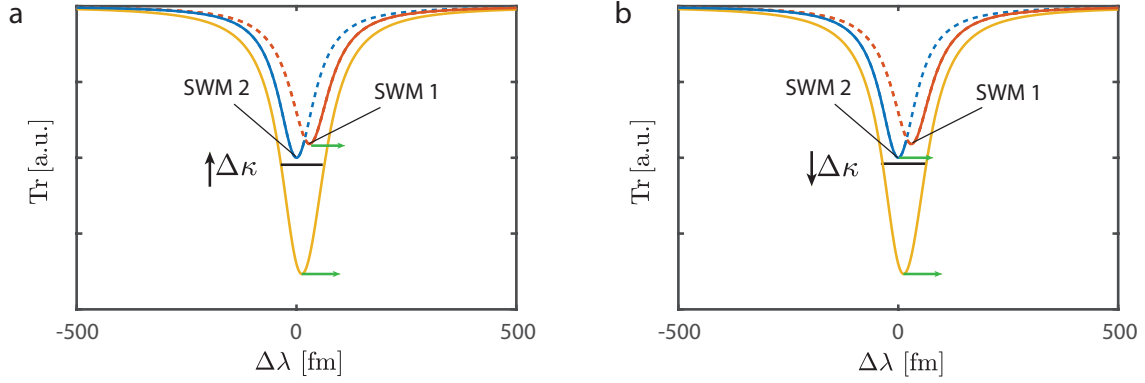


Figure 5.3. Sketch of the unresolved mode split and the corresponding direction of shift of the WGM resonance wavelength and the linewidth depending on the interaction of small sub-kDa molecules with nanoparticle I or II, respectively.

results obtained for the disk resonators are qualitatively applicable to any WGM resonator. Figure 5.2a,b plots the magnetic field intensity distributions of the symmetric and anti-symmetric WGM for the presence of a single scatterer. The simulations were performed for a disk resonator of radius $R = 5 \mu\text{m}$, with a circular gold nanoparticle of radius $r_p = 30 \text{ nm}$ located at a distance of $d = 5 \text{ nm}$ from the resonator surface and excited around $\lambda = 780 \text{ nm}$. The simulations show that the SWMs are formed such that the symmetric SWM has an anti-node at the particle position and the anti-symmetric mode has a node at the particle position. For multiple particles, the mode formation is dependent on the relative positions of the particle and can become complex.⁷⁸ Figure 5.2c,d plots the intensity distributions for the binding of three nanoparticles of radii $r_{p1} = 30 \text{ nm}$, $r_{p2} = 20 \text{ nm}$ and $r_{p3} = 25 \text{ nm}$. The nanoparticles are located at angular positions $\beta_1 = 0$, $\beta_2 = 0.27$ and $\beta_3 = -0.25$ and a distance of $d = 5 \text{ nm}$ from the WGM surface. It can be seen that np_1 (np_2) is in the node (anti-node) of one SWM and the anti-node (node) of the other, while np_3 overlaps with both SWMs partially.

If the mode splitting $S_N < \Delta\kappa_N + \kappa_0 + \kappa_{ex}$, then the mode splitting after binding of N nanoparticles is smaller than the total linewidth of the mode and hence the splitting is not resolvable. Hence, instead of two distinct lineshapes, only one mode that is the superposition of the two SWMs is observed in the transmission spectrum. This scenario is often the case in WGM-plasmonic systems where the extinction cross-section of the gold nanoparticles is high due to the excitation of LSPRs by the WGM. Figure 5.3 shows a sketch of an unresolved mode split (blue, red) and the actual observable WGM lineshape (yellow). The interaction of sub-kDa single molecules with the gold nanoparticles on the WGM surface causes a change in mode splitting S_N . As the mode splitting is unresolved, the change in splitting is translated into a change in the linewidth κ of the WGM.

For example, when a small molecule binds to the single gold nanoparticle shown in Figure 5.2a,b, SWM 1 shifts by an amount g' , while SWM 2 remains unaffected. Hence, the mode splitting S_N changes by an amount of $2g'$ according to (5.6). A corresponding shift of g' is observed in the WGM frequency, while the FWHM (as a proxy for the splitting) shifts by $2g'$. In the case of multiple nanoparticles attached to the WGM surface, the shifting of the individual SWMs is dependent on the position of the nanoparticles on the surface. For the system with three

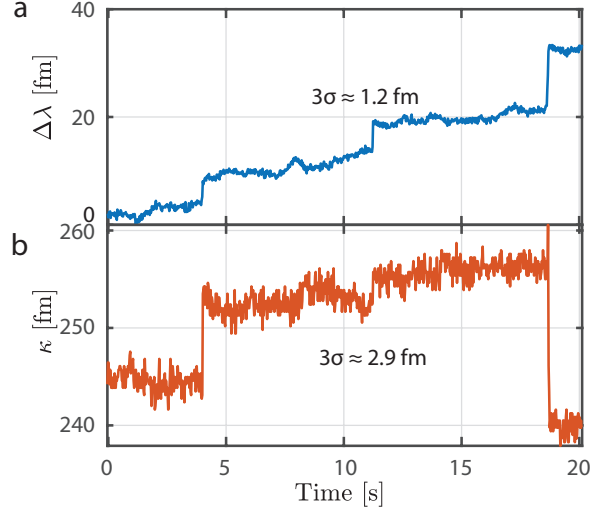


Figure 5.4. Experimentally measured shift of the WGM lineshape upon binding of Dithiobis(C2-NTA) molecules to the plasmonic gold nanorods attached to the WGM. (a) Shift of the WGM resonance wavelength $\Delta\lambda$. (b) The shift of the WGM resonance linewidth κ .

nanoparticles in Figure 5.2c,d, a molecule binding to NP_1 introduces a shift to the SWM 1 as illustrated in Figure 5.3a. Hence, an increase in splitting by a factor of $|2g'|$ is introduced leading to an apparent increase in the FWHM. Whereas, when the molecule interacts with NP_2 , the shorter wavelength SWM 2 shifts as it is maximally overlapped with the nanoparticle as shown in figure 5.3b. This results in a decrease of splitting S_N by the factor $|2g'|$ leading to an apparent negative shift in the FWHM. Finally, when the molecule interacts with NP_3 , both SWMs are partially shifted and hence the change in splitting is given by (5.6) as $\Delta S_N = 2g' \cos(\phi_1 - \psi_n)$. Figure 5.4 plots an example of the WGM resonance wavelength shift ($\Delta\lambda$) and the linewidth (κ) upon binding of single molecules of Dithiobis(C2-NTA), $C_{26}H_{44}Cl_2N_4O_{14}S_2$ (M.W. 771.8, Dojindo EU GmbH). The shift in $\Delta\lambda \equiv -g'$ is always positive whereas the linewidth shift changes sign depending on the nanoparticle position as predicted by (5.6).

In general, the linewidth shifts due to single molecules can vary from $2g'$ to $-2g'$ depending on the position of the binding around the circumference of the resonator. Fig. 5.5a plots the linewidth change $|\Delta\kappa|$ vs the resonance shift ($\Delta\lambda$) for the binding of multiple Dithiobis(C2-NTA) molecules across three spherical WGM resonators. As predicted by (5.6), the magnitude of the linewidth shifts lies between $0 - 2\Delta\lambda$. Hence, a signal enhancement of 2 can be obtained by linewidth signals. However, it has to be noted here that the WGM linewidth noise scales independently of the noise in the WGM resonance position. The linewidth noise is mainly dominated by the loaded quality factor $Q_L = (\kappa_0 + \kappa_a + \kappa_s)/\omega$ for short integration times, while the WGM frequency noise is dominated by the laser frequency/phase noise. Typically, for medium quality resonators with $Q_L \approx 10^6 - 10^7$, noise in linewidth is approximately twice that of the WGM resonance wavelength. The short term noise of the WGM is quantified as the standard deviation of signal 3σ estimated over 200 ms. The background noise for the experiments plotted in figure 5.4 is 1.2 fm for $\Delta\lambda$ and 2.9 fm for $\Delta\kappa$. Since the noise in the linewidth is associated with Q_L , a higher Q_L in the range of 10^8 will provide a better signal-to-noise ratio (SNR) for measurements using the linewidth. Nonetheless, at longer integration times, the noise in the

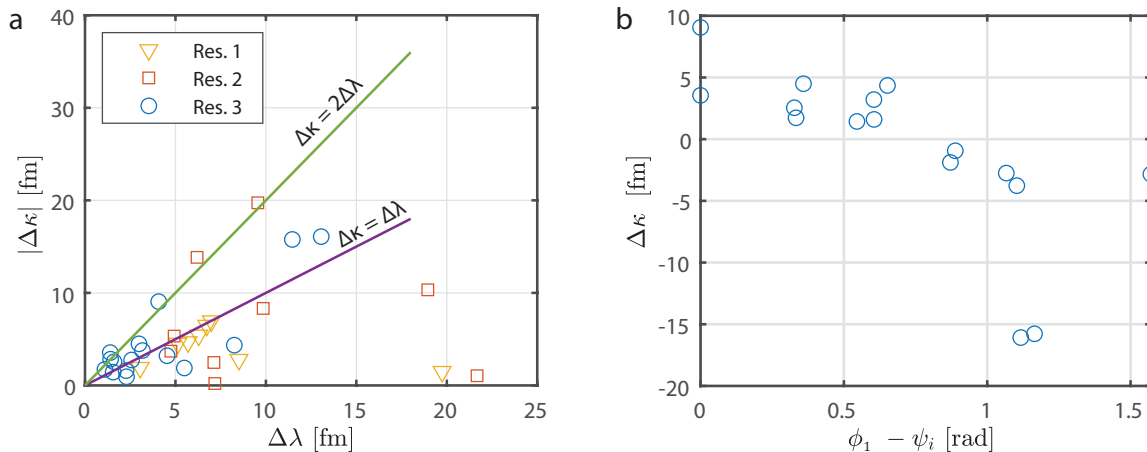


Figure 5.5. (a) WGM linewidth shift ($|\Delta\kappa|$) vs the resonance wavelength shift $\Delta\lambda$ for the binding of Dithiobis(C2-NTA) molecules measured using three different plasmonically enhanced spherical WGM resonators. (b) WGM linewidth shifts $\Delta\kappa$ as a function of the phase difference between the first nanoparticle and nanoparticle n where the molecule binds.

WGM resonance position quickly exceeds the WGM linewidth noise due to the long term noise sources such as laser/ WGM frequency drifts due to changes in temperature, pressure, and analyte concentrations.

Additionally, information on the position of the binding molecules along the circumference of the resonator can be estimated from 5.6 as plotted in Fig. 5.4b. The clustering of the events around specific values of $\phi_1 - \psi_n$ indicates the relative azimuthal position of the gold nanoparticles attached to the WGM resonator. The differences in amplitude of $\Delta\kappa$ within each cluster arise from the different enhancements experienced by the molecules attaching to different locations on the same nanoparticle. Further, the polar position of the nanoparticles can be estimated using multiple WGMs of different m orders.¹²⁰

5.4 Conclusions

In this chapter, we have discussed the origin of linewidth shifts from the binding of single molecules to our sensor. The shift in linewidth arises from the unresolved mode-splitting of the SWMs. The SWMs are formed due to the interference of counter-propagating modes of a WGM in the presence of small scatterers on the WGM cavity surface. Detection of even extremely small sub-kDa single molecules can be achieved with this scheme. The linewidth shift can take values between $-2\Delta\lambda$ to $2\Delta\lambda$ and hence can be more sensitive to single-molecule events compared to the resonance shift $\Delta\lambda$. However, the noise for WGM linewidth is typically larger than for the WGM resonance shift. Hence, the SNR is often lower for the linewidth shifts. A high SNR can be obtained by utilizing high Q resonators (Q $10^7 - 10^8$). Even without significant improvements to the noise figure the WGM linewidth is a more robust channel for detecting single molecules as it is robust against long-term noise sources such as laser or WGM frequency drifts due to changes in temperature, pressure, and local analyte concentrations. The

WGM linewidth can hence provide long-term signals without the need for complicated feedback and stabilization techniques.

Recently, Vincent *et al.*¹²¹ presented linewidth signals $\Delta\kappa > 2\Delta\lambda$. These signals are not explained by the shifting of unresolved split-modes. Alternative explanations are required to describe the observations presented therein. In our experiments, due to the random loading of the gold nanoparticles, most linewidth shifts were not maximized. Precise control over the nanoparticle immobilization can maximize the shifts in the linewidth. Combining $\Delta\kappa$ and $\Delta\lambda$ allows us to extract the information on the relative azimuthal position of the gold nanoparticles in our sensor. The polar position of the gold nanoparticles can be obtained using a method reported by Keng *et al.*¹²⁰ Locating the gold nanoparticles around the WGM cavity surface can allow us to perform multiplexed detection with different receptor molecules on each nanorod attached to the WGM cavity surface. Finally, identifying the position of the nanoparticles can aid in discerning the contributions of molecular weight, orientation, and chirality to the single-molecule signals.

Chapter 6

Fast detection of nanoparticles and single molecules

6.1 Introduction

We have so far seen the exceptional sensitivity of a WGM-plasmonic hybrid sensor to monitor the interactions of small molecules. However, the processes studied were slow in the order of hundreds of milliseconds (DNA hybridization) or discrete such as direct binding of small molecules to the gold nanoparticle. Hence, the simple method of laser scanning could provide the necessary information for the SM studies. Nonetheless, many biological processes of interest such as protein folding and enzyme catalysis have functional components that occur in the microsecond and lower timescales. Hence, fast extraction of the WGM spectra are required. Additionally, fast monitoring of the WGM spectra will enable monitoring diffusion interaction of molecules with the gold nanoparticle which opens up the possibility of detecting a broad range of molecules other than the ones containing thiol or amine groups.

The time resolution of a cavity-based sensor is ultimately limited by the cavity lifetime. For the WGMs used in this thesis with $Q \approx 10^7$, the cavity lifetime is $\tau \approx 100$ ns. Hence, it is theoretically possible to detect the SM signals with a sub-microsecond time resolution. Current methods for SM detection using WGM-plasmonic hybrid system uses a laser scanning approach described in previous chapters which are inherently limited by the resonance frequency of the piezo scanner to typically 1 kHz. However, at higher scan rates additional noise is introduced by the piezo scanner which is detrimental in SM experiments. There do not exist many techniques for extracting the entire cavity resonance position at MHz-GHz rates in the literature.

Recently, Rosenblum *et. al.*¹²² reported a technique that uses far detuned pulses with short rise-time to perform a heterodyne measurement to acquire the complete cavity spectrum in the nanosecond time scale termed cavity ring-up spectroscopy (CRUS). Figure 6.1 shows a schematic representation of the technique. An electro-optic modulator is used to excite the WGM microtoroid cavity with square pulses at a high repetition rate. The laser wavelength is

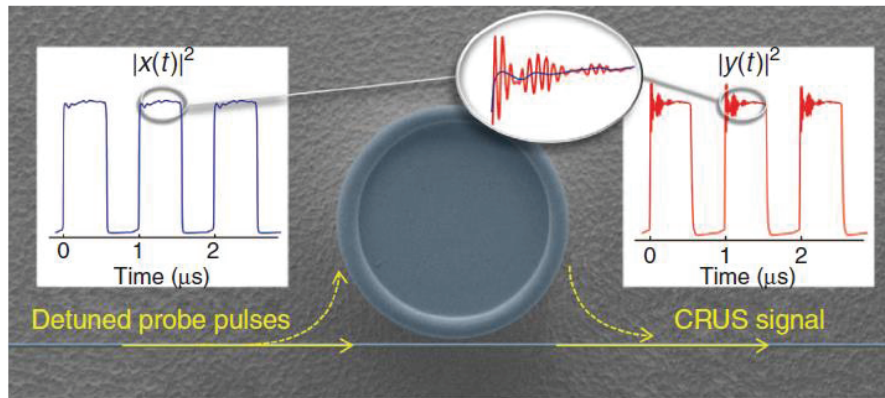


Figure 6.1. Schematic representation of cavity ring-up spectroscopy (CRUS). Adapted from Rosenblum *et. al.*¹²² under the CC-BY-4.0 licence.

maintained far detuned from the cavity resonance. The short rise time t_r of the laser pulses corresponds to a large bandwidth of B given by $B \sim 1/t_r$. If the detuning of the laser from the cavity resonance δ is less than B , then light couples into the cavity and interferes with the specularly reflected light-producing interferograms as shown in Figure 6.1. A Fourier transform of the interferogram then enables the extraction of the complete cavity spectrum. The repetition rate of the pulses and the cavity lifetime determine the time resolution of the system which can be as small as nanoseconds. For biosensing at the SM level, the major drawbacks of this technique are the computationally costly post-processing to extract the cavity spectrum, the additional effort required to maintain the cavity-laser detuning over a long measurement duration and the need for very high coupling efficiency requiring the use of fiber tapers for coupling.

In this thesis, we utilize an alternate technique based on the frequency lock-in of the laser to the cavity resonance. The idea behind the lock-in measurement is to follow resonance using a feedback controller without running off due to laser/cavity drift. Fluctuations in the cavity frequency can then be read out continuously by direct measurement of the feedback signal. Using high bandwidth and low-noise electronics, fast feedback can be obtained to eliminate low-frequency noise which is the dominant source of noise in the system. Using this method, shot-noise limited performance can be thereby achieved. Additional modulation once the laser is locked to the cavity can enable sensitive extraction of the cavity linewidth.¹²³

6.2 Frequency lock-in using the Pound-Drever-Hall (PDH) method

For continuous monitoring of the WGM frequency, the laser has to be locked to the WGM resonance. However, locking to the cavity resonance is not straightforward as the resonance spectrum is symmetric on both sides of the resonance as shown in Figure 6.2a. Hence, the direction of change in the resonance of the cavity or laser cannot be directly measured using the intensity of the spectrum. Also, using the intensity of the spectrum is prone to intensity noise

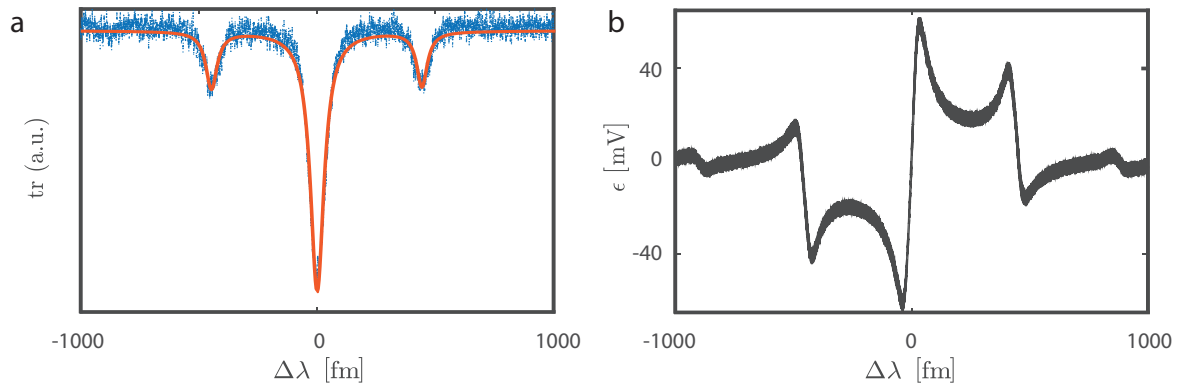


Figure 6.2. a) Measured cavity transmission spectrum with side-bands modulated at $w_0 \pm \Omega$. b) Error signal (derivative of cavity spectrum) obtained after analog demodulation and lowpass filtering.

sources. Alternatively, the derivative of the cavity resonance (Figure 6.2b) is antisymmetric about the cavity resonance. The zero-crossing of the derivative signal provides the intensity minimum of the cavity resonance spectrum. Hence, positive (negative) changes in the derivative signal denote a red (blue) shift depending on the slope of the derivative. This derivative signal termed error signal can hence be used as feedback to lock the laser to the cavity. This method of using the derivative of cavity spectrum for locking is known as a Pound-Drever-Hall (PDH) lock after its originators⁸⁵ and is a popular method of laser locking in high precision fields such as atomic optics and gravitational wave detection.

The PDH lock is achieved by modulating the phase of the cavity's incident field at a frequency Ω using a fast electro-optic modulator. Thus, the incident field takes the form $E_{inc} = E_0 \exp(i\omega_0 t + i\beta \sin \Omega t)$, where $E_0 \exp(i\omega_0 t)$ is the field prior to the phase modulation and β is the modulation depth. As a result side-bands are produced at $\omega \pm \Omega$, $\omega \pm 2\Omega$ and so on as shown in Figure 6.2a. If the modulation frequency is much higher than the cavity linewidth, then the sidebands do not accumulate any phase information of the cavity. However, the beat note between the carrier and sidebands contains the relative phase information between the incident and cavity fields.

The reflected light from the cavity is measured using a high bandwidth photodetector which contains the beat note between the carrier and the sidebands. An analog mixer is fed the detector output and the modulation frequency as input. The analog mixer essentially forms the product of the two sinusoidal inputs and provides a dc signal when the frequencies of the two inputs are the same as in our case. This dc signal is then isolated using a lowpass filter at the output of the analog mixer to obtain the error signal ϵ as shown in Figure 6.2b. In practice, any delays in the phase of the two signals has to be compensated using a phase shifter. This error signal is proportional to the detuning of the laser frequency from the cavity resonance and is given by,¹²⁴

$$\epsilon \approx -8\sqrt{P_c P_s} \frac{\delta\nu}{\kappa} \quad (6.1)$$

where P_c is the power in the carrier, P_s is power in the side bands and ν is the laser frequency and κ is the cavity linewidth. As long as the cavity linewidth is constant, a simple calibration can be used to convert the measured feedback voltages to the frequency shifts using (6.1). The

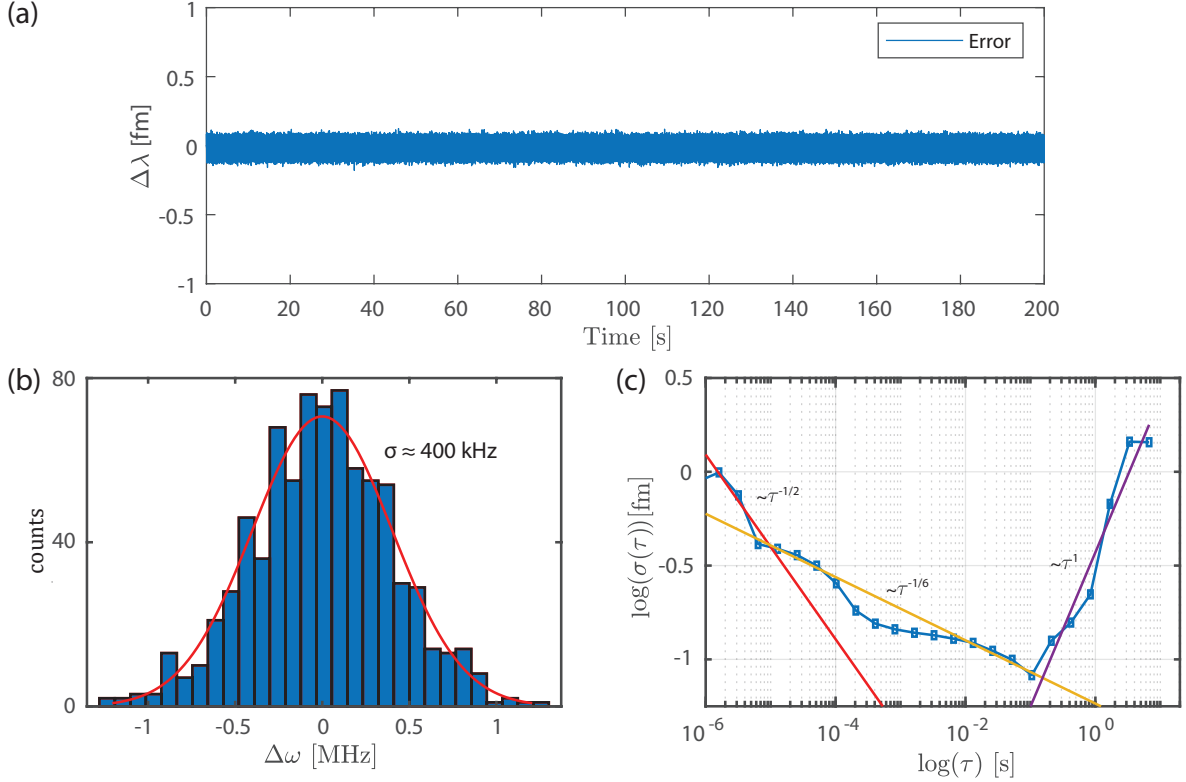


Figure 6.3. (a) WGM resonance position measured in ultra-pure water tracked using the error signal of a PDH lock. (b) Histogram of the WGM frequency measured using the PDH error signal. (c) Allan deviation plot of the WGM frequency obtained by the PDH error signal. The different slopes identify various noise sources in the system.

easy availability of high-speed photodetectors, function generators, modulators, and low-noise amplifiers enables the creation of PDH lock-in setups with extremely high (GHz) bandwidths. The error signal can be split into multiple channels to provide signals at different bandwidths (See Section 3.5 for implementation details). Swaim *et al.*¹²⁵ used a similar system to detect the interaction of gold nanoparticles with a micro toroid cavity.

Figure 6.3a plots the WGM resonance frequency measured using the error signal of the PDH lock with a WGM resonator of diameter $82\ \mu\text{m}$ in ultra-pure water. The signal was recorded at a sampling rate of 2.5 MHz. The plot has been downsampled to 25 kHz to enable long-time plotting. No spike-like events are observed in the time trace. Figure 6.3b plots the histogram of the WGM frequency measured in water using the PDH error signal. The standard deviation of the WGM frequency obtained with an integration time of $5\ \mu\text{s}$ is $\sigma \approx 400$ kHz. This value is slightly above the 300 kHz laser linewidth reported by the manufacturer for this laser with the same integration time. Hence, the PDH lock-in system is capable of tracking the WGM frequency ultimately limited by the laser linewidth. Figure 6.3c plots the Allan deviation of the measured WGM frequency over different integration times. The different slopes in the plot indicate different noise sources. At low integration times, the slope of $\tau^{-1/2}$ indicates domination of the laser frequency noise, at moderate integration times an additional phase noise component with slope $\tau^{-1/3}$ is added on top of the frequency noise, and at high integration times the laser drift dominates with a slope of τ^1 . The Allan deviation plots also show that we are far from any

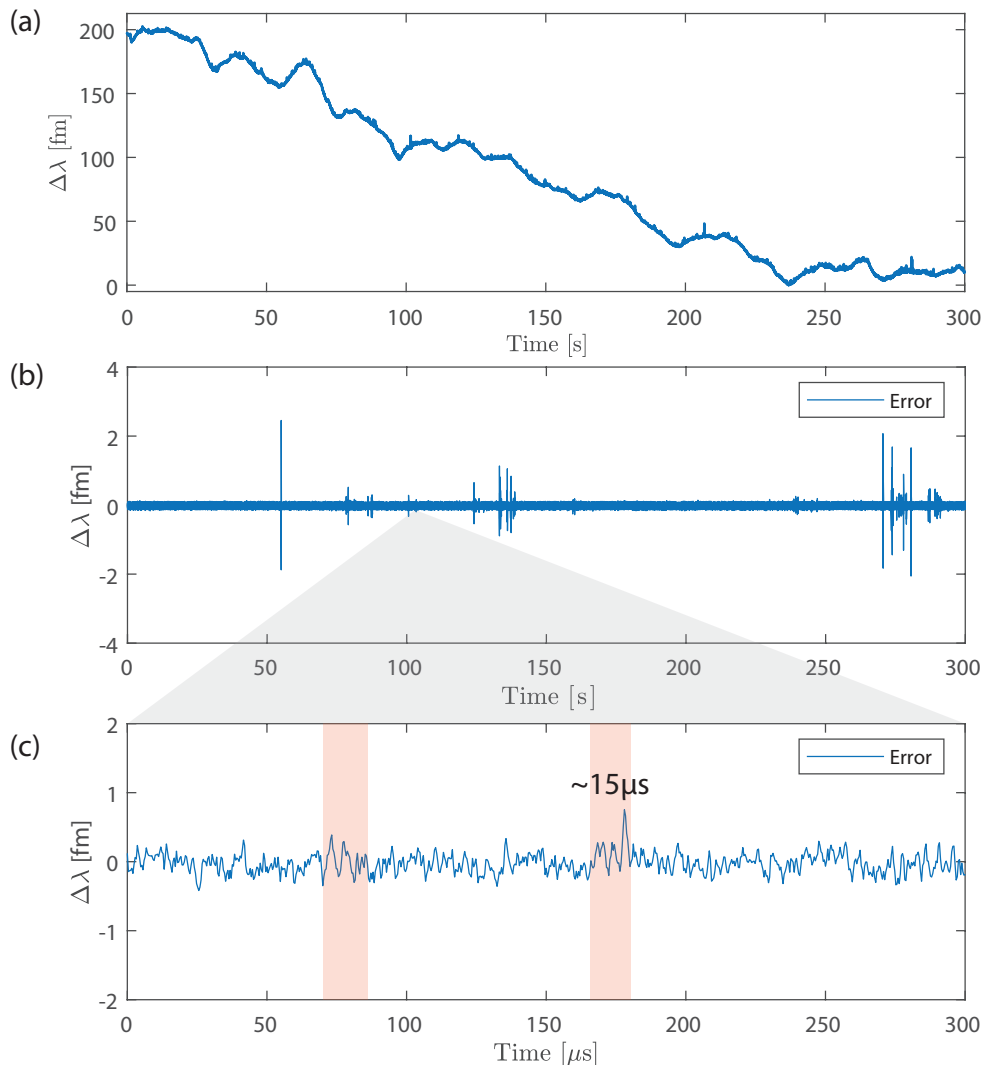


Figure 6.4. Interaction of gold nanorods with the WGM.(a) A long time scale measurement of interaction of NPs with the WGM cavity surface using the piezo scanning method. (b) Long-term interaction signal of the diffusion interaction of the nanorods measured using the PDH error signal. The PDH error signal has been downsampled to 25 KHz for plotting. (c) A zoom-in of (a) around 100 s showing signals in the microsecond timescale.

fundamental noise limitations and improving the electronics of the lock and the laser linewidth can lead to lower noise even at smaller integration times.

6.3 Measurement of the diffusion of gold nanoparticles in water

Next, gold nanorods (A12-40-CTAB-750, Nanopartz Inc., USA) are added to the sample chamber. Figure 6.4 plots the WGM resonance shift signals upon the diffusion interaction of the gold nanorods with the WGM cavity surface. Figure 6.4a plots the signals measured using the traditional piezo scanning approach. The signals are obtained after processing of the WGM

spectra. Slow background drifts due to temperature and pressure fluctuations have to be corrected during post-processing. Figure 6.4b plots the signals measured using the PDH error signal obtained at a sampling rate of 2.5 MHz. The feedback controller enables the correction of the background signals and hence enables real-time measurement of the signals. The signals in the plot have been downsampled to 25 KHz. Figure 6.4c plots a zoom-in of the interaction signals around 100 s without any downsampling. Interaction duration of the nanorods as fast as 15 μ s can be measured using the PDH error signal.

6.4 Conclusions

In conclusion, the ultimate limit of the sensor time resolution is set by the cavity lifetime. For the WGMs used in this work, the cavity lifetime is in the range of 10 – 100 ns. However, extracting the information of the resonance position at these timescales is challenging. A fast PDH lock-in method was employed here to achieve a microsecond timescale. The PDH lock enabled the measurement of the WGM resonance position with a sensitivity limited by the laser noise over various time scales. Although faster extraction of the WGM resonance down to *ns* is possible using the PDH lock, an Allan deviation plot showed that the instantaneous noise at these timescales is high. At these timescales, the expected signal amplitude is also smaller due to the short integration time of the signal. Hence, practical detection at GHz frequencies could not be achieved yet. Nonetheless, the lock-in method could be utilized to detect signals from the free diffusion of single gold nanoparticles across the WGM resonator down to the μ s timescale.

Chapter 7

Studying the thermodynamics of single enzymes using WGM-plasmonic sensors

7.1 Introduction

Enzymes are a class of biomolecules that are interesting for biological, sensing, and industrial applications. Enzymes derive their functionality from a diverse range of motion spanning a wide time (fs-hours) and amplitude range.¹²⁶ Although the dynamics of enzymes are accessible via various methods, assigning the dynamics to catalytic activity is challenging. The temperature dependence of enzyme turnover activity is often used to study the fundamental thermodynamics and processes involved in catalysis. The Eyring-Polanyi equation is typically used for describing the temperature dependence of the catalytic rates,

$$k = \frac{\kappa k_B T}{h} \exp\left(-\frac{\Delta G^\ddagger}{RT}\right) \quad (7.1)$$

where, ΔG^\ddagger is the Gibb's free energy, k_B is the Boltzman constant, h is the Planck's constant, T is the temperature, R is the universal gas constant, and κ is the transmission coefficient. The transmission coefficient κ describes the probability that the transition state complex will dissociate into products rather than reverting to the reactants. Although it can take values between 0 and 1, κ is assumed to be 1 for most reactions.¹²⁷ From (7.1), the activation enthalpy and entropy of the process is obtained (from $\Delta G^\ddagger = \Delta H^\ddagger + T\Delta S^\ddagger$). Recently, a large body of data has emerged where enzymes do not conform to this model. An alternate model termed macromolecular rate theory (MMRT) was proposed recently by Hobbs *et al.*⁵⁷ to interpret these data. This model postulates a change in heat capacity, ΔC_P^\ddagger , (associated with the change in

The content of this chapter appeared in Subramanian, S., Jones, H.B.L., Frustaci, S., Winter, S., van der Kamp, M.W., Arcus, V.L., Pudney, C.R., and Vollmer, F., "Sensing Enzyme Activation Heat Capacity at the Single-Molecule Level Using Gold-Nanorod-Based Optical Whispering Gallery Modes," ACS Applied Nano Materials 4(5), 4576–4583 (2021).

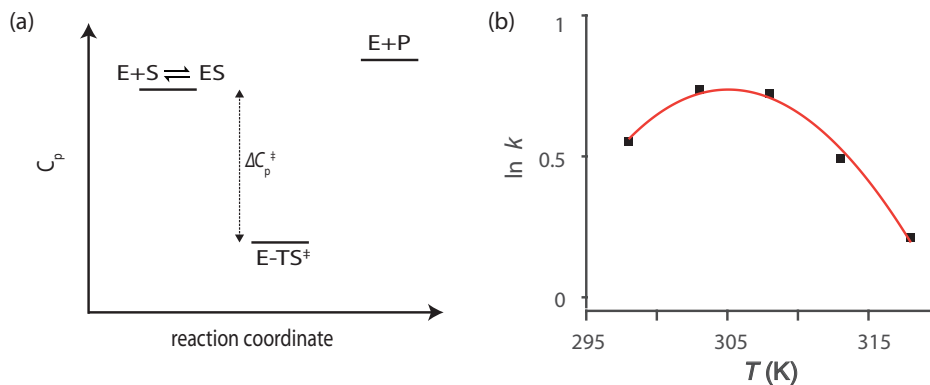


Figure 7.1. (a) Heat capacity of an enzyme-catalyzed reaction along the reaction coordinate as predicted by MMRT. (b) Negative curvature of the catalytic rate with temperature arising a consequence of a negative ΔC_p^\ddagger . The measured rates (black squares) obtained from temperature dependent measurements of a mutant of the enzyme MalL (see section 7.5) and the corresponding fit to (7.2) is shown by red line.

conformational fluctuations along the reaction coordinate) between the enzyme-substrate (E-S) complex and the enzyme-transition state (E-TS) complex. Under this model, the Eyring-Polanyi equation is extended as,

$$\ln k = \ln \frac{k_B T}{h} - \frac{\Delta H_{T_0}^\ddagger + \Delta C_p^\ddagger (T - T_0)}{RT} + \frac{\Delta S_{T_0}^\ddagger + \Delta C_p^\ddagger (\ln T - \ln T_0)}{R} \quad (7.2)$$

where $\Delta H_{T_0}^\ddagger$ is the activation enthalpy, $\Delta S_{T_0}^\ddagger$ is the entropy and T_0 is an arbitrary reference temperature. Here, κ is assumed to be 1. It has been observed that the value of ΔC_p^\ddagger is in general negative.^{57,128} That is, the heat capacity of the enzyme-substrate (ES) complex is higher than the enzyme-transition state (E-Ts) complex as illustrated in Figure 7.1a. A consequence of this negative ΔC_p^\ddagger is the observation of a negative curvature in the enzymatic rates $\ln k$ as predicted by (7.2) and is illustrated in Figure 7.1b.

Previously, Jones *et al.*¹²⁹ showed that maltose-inducible α -glucosidase (MalL) deviates from Eyring kinetics. The temperature dependence of the rate of hydrolysis of the substrate 4-Nitrophenyl β -D-glucopyranoside (pNPG) into a β -D-glucose and p-Nitrophenol measured using colorimetric assays showed a negative curvature resulting in a significant negative ΔC_p^\ddagger . Further, van der Kamp *et al.*¹³⁰ performed extensive molecular dynamics (MD) simulations of MalL for the enzyme-substrate complex and a pseudo enzyme-transition state complex (5 μ s for each). They identified that the source of the negative ΔC_p^\ddagger arises from a difference in conformational fluctuations between the ground and transitions state as hypothesized by the MMRT model. These changes in fluctuations are distributed across the enzyme domains and thus, account for the large values of the activation heat capacity ($-5.9 \text{ kJ.mol}^{-1}.\text{K}^{-1}$)¹²⁹ and the pronounced deviations (curvature) from Eyring kinetics.

In this chapter, the WGM-plasmonic hybrid sensor is applied to study the thermodynamics of a functionally similar mutant of MalL at the single-molecule level. Using the microsecond time resolution offered by the PDH technique, the fast conformational dynamics are monitored. The chapter is organized as follows. Firstly, we monitor the electrostatic interaction of single en-

zymes with the gold nanorod surface. Then, specific immobilization of the enzyme via a surface cysteine group is monitored in real-time. A mutant of MalL is produced to achieve specific immobilization of the enzyme to the gold surface. Molecular dynamics (MD) simulations are used in the next step to study the effect of the gold surface on the enzyme dynamics. The catalysis of the substrate pNPG is then monitored using the PDH lock-in technique. Specific signal patterns associated with single enzyme-substrate interactions are identified. The signal patterns likely correspond to the steps in the catalytic process. Multiple rates are extracted from fits to the distribution of the event height, duration, and time between consecutive events. Our experiments show that the measured rates are reduced compared to the free enzyme in solution. The reduction in enzyme activity is likely due to the interaction of the enzyme with the gold surface as predicted by the MD simulations. Finally, we study the temperature dependence of the enzyme-substrate interaction and catalytic rates using our sensor. The temperature-dependent turnover rate of the enzyme is estimated from the SM signals obtained. The enzymatic rates dependent on temperature are shown to have a negative curvature even at the SM level providing strong evidence in support of the MMRT model.

7.2 Specific immobilization of the enzyme

Specific immobilization of the enzymes with a specific orientation is necessary for controlling the distance of the active site from the gold nanoparticle surface to enhance sensitivity and restrict any diffusive motion during catalysis. In this way, we obtain repeatable signal patterns associated with catalysis. Information about the conformational dynamics of the enzyme may be extracted from these signal patterns. We achieve specific immobilization of the enzyme by modifying the enzyme to contain a free thiol (-SH) group to interact with the gold nanorod. The binding of thiolates to $\langle 111 \rangle$ and $\langle 100 \rangle$ atoms of a gold surface are well known and commonly used for forming self-assembled monolayers on gold surfaces and nanoparticles.¹³¹ An alternative method of immobilization is to use linker molecules to attach the enzymes.¹³² However, this methodology introduces a greater separation of the enzyme from the gold nanorod surface which can result in loss of sensitivity.

Hence, we chose to introduce a mutation to the enzyme such that the active site of the enzyme is within the near-field enhancement provided by the gold nanoparticle. A mutation from serine (S) to cysteine (C) at residue 135 on the wildtype enzyme MalL produces a solvent-exposed thiol group as shown in Figure 7.2a. The mutated enzyme is referred to as S135C MalL henceforth. Site-directed mutagenesis of MalL to generate S135C MalL was carried out by Genscript (Piscataway, NJ, USA). The expression and purification of full-length *Bacillus subtilis* 168 MalL were carried out as outlined previously by Hobbs *et al.*⁵⁷ After purification S135C MalL was buffer exchanged into 20 mM HEPES 20 mM TCEP pH 7.0 using spin concentration (10 kDa cut-off). Here, the protein was diluted at a 1:10 ratio, and concentrated 10 fold, 6 times.ⁱ

ⁱMutation and expression of the enzyme were performed by Hannah Jones in the lab of Dr. Christopher Pudney, University of Bath.

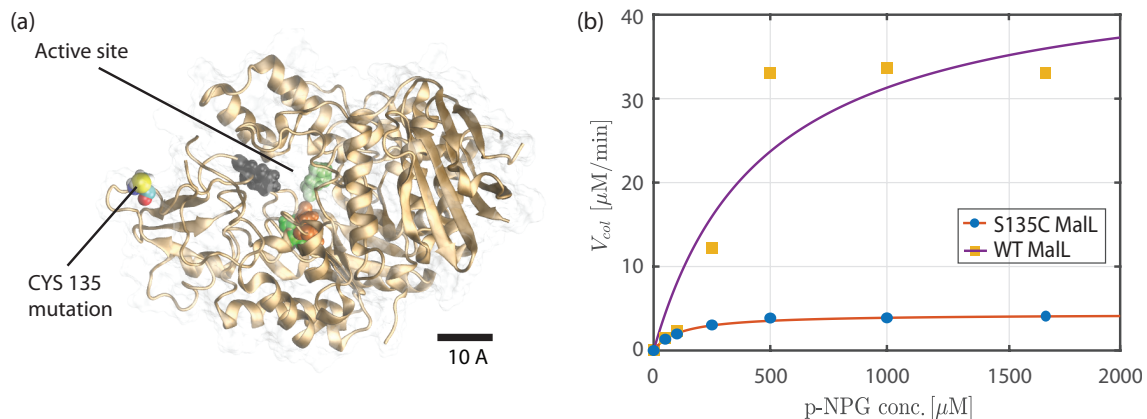


Figure 7.2. (a) Representation of the mutated enzyme rendered using Visual Molecular Dynamics (VMD) software.^{133,134} (b) Steady-state kinetics of the WT MalL (squares) and S135C MalL (circles) measured using a colorimetric assay and the corresponding fits to the Michaelis-Menten kinetics equation.

Colorimetric measurements showed that the mutation introduced to the enzyme does affect the catalytic rate of the enzyme. The colorimetric measurements were performed using a UV-VIS spectrophotometer by measuring the rate of absorption of p-Nitrophenol at 410 nm after turnover of the substrate pNPG. An enzyme concentration of 100 nM was used and the pNPG concentration was increased from 100 μM to 2 mM in 6 steps to obtain the kinetics of the enzyme as shown in Figure 7.2b. The measured reaction velocity V_{col} for WT MalL (squares, orange) and S135C MalL (circles, blue) are plotted and the corresponding fits to the Michaelis-Menten (MM) equation¹³⁵ are also plotted. The MM equation is given as,

$$V = k_{cat}[E][S]/(K_M + [S]) \quad (7.3)$$

where, V is the reaction velocity measured, k_{cat} is the enzyme catalytic rate, $[E]$ the enzyme concentration, $[S]$ the substrate concentration, and K_M the Michaelis constant. The Michaelis constants K_M estimated from the fits are 107 M and 113 M for the WT and S135C MalL, respectively. The values of enzyme catalytic rates k_{cat} are 1034 min^{-1} and 181 min^{-1} for the WT MalL and the S135C MalL at 35 C, respectively. The activity of the mutant S135C MalL is hence approximately 6 fold lower than the WT MalL enzyme at 35 C. Here, we chose to trade-off some catalytic rate to ensure that the active site of the enzyme is closer to the nanorod surface.

For the SM experiments, the plasmonically enhanced WGM sensor was assembled as described in previous chapters. After sensor assembly, single enzymes were introduced into the sample chamber in 20 mM HEPES buffer, pH \sim 7.2. Figure 7.3a shows the WGM signals obtained by the PDH error signal upon addition of 50 nM of S135C MalL to the sample chamber. The spike-like transient interactions obtained indicate the interaction of the enzyme with the gold nanorod surface. Inset of Figure 7.3b shows a plot of the probability distribution function $p(\tau)$ of the interaction duration (τ). A mean interaction duration $\tau_m \approx$ 20 ms is obtained from a log-normal distribution fit according to (4.1) using a maximum likelihood estimate. The value of τ_m is similar to the 20 ms scanning time typically used in the laser scanning approach previously described. Hence, the PDH lock-in technique is required to resolve these fast single-molecule

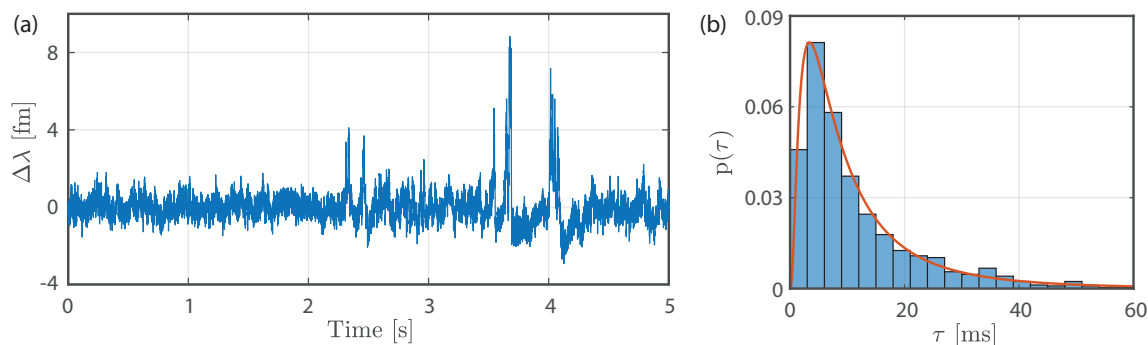


Figure 7.3. (a) Sensor signals due to transient interaction of the enzyme with the gold the gold nanorod in the absence of the reducing agent. (b) Probability distribution histogram of the duration of the interaction events and the corresponding log-normal fit according to (4.1). A mean interaction duration of ~ 20 ms is estimated indicating electrostatic interactions of the enzyme with the gold nanorod.

events. Previously, Kim *et al.* showed that the interaction of a DNA-polymerase with gold nanorods could not be detected with a similar sensor, however using at a lower acquisition rate of 50 Hz. Using Monte-Carlo simulations, they estimated that DNA polymerase molecules exited the evanescent field of the gold nanorods within a few microseconds assuming the molecules are elastically reflected off the nanorod surface (see supplementary section S9, Kim *et al.*⁵²). Hence, the high value of $\tau_m \approx 20$ ms obtained here shows the presence of electrostatic interactions between the enzyme S135C MalL and the gold nanorod surface and the assumption of elastic interaction between the enzyme and the gold surface is no longer valid.

Upon the addition of S135C MalL to the sample chamber, only transient interactions were obtained indicating unsuccessful immobilization of the enzyme on the gold nanorod surface. The inability of the enzyme to bind is likely due to the unavailability of free solvent-exposed thiols to adsorb to the gold nanoparticle surface due to dimerization of the enzymes via a disulfide bond.¹³⁶ To remove any disulfide formation, 20 mM of the reducing agent Tris(2-carboxyethyl)-phosphine hydrochloride (TCEP) was added to the buffer. Figure 7.4a shows the step changes in WGM resonance obtained upon addition of TCEP. These steps indicate a permanent binding of S135C MalL to the nanorod surface. This shows that the binding to the gold surface occurs via the mutated CYS group as S135C MalL contains only one solvent-exposed CYS group at residue 135. Inset of Figure 7.4a shows the step heights measured over 20 mins. A total of 5 binding steps above the noise were observed. Hence, we consider a total of 5 enzymes to contribute to signals of enzyme-substrate interactions in the next set of experiments. Enzymes that bind to the nanorod but do not produce a significant binding step are ignored as they also do not contribute to further signals. Figure 7.4b shows an illustration of the enzyme S135C MalL immobilized on the tip of a gold nanorod rendered using Visual Molecular Dynamics (VMD).^{133,134} The exponential decay of the normalized electric field from the surface of the nanorod is plotted for reference. The choice of the mutation site ensures that the active site of the enzyme is situated 2 – 3 nm away from the surface of the gold nanorod where the enhancement is still approximately 20-fold.

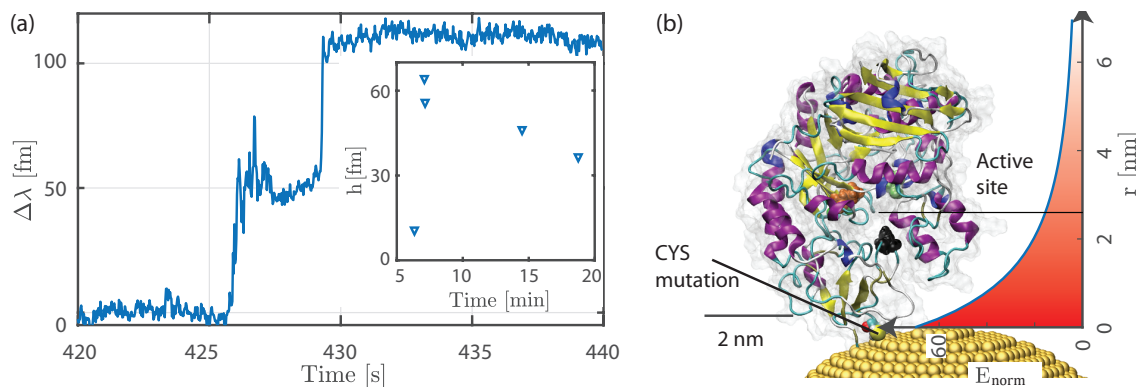


Figure 7.4. (a) Binding of the enzyme to the tips of gold nanorods in the presence of the reducing agent. Inset shows a total of five binding events observed during a 20 min measurement interval. (b) Representation of the enzyme (S135C MaL) immobilized on the tip of a gold nanorod via an Au-S link. The active site of the enzyme is situated 2 – 3 nm away from tip of the nanorod. Enzyme representation rendered using VMD.^{133,134}

7.3 Molecular dynamics simulations of the enzyme-gold interactions

We performed Molecular Dynamics (MD) simulations to study the impact of interactions of the enzyme with the gold nanorod surface on the enzyme dynamics. MD simulations were performed in the GROMACS software package¹³⁷ for both the free enzyme and enzyme near an Au $\langle 111 \rangle$ surface. A 40 ns simulation was performed for both cases and the analysis of the results obtained was performed using GROMACS and VMD.^{133,134} The free enzyme simulations were performed using the OPLS¹³⁸ force-field and the enzyme-surface simulations are performed using the GolP-OPLS¹³⁹ force-field. The GolP-OPLS force-field includes parameters for amino acid-gold, water-gold, and ion-gold interactions.

For the free enzyme simulations, a cubic simulation box was used with dimensions 1 nm larger than the enzyme (see Figure 7.5a). For the enzyme-surface simulations, an Au $\langle 111 \rangle$ surface with 3 gold layers with dimensions $102 \times 102 \times 20 \text{ \AA}$ was created using a unit cell with lattice constant $a = 2.93$ and unit vectors $(1,0,0)$ and $(1/2, \sqrt{3}/2, 0)$. A cuboidal simulation box with dimensions $102 \times 102 \times 160 \text{ \AA}$ (see Figure 7.5b) was used for the enzyme-surface simulations. It is important to note here that the simulation box XY dimension be equal to that of the gold layer so that periodic boundary conditions can be utilized without errors. The simulation protocol for the gold-enzyme simulations was adapted from Ozboyaci *et al.*¹⁴⁰

The enzyme was placed with the 135CYS residue approximately 7.8 \AA away from the Au surface at the start of the simulation (see Figure 7.5c). The simulation boxes were then solvated using the SPC/E water model^{141,142} and compensated for the net negative charge of the system using Na^+ ions. The structures were energy minimized using a steepest descent method until the maximum net force reached $F_{\text{max}} < 1000 \text{ KJ}^{-1}\text{mol}^{-1}\text{nm}^{-1}$. After the energy minimization, temperature equilibration was performed under an NVT ensemble using the Nose-hoover^{143,144} thermostat at 300 K. For the free enzyme system, the equilibration was performed in a single step

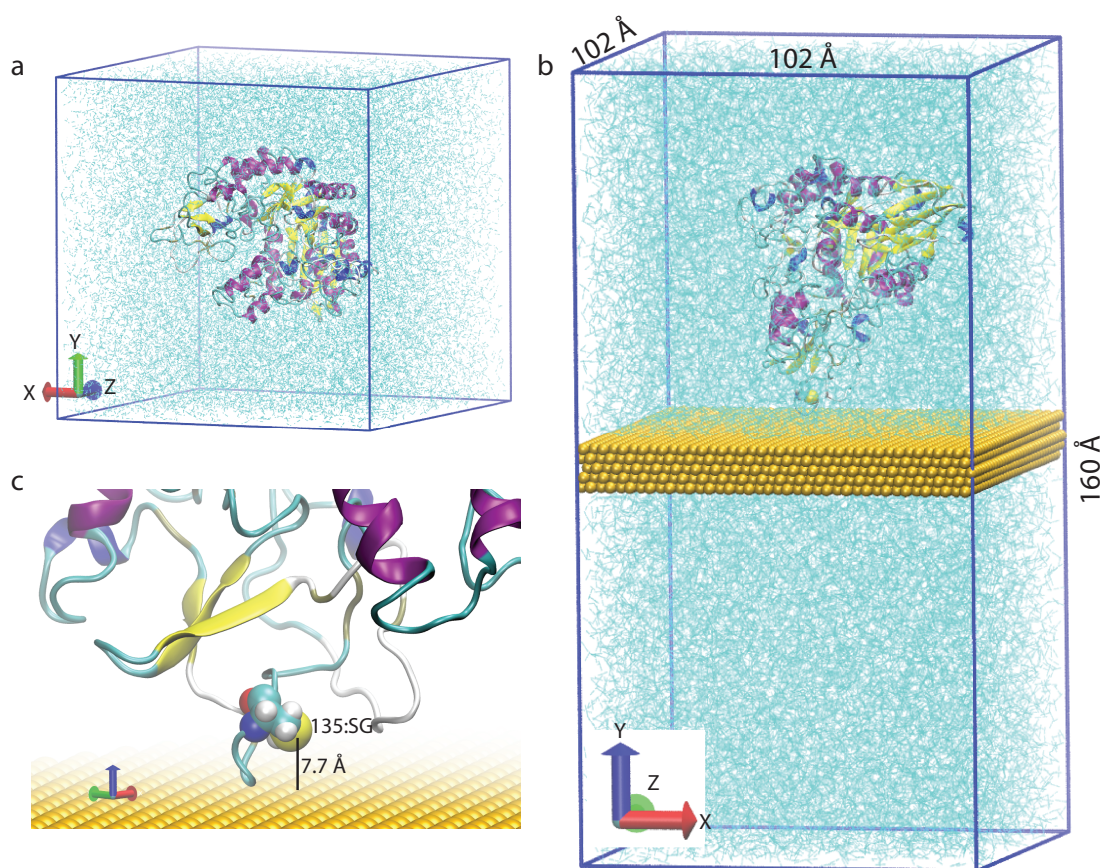


Figure 7.5. (a) The simulation box of S135C MalL solvated in water as solvent. (b) Simulation box of S135C MalL near the surface of a Au $\langle 111 \rangle$ surface solvated in water. (c) A zoom in of the starting configuration of S135C MalL on the surface of the gold. The simulation is started with the Sulphur of the residue CYS-135, 7.8 Å away from the gold surface.

of 50 ps. Whereas, for the enzyme-surface system the equilibration was performed gradually in 300 steps of 1 K with 50 ps per step. During the temperature equilibration, the protein was held using a position restraint and the Au surface atoms were frozen. All bonds containing hydrogen were constrained using the LINCS¹⁴⁵ algorithm. The MD simulations were performed for both systems in an NVT ensemble using a Nose-Hoover thermostat^{143,144} at 300 K. All simulations are performed for 40 ns with a time-step of 2 fs. More details on the simulation are provided in Appendix C.

Figure 7.6a shows the enzyme S135C MalL after 0, 20 and 40 ns of MD simulation. The simulations show that the enzyme rotates and spreads on the Au surface. The amino acid residues including LYS, PRO, ASP, CYS, TYR, GLU, THR, and ARG were found to interact with the gold surface. Figure 7.6b shows a zoom-in of the active site of the enzyme. Figure 7.6c plots the root-mean-square fluctuations (r.m.s.f) of the S135C MalL free in solution (orange) and on a Au $\langle 111 \rangle$ surface (blue). The shaded regions mark the C-alpha atoms near the active site residues. The r.m.s fluctuations of the C-alpha atoms near the active site are increased when the enzyme is interacting with an Au surface. Hobbs *et al.*⁵⁷ studied the impact of mutations on the wildtype enzyme WT MalL and observed that an increase in flexibility of the atoms near the active site caused a decreased catalytic rate. The increased flexibility of the transition state

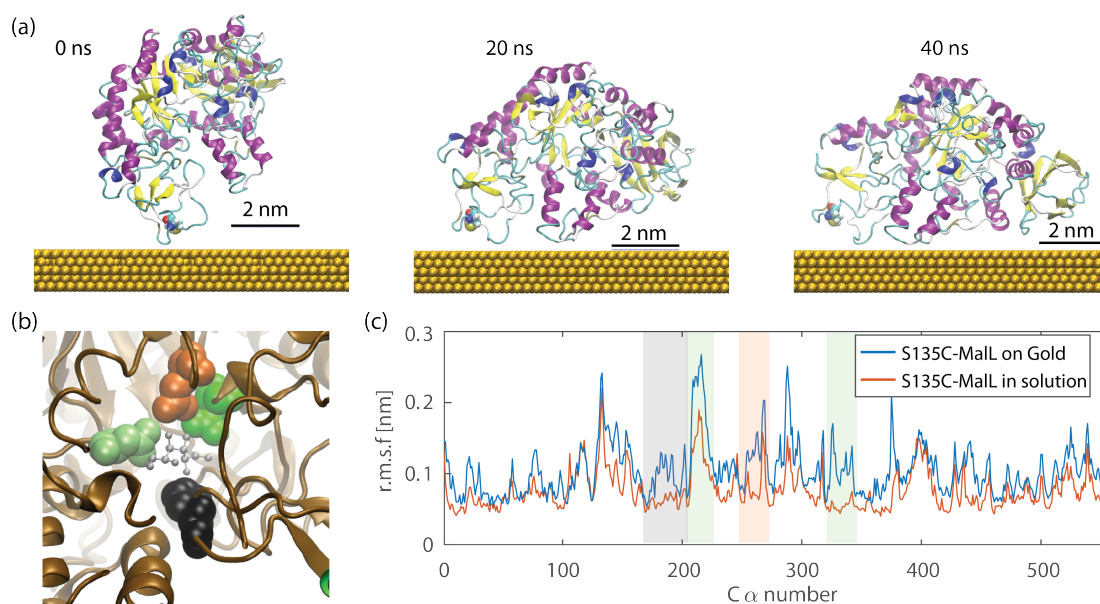


Figure 7.6. (a) Snapshots of S135C MalL on a gold surface at 20 ns time intervals obtained from MD simulations. Representations rendered using VMD.^{133,134} (b) A zoom in of the active site of S135C MalL. The glucose binding residues F144 (black), D199 (green), E255 (orange) and D332 (green) are represented as solid spheres and the D-glucose substrate is represented as ball-and-stick (grey). (c) Root-mean-square fluctuation of the C-alpha atoms of S135C MalL free in solution (orange) and S135C MalL on a gold surface (blue). The shaded regions mark the C-alpha atoms around the active site residues.

causes an increased Gibbs free energy (ΔG) for the reaction and hence a decrease in the enzyme catalytic rate. Although we cannot put much emphasis on single trajectories, the reduced rates we present from the SM measurements below corroborates an effect of the gold on the enzyme dynamics.

7.4 Measuring the enzyme-substrate interaction

After immobilization of the enzyme, the excess free enzyme in the solution is removed by rinsing the sample chamber with the buffer. Then, the signals from the enzyme-substrate interactions are monitored via the PDH error signal. Figure 7.7a shows long-term plots of signals obtained at various steps of the experiment. The signals in Figure 7.7a are downsampled to 2.5 kHz and corrected for drift to improve the presentation (see Section 3.6). Before the immobilization of the enzyme, no discernible peaks above the 3σ noise are found even in the presence of 2mM pNPG substrate (black trace). This shows that the substrate in itself does not interact with the gold nanoparticle. After enzyme immobilization, no spike events are observed indicating that any diffusive movements of the enzyme on the gold surface are restricted. Upon addition of 2 mM pNPG in 20 mM HEPES buffer, spikes above the noise are observed (orange trace). Figure 7.7b shows a 300 ms zoom-in of the signals measured in the presence of enzyme and substrate. The plot shows the single enzyme-substrate interaction 'event'. The plot shows

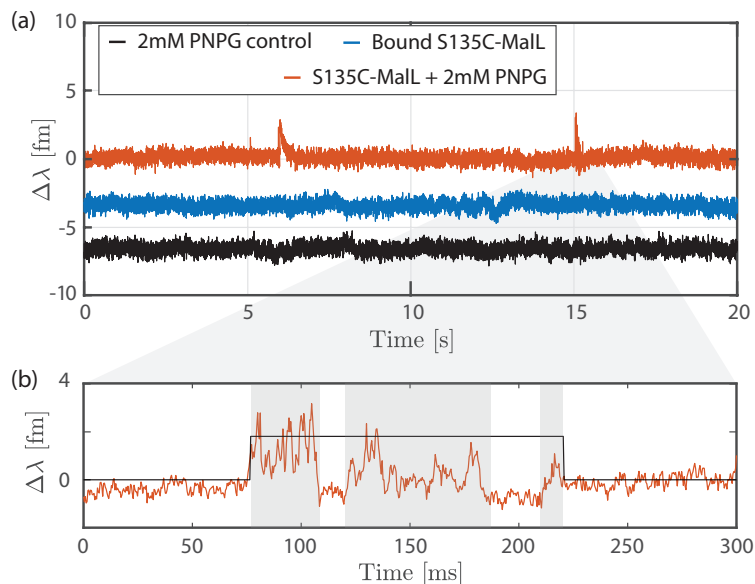


Figure 7.7. (a) Plots of the sensor signals at various steps of the experiment. In the absence of the enzyme, no signals are observed (black) even at high concentrations of the substrate. even upon enzyme immobilization, no spike events are observed (blue). Hence diffusive motion of the enzyme on the surface is restricted. The addition of the substrate after enzyme immobilization results in regular spike events (orange). The traces are offset from zero for clarity. (b) A zoom-in of a 300 ms section of the events measured shows three distinct sub-domains. All measurements were performed at a $\text{pH} \approx 7.2$ in 20 mM HEPES.

that the 'event' is composed of three distinct (shaded regions) sub-domains (see Section 3.6 for peak detection and event classification). About 10-20% of the events contain three or more sub-domains. These events might correspond to the rare turnover event that has been slowed down enough due to the gold-enzyme interaction to enable us to detect the sub-states.

Typically, for SM measurements with simple systems such as DNA hybridization a single exponential adequately fits the Δt data. However, in the case of the enzyme SM data presented here, significant deviations from a single exponential fit are found and a bi-exponential model,

$$S(t) = \sum_{i=1}^{\leq 2} A_i \exp(-k_i t), \quad (7.4)$$

is found to fit the data better. Figure 7.8a plots the survival function $S(\Delta t) = P(T > \Delta t)$ and corresponding exponential fits according to (7.4). Two distinct rate parameters separated by an order of magnitude are provided by the bi-exponential fit. This indicates that two distinct processes can be identified within the SM data provided by Δt . Figure 7.8b plots $S(\tau)$ for the duration of events τ . In this case, the data are adequately fit by a single exponential, and increasing the number of exponentials does not increase the goodness-of-fit. Additionally, a bi-exponential fit to τ data provides two rates that are similar and hence cannot be resolved well by the fit.

Figure 7.9 shows a schematic representation of the processes that likely correspond to the Δt and τ data. For further analysis, we consider the turnover over of the substrate by the enzyme to be

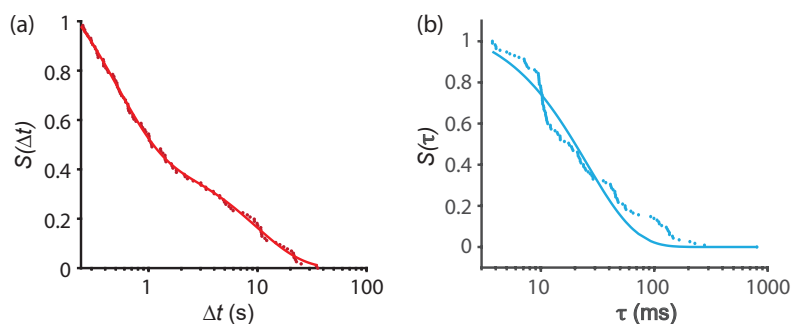


Figure 7.8. (a) Survivor function and the corresponding exponential fits according to (7.4) to time between consecutive events Δt to estimate the rate of events. (b) Survivor function and the corresponding.

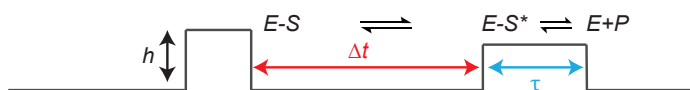


Figure 7.9. Proposed mechanistic scheme of the catalytic reaction.

composed of at least 4 steps, (i) rapid binding of substrate to give E-S (Enzyme-Substrate complex) which is likely faster than our microsecond time resolution; (ii) conformational changes/rearrangement to form the catalytically competent binary complex, ES* (a conformation similar to the transition state), reflected in Δt ; (iii) decay of this complex and chemical turnover to form product E+P (Enzyme + Products), reflected in τ ; (iv) product release and new substrate binding. The multiple rates provided by the SM data further indicate that there exists an equilibrium of E-S complex conformations and interconversion between multiple E-S states that can be resolved. This is consistent with the findings from other SM experiments.^{146–150} Further, the rates obtained from Δt and τ are two orders of magnitude different ($60 - 6000 \text{ min}^{-1}$) and hence turnover would be rate-limited by the process reflected by Δt , the supposed timescale for rearrangement to a catalytically competent binary complex.

7.5 Temperature dependent kinetics of the enzyme

After confirming the activity of the enzyme at the SM level, temperature-dependent measurements were performed. It has to be noted that the results presented henceforth are extracted from a single measurement run across multiple temperature and technical repeats could be performed. All errorbars henceforth present the confidence bounds of the estimation of mean values. Figure 7.10a plots the histogram and corresponding fits of the mean event amplitudes to (4.1). The 3σ background threshold for estimating events is also marked for reference. A log-normal distribution is expected as the event amplitudes arise due to a combination of two main underlying processes. The 5 enzymes are attached to different sites on the gold nanorods and hence experience different intensity enhancements. The site dependence of event amplitudes is distributed in a Poissonian manner. However, the event amplitudes corresponding to a single site are expected to be normally distributed as they experience a similar intensity enhance-

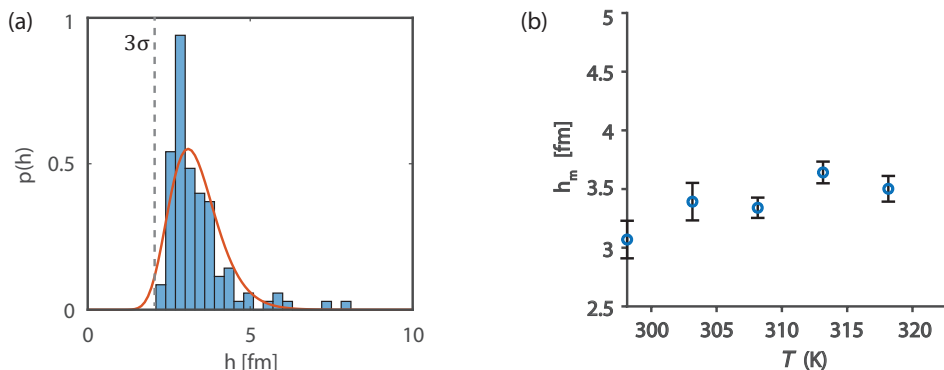


Figure 7.10. (a) Histogram of the event amplitudes and the corresponding log-normal fit according to (7.4). The value of the amplitude threshold 3σ (gray,dashed) is plotted for reference. (b) Temperature dependence of mean event amplitudes h_m . The error bars plot the confidence bounds of the fit to estimate the mean event amplitude. The small gradual increase in h_m from 298 to 318 K indicates that the sensors signals possibly capture conformational fluctuations of the enzyme.

ment. The combination of these two processes results in a log-normal distribution of the event amplitudes. Log-normal distributions of event amplitudes were reported for enzyme kinetics measured with a similar sensor previously.⁵² Such distributions are common in experiments where multiple underlying processes provide the signals as also seen in Chapter 4.

Figure 7.10b plots the estimated mean event amplitude h_m across temperatures from 298-323 K. The associated estimation error (confidence bounds of the fits) is also plotted. The values of h_m show a weak upward trend from 298-318 K. There are two main contributions to the SM signal amplitude, (i) the binding of the substrate and (ii) the conformational fluctuations of the enzyme-substrate complex. The increase in h_m indicates that the SM data contains information about the conformational change of the enzyme since the contribution from the substrate-binding should remain constant. The weak nature of the increase in h_m is expected as the conformational motions of MalL are very small¹³⁰ compared to that of enzymes such as a DNA-polymerase where a larger increase could be observed.⁵² At 323 K, the h_m increases sharply which could indicate enzyme denaturation. However, since this is the last measurement temperature, the data point at this temperature could be an outlier. Further experimental repeats are required to confirm this data point. Hence, measurements at this temperature are excluded from further analysis.

Figure 7.11 plots the temperature dependence of the different rates measured by the sensor. Figure 7.11a plots the survivor function $S(\Delta t)$, and the corresponding fits to the bi-exponential model at different temperatures. The amplitudes A_1 and A_2 are of a similar magnitude, but the rates are an order of magnitude different. Figure 7.11b plots the logarithmic rates $\ln k_1$ and $\ln k_2$ obtained from the exponential fits vs temperature. The corresponding fits to (7.2) are also plotted. Figure 7.11c plots the survivor function $S(\tau)$ and the corresponding single exponential fits. Figure 7.11d plots the temperature dependence of the rate k_τ obtained from the exponential fits at different temperatures. The corresponding fits to (7.2) are also plotted. As illustrated in Figure 7.9, the Δt data likely reflects the formation of a reaction-ready conformation from an

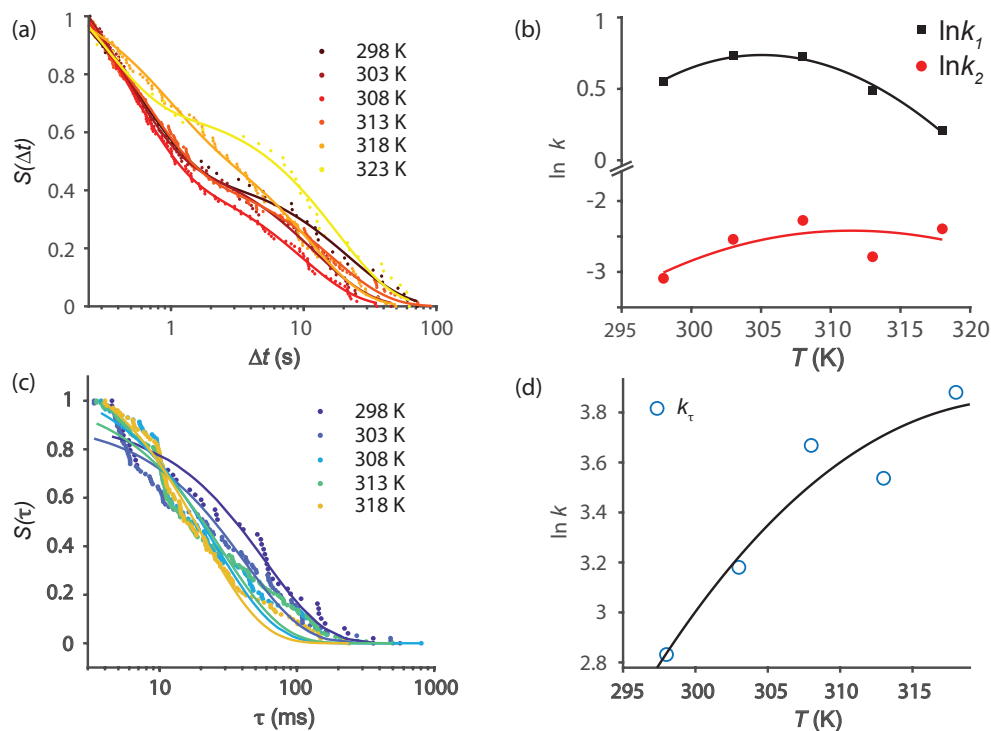


Figure 7.11. Enzymatic rates vs temperature. (a) Survivor function plots and corresponding exponential fits to the Δt data at different temperatures. (b) Temperature dependence of rates $\ln k_{\Delta t}$ shows a negative curvature. (c) Survivor function plots and corresponding exponential fits to the τ data at different temperatures. (d) Logarithmic rate $\ln k_{\tau}$ vs temperature shows a negative curvature.

initial E-S complex which can ultimately decay to a single E-S* conformation. Hence, the SM data resolve at least two different E-S complex geometries that are inter-convertible. Multiple E-S* conformations might exist, however are not accessible from the SM experiments.

Table 7.1. Parameters extracted from fits to (7.2) for the temperature data shown in Figure 7.11.

	Δt		τ
	k_1	k_2	k_{τ}
T_{opt} (K)	305	312	320
$k @ T_{opt}$ (s^{-1})	2	0.08	47.3
ΔH^{\ddagger} (kJmol^{-1}) ^a	-13.6 ± 14.6	10.0 ± 9.5	37.6 ± 11.1
ΔS^{\ddagger} ($\text{kJmol}^{-1}\text{K}^{-1}$) ^a	1.02 ± 0.05	1.06 ± 0.03	1.15 ± 0.04
ΔC_p^{\ddagger} ($\text{kJmol}^{-1}\text{K}^{-1}$)	-5.5 ± 5.1	-2.2 ± 3.4	-2.9 ± 2.6

The rates obtained from both Δt and τ data show significant curvature as with WT MalL at the ensemble level. The parameters extracted from the rate data using the fits to (7.2) are provided in Table 7.1. A negative ΔC_p^{\ddagger} value of -5.5 ± 5.1 and $-2.2 \pm 3.4 \text{ kJmol}^{-1}\text{K}^{-1}$ is obtained for the rates k_1 and k_2 , respectively. As a consequence of the plot curvature, the temperature of theoretical maximum rate can be extracted. From Table 7.1, the optimum temperature T_{opt}

is different by approximately 5 K for k_1 and k_2 . A ΔC_p^\ddagger value of $-2.9 \pm 2.6 \text{ kJmol}^{-1}\text{K}^{-1}$ is obtained for the rate k_τ . The T_{opt} estimated from the k_τ data is 320 K. The maximum rate at T_{opt} estimated from the k_τ data is 47.3 s^{-1} which is similar to that obtained for WT MalL from ensemble measurements. In ensemble measurements, the steady-state turnover was shown to be rate limited by the chemical step¹²⁹ which is supposedly measured by the τ data in our SM sensor. However, in the case of the SM data, the rate-limiting step is the one reflected in the Δt data due to the interaction between the gold surface and enzyme.

7.6 Conclusions

In this chapter, we applied the SM sensor to explore some key biological questions. A new thermodynamic model for enzymatic rates proposed by Hobbs *et al.* recently, namely MMRT, has been explored in ensemble kinetic measurements previously.^{57,129} However, one would ideally wish to capture kinetic data for a single chemical step without the convolution of different steps in the data. In ensemble measurements, the presence of inter-converting conformational sub-states that are differently reactive and the convolution of different chemical steps could give rise to a curvature in the temperature dependence of rates as predicted by MMRT. Using an SM experiment enables us to deconvolve these steps to discern the temperature dependence of discrete kinetic steps and conformational sub-states. The data presented in this chapter show that multiple chemical steps with rates that are different by 1 order of magnitude could possibly be discerned. Although some of these rates might be unique to the enzyme immobilized in the sensor and not present in free enzyme in solution, the curvature in the temperature dependence of all rates provides strong support for the MMRT model. The change in mean amplitude with temperature likely shows that the signals contain the conformational dynamics of the enzyme. The small changes in the measured amplitudes provide a sense for the lower limit of the sensitivity of the WGM-plasmonic hybrid sensor as the change in conformational fluctuations of MalL are quite small in the low Å range. Previously, this sensor was utilized to monitor conformational fluctuations in a DNA-polymerase whose conformational fluctuations are in the range of 10-20 Å.¹⁵¹ However, more experiments have to be performed to establish the results presented in this chapter as technical and biological repeats were not performed. Hence, the results obtained here only provide a first step towards studying single enzyme dynamics.

The higher sensitivity achieved here is due to the new technical features added to the SM sensor in this thesis. The PDH lock-in enabled the detection of signals in the sub-millisecond timescale. The specific immobilization of the enzyme with the active site close to the nanorod surface enables the repeated and sensitive detection of the conformational fluctuations associated with catalysis. It is important to note here that the immobilization does affect the enzyme dynamics. MD simulations performed with the enzyme on the Au surface indicate that a likely change in r.m.s.f of the enzyme backbone upon immobilization results in a decrease in the rate of turnover. Serendipitously, these changes, and the sensitivity of the WGMs, allow us to uncover multiple steps during MalL turnover, which would otherwise not be resolvable. These turnover associated conformational changes likely associate to the steps during MalL turnover based on a scheme

similar to that shown in Figure 7.9. Our study, therefore, provides compelling evidence in support of the MMRT model and its physical underpinning. Additionally, the data point to the power and utility of the plasmonically-enhanced WGM sensor in studying enzyme dynamics and turnover at a high resolution providing insights into complex physical models.

Chapter 8

Conclusions and Outlook

This thesis developed a single-molecule sensing platform capable of studying the thermodynamics of single enzymes. The principle of measurement of the sensor is based on the change in spectral properties of a WGM when a small scatterer interacts with its evanescent field. The change in spectral properties, mainly the shift of the WGM resonance frequency is proportional to the real part of the polarizability of the small scatterer. In Chapter 4, we showed that this is indeed the case by measuring the sign of the shifts of the WGM frequency when asymmetric gold nanoparticles (nanorods) interact with its evanescent field. Theoretically, it was previously reported that the frequency shifts of bare WGM resonator⁷¹ due to the interaction of small biomolecules such as DNA or proteins are smaller than the noise (ultimately limited by the thermal noise for the frequency shift of a single WGM). Hence, either a reduction in the noise or an enhancement of the signal is required. In this work, we achieved the detection of small single molecules via the enhancement of the WGM evanescent field using plasmonic gold nanoparticles. Interaction of small molecules including the binding of thiolated ssDNA and its hybridization with a complementary ssDNA could be measured. However, the signal-to-noise ratio (SNR) measured was typically small. An improvement to the SNR can be obtained by utilizing different plasmonic structures such as nanobipyramids¹⁵² or dimer structures of plasmonic nanoparticles¹⁵³ providing a higher enhancement at the tips or the junction, respectively. The use of particle dimers may be especially useful for large molecules such as proteins which may have only a small overlap with the near-field of a single gold nanoparticle.

On the other hand, the SNR can be further improved by reducing the noise in the system. In the current work, the main source of noise at the timescales of measurement was the laser jitter/frequency noise. A small gain in the SNR may be obtained by utilizing a more stable lower-noise laser source. The frequency shift of a single WGM is limited by the thermal noise due to the small fluctuations in the refractive index of glass or the size of the resonator at room temperature. In Chapter 5, we presented an alternate sensing modality based on the change in frequency splitting of WGMs. The thermal noise limit can be overcome by utilizing this sensing modality as the thermal noise is common for the counter-propagating modes and hence can be canceled out when measuring the mode splitting. Lock-in techniques can be used to extract the mode-splitting with high bandwidth.

An aspect of the sensor to be improved is the robustness and reproducibility of the sensor system. In this work, the WGM resonators were fabricated individually at the tips of glass fibers and placed close to a coupling prism. The distance between the prism surface and the glass resonator has to be maintained (approximately 1 μm) throughout the experiment which is achieved via manual nanopositioning stages. However, depending on the mechanical (length of the fiber attached to a resonator) and the chemical (buffers conditions and surface charges), the resonator may deviate from its original position over the course of the experiment. One way to maintain the position of the resonator is to mount the resonator on a piezo position stage and utilize a feedback control mechanism. Nonetheless, this method is not preferred due to the additional complexity in control design and the use of expensive piezo positioners.

Alternatively, the coupling position of the resonator can be fixed by coating the prism with a solid index matching layer of thickness approximately 1 μm matched to the refractive index of water (typical medium for experiments). For the index matching layer, a fluoropolymer such as CYTOP (Agashi Chemicals, Japan) with refractive index 1.34¹⁵⁴ or Teflon AF 1600 (DuPont, USA) with refractive index 1.31 can be used. The presence of the index matching layer will also allow the use of mass fabricated glass spheres without fiber stems to be utilized for sensing. Hence, prefabricated sensor chips with multiple spheres on a prism surface can be utilized reducing experimental time significantly. Further, microfluidics can be easily integrated with the sensor as the coupling distance will not be affected by the fluid flow. Arrays of microresonators may be assembled and disassembled using liquid flow or air channels integrated as control channels in a PDMS structure.¹⁵⁵ Different functionalizations of sets of microresonators can then be automated for parallel measurements of various samples.

The current implementation of the sensor depends on the self-assembly of the gold nanoparticles with the glass resonator from the solution which does not guarantee the alignment of the nanoparticles with the polarization of the WGM. This issue can be overcome by placing the nanoparticles on the coupler surface (prism in our case) rather than on the resonator. Since the prism is a flat substrate, standard clean-room fabrication techniques can be used to fabricate the nanoparticles. Alternatively, nanoimprinting techniques^{156,157} can be used to place a pattern of wet-chemically synthesized gold nanorods on the prism surface. In these techniques, nanostructures are first patterned on a silicon/silicon nitride substrate using electron beam lithography. Then the pattern is either transferred to a hydrophobic PDMS stamp or made hydrophobic by silanization. The gold nanoparticles can then be trapped in the stamp by a receding meniscus as a drop of the nanoparticle solution is dragged across the hydrophobic stamp surface at an elevated temperature. The stamp can then be used to place the nanorod pattern on the prism surface. The index matching layer of fluoropolymer or optical adhesive will ensure that the gold nanoparticles are close to the WGM resonator surface for maximum enhancement.

In Chapter 7, we showed that the binding of single enzymes and their temperature-dependent activity could be monitored at the single-enzyme level. Further experimental repeats with the MalL and other enzymes will firmly establish the results from this work and pave the way for utilizing optoplasmonic sensors as a platform for single enzyme analysis. The attachment of enzymes to the gold nanoparticles was achieved via a cysteine mutation directly on the enzyme

in this work. The experimental and simulation (MD) results suggest that the direct binding of the enzyme to gold nanorods can substantially affect the dynamics and activity of the enzymes. The impact of the nanoparticle surface on the enzyme can be mitigated by using linker molecules to separate the enzyme from the surface. For example, Dithiobis(C2-NTA) (Dojindo, Japan) is a thiolated molecule that can attach to the gold surface on one end and complex with histidine tags on the N- or C-terminals of purified proteins in the presence of Nickel ions on the other. Similarly, a cysteine residue can be introduced at the end of the histidine tags on the protein to provide a separation of the protein and nanorod surface. Although this process reduces the impact of the surface, the signal enhancement is also reduced as the protein is now further away from the region of maximum enhancement. The precise positioning of the nanoparticle dimers using DNA origami¹⁵⁸ may aid to overcome this issue by allowing the placement of the protein at the junction between the two nanoparticles while allowing for significant enhancement of the electric field.

Finally, additional modalities can be added to the optoplasmonic sensor by combining with other single-molecule techniques such as single-molecule fluorescence microscopy. The optical WGMs may be excited directly using a TIRF objective and signals of the WGM shifts may be acquired simultaneously with fluorescence from single molecules using STORM, PALM, or DNA-PAINT. This would then allow comparison of the signals from each technique and study the impact of these techniques on the system under study. Simultaneous surface-enhanced Raman scattering (SERS) signals may be obtained using a microscope setup similar to the work reported by Huang *et al.*¹⁵⁹ Alternatively, the low-frequency Raman modes (10-100 GHz) of a molecule may be excited using the beat-note of two lasers focused directly on gold nanoparticles attached to the WGM resonator surface. The Raman signals may then be obtained as the change in root-mean-square (r.m.s) fluctuations of the WGM frequency due to enhanced vibrations when the beat-note frequency matches a vibrational mode of the molecule.⁴⁶ This may enable novel molecular fingerprinting using low-frequency Raman modes.

In conclusion, I hope that this thesis serves as a springboard for understanding optoplasmonic sensing and the development of novel single-molecule techniques based on optical microcavities and plasmonic nanoparticles. Hopefully, in the near future, the sensor system presented in this thesis will be developed into a platform for a rapid, repeatable, and easy-to-use sensor for studying chemical and biochemical reactions at the single-molecule level.

Appendix A

Maxwell's equations in spherical coordinates

The analytical solutions of WGMs in spherical resonators is provided in this section. The aim is not to provide a rigorous step-wise derivation of the solutions, but to develop an intuition for the origin of the key parameters of whispering gallery modes in spherical resonators. The solution for the field inside and outside the resonator can be obtained by solving Maxwell's equations with the appropriate boundary conditions. Maxwell's equations relate the electric and magnetic components of the electromagnetic field as follows,

$$\mathbf{curl} \mathbf{E} + \frac{\partial}{\partial t} \mathbf{B} = 0 \quad (\text{A.1a})$$

$$\text{div} \mathbf{B} = 0 \quad (\text{A.1b})$$

$$\text{div} \mathbf{D} = \rho \quad (\text{A.1c})$$

$$\mathbf{curl} \mathbf{H} - \frac{\partial}{\partial t} \mathbf{D} = \mathbf{j}. \quad (\text{A.1d})$$

Here, $\mathbf{E} = \mathbf{E}(\mathbf{r}, t)$ is the electric field vector with \mathbf{r} as a vector in space and t the time variable, $\mathbf{B} = \mathbf{B}(\mathbf{r}, t)$ is the magnetic flux, $\mathbf{D} = \mathbf{D}(\mathbf{r}, t)$ is the electric displacement vector, $\mathbf{H} = \mathbf{H}(\mathbf{r}, t)$ is the magnetic field strength, $\rho = \rho(\mathbf{r}, t)$ is the electric charge density and $\mathbf{j} = \mathbf{j}(\mathbf{r}, t) = \mathbf{j}_s + \mathbf{j}_c$ is the current density in S.I. units. The values \mathbf{j}_s and \mathbf{j}_c are the source current density and the induced current density, respectively.

The auxiliary relations connect the magnetic flux to magnetic field strength and the electric field to the electric displacement as,

$$\mathbf{B} = \mu_0(\mathbf{H} + \mathbf{M}) \quad (\text{A.2a})$$

$$\mathbf{D} = \epsilon_0 \mathbf{E} + \mathbf{P}. \quad (\text{A.2b})$$

Here, \mathbf{M} is the magnetization and \mathbf{P} is the polarization.

For electromagnetic fields in isotropic and linear material, the constitutive relationships give

$$\mathbf{M} = \chi_m \mathbf{H} \quad (\text{A.3a})$$

$$\mathbf{D} = \epsilon_0 \chi_e \mathbf{E} \quad (\text{A.3b})$$

$$\mathbf{j}_c = \sigma \mathbf{E} \quad (\text{A.3c})$$

where, χ_m is the magnetic susceptibility and χ_e is the electric susceptibility and σ is the electric conductivity. Assuming the media is free of induced currents $\mathbf{j}_c = 0$,

$$\mathbf{B} = \mu \mathbf{H} \quad (\text{A.4a})$$

$$\mathbf{D} = \epsilon \mathbf{E} \quad (\text{A.4b})$$

where, $\epsilon = \epsilon_0(1 + \chi_e) = \epsilon_0 \epsilon_r$ is the dielectric permittivity and $\mu = \mu_0 \chi_m = \mu_0 \mu_r$ is the magnetic permeability of the material. Here, the dimensionless quantities ϵ_r and μ_r are termed the relative permittivity and permeability of the material, respectively. The speed of light in the material is given by

$$v = \frac{1}{\sqrt{\mu_r \mu_0 \epsilon_r \epsilon_0}} = \frac{c}{\sqrt{\mu_r \epsilon_r}} \quad (\text{A.5})$$

where $c = \frac{1}{\sqrt{\mu_0 \epsilon_0}}$ is the speed of light in vacuum. The dielectric spherical resonators considered in this work are non-magnetic and hence $\mu_r = 1$. Hence, the speed of light in the medium is $v = c/\sqrt{\epsilon_r} = c/n$, where n is termed the refractive index of the material.

From (A.1) to (A.4) and taking the **curl** of (A.1a) and (A.1d), we get

$$\frac{\partial^2}{\partial t^2} \mathbf{E} - \mu \epsilon \mathbf{E} = 0 \quad (\text{A.6a})$$

$$\frac{\partial^2}{\partial t^2} \mathbf{B} - \mu \epsilon \mathbf{B} = 0. \quad (\text{A.6b})$$

Here, we have used the relation $\mathbf{curl}(\mathbf{curl} \mathbf{V}) = \nabla(\text{div} \mathbf{V}) - \Delta \mathbf{V}$, where \mathbf{V} is a vector function of space variables. Equations (A.6a) and (A.6b) are the vectorial Helmholtz equations. Since, we are looking for sinusoidal fields of the form $\mathbf{V} = \mathbf{V}_0(\mathbf{r}) \exp(i(\omega t + \phi(\mathbf{r})))$ with the angular frequency ω and phase $\phi(\mathbf{r})$, (A.6a) and (A.6b) can be separated into the space and time variables and must satisfy,

$$\underline{\mathbf{E}} + k^2 \underline{\mathbf{E}} = 0 \quad (\text{A.7a})$$

$$\underline{\mathbf{B}} + k^2 \underline{\mathbf{B}} = 0. \quad (\text{A.7b})$$

Here, the substitutions $\mu_r = 1$ and $k^2 = \omega^2 \mu_0 \epsilon$ have been made, where k is the wave number, $\underline{\mathbf{E}} = \mathbf{E}_0(\mathbf{r}) \exp(i\phi(\mathbf{r}))$ and $\underline{\mathbf{B}} = \mathbf{B}_0(\mathbf{r}) \exp(i\phi(\mathbf{r}))$.

In the spherical coordinate system with space variables (r, θ, ϕ) , the solutions to (A.7) are obtained using the vectorial spherical harmonic functions and the Ricatti-Bessel functions. The vectorial spherical harmonics can be derived from by scalar counterparts using the Hansen

method⁹³ and are defined as follows,

$$\mathbf{X}_l^m = \nabla Y_l^m \times \mathbf{r} / \sqrt{l(l+1)} \quad (\text{A.8a})$$

$$\mathbf{Y}_l^m = r \nabla Y_l^m / \sqrt{l(l+1)} \quad (\text{A.8b})$$

$$\mathbf{Z}_l^m = Y_l^m \hat{\mathbf{r}}, \quad (\text{A.8c})$$

where $Y_l^m = Y_l^m(\theta, \phi)$ are the scalar spherical harmonics. The Ricatti-Bessel functions are defined as follows,

$$\psi_l(x) = \sqrt{\frac{\pi x}{2}} J_{l+\frac{1}{2}}(x) \quad (\text{A.9a})$$

$$\chi_l(x) = -\sqrt{\frac{\pi x}{2}} Y_{l+\frac{1}{2}}(x), \quad (\text{A.9b})$$

where $J(x)$ and $Y(x)$ are the Bessel's functions of the first and second kind, respectively. The vectorial spherical harmonics provide the angular distribution of the fields, while the Ricatti-Bessel functions provide the radial component. The number l is an integer value that provides the order of the spherical harmonic Y_l^m is called the mode number. The number m can take $2l + 1$ integer values from $-l$ to l and is called the azimuthal mode number.

Appendix B

Notes on sensor assembly and gold nanorod functionalization

The WGM-plasmonic hybrid sensor presented in this thesis depends on the plasmonic enhancement of the gold nanoparticles attached to the glass microsphere for detecting single entities in solution. This Appendix provides more details and some common issues with sensor assembly and functionalization of the gold nanorods used for sensing. One of the key steps in sensor assembly is the attachment of the gold nanorod to the WGM cavity surface. Section 4.1.2 described a procedure based on the electrostatic attachment of CTAB coated nanorods on the cavity surface using a low pH method. Although this method provides an easy and efficient method of assembling the nanorods on the cavity surface, the robustness of the attached nanorods in various buffers is low. Typically, the nanorods remain stable in buffers with $\text{pH} \approx 3 - 8$ even with high ionic strength (1 M NaCl). However, at higher pH and in buffers containing surfactants such as SDS or Tween20, the stability of the attachment is reduced. Figure B.1a shows a photograph of the WGM microsphere on the experimental setup. The rectangular boxes mark the region where gold nanoparticles are attached to the microsphere surface. The scattering from the gold nanoparticles is clearly visible. Figure B.1b plots the normalized intensity fluctuations within the rectangular regions indicated in Figure B.1a when the cavity is immersed in a solution of 0.2% SDS. It can be seen that while the changes in intensity within region I is negligible, the intensity of region II fluctuates considerably. These changes in intensity arise from a change in scattering from the nanorod within the region. The scattering of the nanorod changes due to the motion of the nanorod on the surface of the microsphere. The SDS surfactant interacts with the CTAB molecule on the nanorod and destabilizes the attachment of the nanorod to the glass surface. The destabilization of the nanorods depends on various uncontrolled factors such as the orientation of the nanoparticle on the surface, the density of CTAB on the particle and the contact surface area between the nanoparticle and the glass. Hence, particle in region I with likely more dense CTAB coating and higher surface contact is more stable compared to particle II. In conclusion, it is important to test any new buffers after sensor assembly to exclude the interaction of the buffer with the sensor.

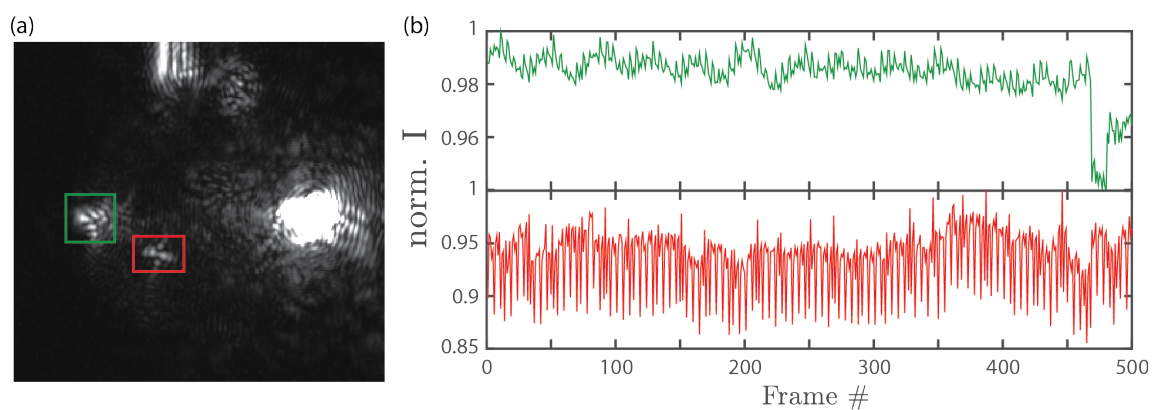


Figure B.1. (a) Photograph of the spherical micro resonator in the experimental setup. The rectangular boxes mark a region with nanoparticles attached to the resonator. (b) Intensity fluctuations within the rectangular regions of due to change in scattering from the nanoparticles attached on the microsphere surface in 0.2% SDS solution.

Appendix C

All-atom molecular dynamics simulations in GROMACS

Molecular dynamics (MD) are simulations that enable the computational study of complex biological problems such as protein stability, conformational changes, protein folding, protein-ligand interaction, and transport in biological systems. At the simplest, MD simulates the motion of atoms described in 3D space over time by solving the classical Newtonian equations of motion. A biomolecule is represented as a set of points in 3D space. The initial static 3D positions of each atom of a biomolecule such as a protein can be obtained from experimental methods such as X-ray crystallography or Cryo-electron microscopy with extremely high precision in the single-digit Årange. The Protein Data Bank (PDB) provides a free repository for all published structures of various biomolecules. Once the positions and initial velocities of the atoms in biomolecules are known (initial velocities can be generated based on a specified temperature), the time evolution of the system can be simulated by simply solving the Newtonian equations. The two simple equations governing MD simulations are,

$$\mathbf{F}_i = \frac{d\mathbf{p}_i}{dt} \tag{C.1a}$$

$$\mathbf{F}_i = -\nabla U \tag{C.1b}$$

where \mathbf{F}_i is the net force on an atom number i , \mathbf{p}_i is the momentum vector and U is the potential energy of the system. From an initial state of the system and known potential energy, the final state of the system after a small time-step is simulated by solving (C.1). Obtaining accurate results from an MD simulation requires simulating very small time-steps in the order of a fs and hence long time simulations in the order of μs - ms involves hundreds of thousands of simulation steps. The computational cost of such a simulation is massive even for small systems with a few thousand atoms and is difficult to process in practical timescales for modern supercomputers. In this thesis, we perform 50 ns simulations due to the computational cost and the resources available.

MD simulations hence require an accurate description of the potential energy of the system

for providing realistic outcomes of the system dynamics. For a system with biomolecules such as proteins/enzymes, the potential energy is described by two sets of equations defining the bonded (dealing with atomic bonds) and non-bonded (dealing with electrostatic and Van der Waals interactions). The bonded part of the potential energy is typically separated into different interactions as follows,

$$U_{bond}(r_{ij}) = \frac{1}{2}k_{ij}^b(r_{ij} - r_{ij}^0)^2 \quad (\text{C.2a})$$

$$U_{angle}(\theta_{ijk}) = \frac{1}{2}k_{ijk}^\theta(\theta_{ijk} - \theta_{ijk}^0)^2 \quad (\text{C.2b})$$

$$U_{proper}(\phi_{ijkl}) = k_\phi(1 + \cos(n\phi - \phi_s)) \quad (\text{C.2c})$$

$$U_{improper}(\epsilon_{ijkl}) = \frac{1}{2}k_\epsilon(\epsilon_{ijkl} - \epsilon_{ijkl}^0)^2. \quad (\text{C.2d})$$

Here, U_{bond} defines the bond length r_{ij} stretching potential between atoms i and k , U_{angle} defines bond-angle θ_{ijk} stretching between atoms i, j and k , U_{proper} is the potential describing the proper dihedral angle ϕ between ijk and jkl planes and $U_{improper}$ ⁱ defines improper dihedral potential between planes ijk and jkl with improper dihedral angle ϵ_{ijkl} between the planes. The terms k_{ij}^b , k_{ijk}^θ , k_ϕ , k_ϵ and r_{ij}^0 , θ_{ijk}^0 , ϕ_s , ϵ_{ijkl}^0 are constants that vary for each set of atoms. The non-bonded potential energies are typically given as,

$$U_{Coulomb}(r_{ij}) = \sum_{i < j} \frac{1}{4\pi\epsilon_0} \frac{q_i q_j}{r_{ij}} \quad (\text{C.3a})$$

$$U_{LJ}(r_{ij}) = \sum_{i < j} \frac{A_{ij}}{r_{ij}^{12}} - \frac{B_{ij}}{r_{ij}^6}, \quad (\text{C.3b})$$

where, $U_{Coulomb}$ describes the electrostatic interactions and U_{LJ} describes the Van der Waals interactions, q_i , q_j are the partial charges on atoms i and j , r_{ij} is the interatomic distance, A_{ij} and B_{ij} are constants.

The complete set of parameters (force constants, ideal bond lengths, bond angles, improper dihedrals, proper dihedrals, partial charges, Van der Waals constants) describing the interaction between different types of particles is called a force field. Typically, these parameters are obtained empirically or via *ab-initio* quantum mechanical calculations using Discrete Functional Theory (DFT). Many different parameterizations exist such as ff14SB,¹⁶⁰ CHARMM¹⁶¹ and OPLS-AA.¹³⁸ These force fields are in constant refinement to provide more accurate simulations of biomolecular systems. The solutions to (C.1) are obtained numerically using the force field parameters as inputs. Along with many force fields, there exist a multitude of open-source massively parallelized solvers such as NAMD,²⁸ LAMMPS,²⁹ and GROMACS.³⁰ In this thesis, the OPLS-AAⁱⁱ force field¹³⁸ is used to simulate the dynamics of the enzyme. An extension to the OPLS-AA to include interactions of amino acids with gold < 111 > layers known as GolP-OPLS¹³⁹ is used to simulate the enzyme-gold interactions. The simulations were performed

ⁱThe improper dihedrals are meant to keep groups in plane (e.g. in aromatic rings) or prevent molecules from flipping to their mirror images.

ⁱⁱThe OPLS force field uses the Ryckaert-Bellemans function for proper dihedral potential as $U_{proper}(\phi_{ijkl}) = \sum_{n=0}^5 C_n(\cos(\phi - 180^\circ))^n$

using the GROMACS software package.¹³⁷ The main steps for performing MD simulations as described below. A detailed step-wise tutorial for simulating a protein using GROMACS is available online at <http://www.mdtutorials.com/gmx/lysozyme/>.

The goal of the MD simulations here is to study the effect of the gold surface of the enzyme attached to it. Hence, two different simulations were performed, one for enzyme-free in solvent (water) and one for enzymes near an Au < 111 > surface. The first step in the simulation process is to set up the simulation geometry. Since setting up the system for the enzyme gold interaction is more complex, the procedure of the enzyme-gold simulation is described below. The settings for the free enzyme simulation can be obtained by simply deleting the parts related to the gold layer.

C.1 Creating the simulation geometry

First, the coordinate file for the mutated enzyme S135C MalL is generated using the mutation functions available in VMD starting from the base structure file available in PDB entry 4M56. A topology file that contains all the parameters required to define the enzyme in the simulation is generated using `pdb2gmx` and stored in the file `"s135c.itp"`. To include the Au < 111 > surface, new atom types have to be defined in the force field according to the definitions in GoIP-OPLS. The `"atomtypes.atp"` was edited to include new atom types as follows,

```
1 ; Atom types of AU layer
2 ; Name      mass
3 AUB        196.97      ; Gold in Bulk
4 AUC         0.5        ; Gold Dipole (to account for polarization)
5 AUS        196.97      ; Gold on Surface
6 AUA        196.97      ; Gold on Surface near binding of S (Sulphur)
7 AUE        196.97      ; Gold at Edge
8 AUV        196.97      ; Gold at Vertex
9 AUI        196.97      ; Virtual Gold interaction site
10 AUJ       196.97      ; Virtual Gold interaction site near S binding
11 AUD       196.97      ; Dummy Gold interaction site for S binding
```

New molecule types defining the gold surface atoms, gold virtual interaction types, and gold bulk atoms are defined as follows,

```

1 [ moleculetype ]
2 ; Name          nrexcl
3 GoldSurface     3
4 [ atoms ]
5 ;  nr          type  resnr  residue  atom  cgnr    charge    mass
   typeB        chargeB      massB
6  1            AUS    1     AUS     AU   1       -0.3     196.97  ;
   qtot 0
7  2            AUC    1     AUS     AUC  2        0.3      0.5    ;
   qtot 0
8
9 [ constraints ]
10 1 2 1 0.07
11
12 #ifdef GOLDPOSRES
13 [ position_restraints ]
14     1  1  GLDFX  GLDFY  GLDFZ
15 #endif
16
17 #ifdef GPOSRES
18 [ position_restraints ]
19     1  1 1000 1000 1000
20     2  1 1000 1000 1000
21 #endif

```

```

1 [ moleculetype ]
2 ; Name          nrexcl
3 GoldVirtualSite 3
4 [ atoms ]
5 ;  nr          type  resnr  residue  atom  cgnr    charge    mass
   typeB        chargeB      massB
6  1            AUI    1     AUI     AUI   1        0.0     196.97  ;
   qtot 0
7
8 #ifdef GOLDPOSRES
9 [ position_restraints ]
10     1  1  GLDFX  GLDFY  GLDFZ
11 #endif
12
13 #ifdef GPOSRES
14 [ position_restraints ]
15     1  1 1000 1000 1000
16 #endif

```

```

1 [ moleculetype ]
2 ; Name          nrexcl
3 GoldBulk        3

```

```
4 [ atoms ]
5 ;   nr      type  resnr  residue  atom  cgnr   charge   mass
      typeB    chargeB      massB
6   1      AUB    1     AUB    AU     1     -0.3    196.97 ;
      qtot 0
7   2      AUC    1     AUB    AUC    2     0.3     0.5    ;
      qtot 0
8
9 [ constraints ]
10 1 2 1 0.07
11
12 #ifdef GOLDPOSRES
13 [ position_restraints ]
14     1  1 GLDFX GLDFY GLDFZ
15 #endif
16
17 #ifdef GPOSRES
18 [ position_restraints ]
19     1  1 1000 1000 1000
20     2  1 1000 1000 1000
21 #endif
```

The gold layer is then generated from a **fcc** unit cell with lattice constant $a = 2.93 \text{ \AA}$. Three layers of gold atoms with Au surface layers on top and bottom are generated with dimensions $102 \times 102 \times 20 \text{ \AA}$ as shown in Figure 7.5b. The AUC atoms are generated randomly at a fixed distance of 0.07 \AA from the AUS or AUB atoms. The gold virtual sites are situated at $(a/2, a/2\sqrt{3}, 0)$ and $(-a/2, -a/2\sqrt{3}, 0)$ in each surface unit cell. A simulation box of size $102 \times 102 \times 160 \text{ \AA}$ is created to enclose the system. The XY dimensions of the box fit exactly with the XY size of the gold layer to avoid any improper interactions of the solvent or protein with the gold atoms on the sides due to periodic boundary conditions. The Z size is chosen to be large enough so that there are no interactions of the enzyme with its image.¹⁴⁰

C.2 Topology file, solvation and neutralization

To simulate realistic physiological conditions, the system is solvated, that is solvent molecules (water) are added to the simulation. The resulting simulation geometry is shown in Figure 7.4. Next, the system is neutralized by adding counter-ions equal to the net charge of the system. This can be performed automatically in GROMACS using the tool `genion` by replacing water molecules in the system with ions. The net charge of the S135C Mall system is $-21e$ and hence 21 Na^+ ions were added to neutralize the system. The final topology file looks as follows,

```

1 ; Include forcefield parameters
2 #include "../oplsaag.ff/forcefield.itp"
3
4 ; Include protein topology
5 #include "s135c.itp"
6
7 ; Include gold topologies
8 #include "../oplsaag.ff/gold_bulk.itp"
9 #include "../oplsaag.ff/gold_virtual.itp"
10 #include "../oplsaag.ff/gold_surface.itp"
11
12 ; Include water topology
13 #include "../oplsaag.ff/spce.itp"
14
15 #ifdef POSRES_WATER
16 ; Position restraint for each water oxygen
17 [ position_restraints ]
18 ; i funct      fcx      fcy      fcz
19   1    1      1000      1000      1000
20 #endif
21
22
23 ; Include generic topology for ions
24 #include "../oplsaag.ff/ions.itp"
25
26 [ system ]
27 ; Name
28 Mall on gold in water
29
30 [ molecules ]
31 ; Compound      #mols
32 Protein_chain_X      1
33 GoldBulk            4175
34 GoldVirtualSite     5600
35 GoldSurface         2800
36 SOL                 60395
37 NA                  21

```

C.3 Energy minimization

Before starting an actual simulation run, we have to ensure that the system has an appropriate geometry and no steric clashes. Hence, the structure is gradually relaxed into a minimum configuration using an energy minimization step. The energy minimization is performed using the steepest descent integrator until the maximum force $F < 1000 \text{ KJmol}^{-1}\text{nm}^{-1}$. A new group containing all AU atoms are created using `make_ndx` for use with `freezegrps`. All Au atoms are thus frozen in place in all directions as the gold Au atoms are much heavier than the rest. This reduces the simulation cost considerably. The following input file is used with `grompp` to create the simulation run,

```

1 ; minim.mdp - used as input into grompp to generate em.tpr
2 ; define = -DFLEXIBLE
3 ; Parameters describing what to do, when to stop, and what to save
4 integrator = steep ; Algorithm (steep = steepest descent
   minimization)
5 emtol = 1000.0 ; Stop minimization when the maximum force
   < 1000.0 kJ/mol/nm
6 emstep = 0.01 ; Minimization step size in ps
7 nsteps = 50000 ; Maximum number of (minimization) steps to
   perform
8
9 nstlist = 1 ; Frequency to update the neighbor list and
   long range forces
10 cutoff-scheme = Verlet ; Buffered neighbor searching
11 ns_type = grid ; Method to determine neighbor list (simple
   , grid)
12 coulombtype = PME ; Treatment of long range electrostatic
   interactions
13 rcoulomb = 1.0 ; Short-range electrostatic cut-off
14 rvdw-switch = 0.90 ;
15 rvdw = 1.0 ; Short-range Van der Waals cut-off
16 pbc = xyz ; Periodic Boundary Conditions in all 3
   dimensions
17
18 ; Many warnings of large rotations of rods
19 ; may appear in the initial few ps of the simulation
20 ; to prevent them:
21 lincs_warnangle = 80
22
23 ; To keep au surface in place, freeze Au atoms.
24 ; The AU group has been defined via make_ndx
25 ; to contain all the AU atoms ('a AU').
26 freezegrps = AU AUI ; Freeze groups of AU and AUI
27 freezedim = Y Y Y Y Y Y ; freeze all dimensions
28 comm-mode = None ;

```

C.4 Temperature equilibration

After ensuring a reasonable starting structure by energy minimization, the solvent and ions must be equilibrated around the protein. Temperature equilibration is required to optimize the solvent and ion orientation with the solute for the system at the simulation temperature (300 K in our case). The equilibration is conducted under an *NVT* ensemble (constant Number of particles, Volume, and Temperature). Position restraints are applied to heavy atoms of the enzyme (other than hydrogen) so the solvent can be equilibrated around the enzyme without structural changes to the enzyme. The following input file is used in *grompp* in combination with position restraints to create the simulation files,

```

1 title          = NVT equibriation for S135C Mall on Au layer
2 define         = -DPOSRES ; position restrain the protein
3 ; Run parameters
4 integrator    = md          ; leap-frog integrator
5 nsteps        = 25000       ; 2 * 50000 = 100 ps
6 dt            = 0.002       ; 2 fs
7 ; Output control
8 nstxout       = 1000        ; save coordinates every 0.2 ps
9 nstvout       = 1000        ; save velocities every 0.2 ps
10 nstenergy     = 1000       ; save energies every 0.2 ps
11 nstlog        = 1000       ; update log file every 0.2 ps
12 ; Bond parameters
13 continuation = yes         ; first dynamics run
14 constraint_algorithm = lincs ; holonomic constraints
15 constraints    = h-bonds    ; all bonds (even heavy atom-H
    bonds) constrained
16 lincs_iter     = 1          ; accuracy of LINCS
17 lincs_order    = 4          ; also related to accuracy
18 ; Neighborsearching
19 cutoff-scheme = Verlet     ; Buffered neighbor searching
20 ns_type        = grid      ; search neighboring grid cels
21 nstlist        = 10        ; 20 fs, largely irrelevant with Verlet
22 nsttcouple     = 2         ;
23 rlist          = 1         ; short-range neighborlist cutoff (in nm)
24 rcoulomb       = 1         ; short-range electrostatic cutoff (in nm)
25 rvdw           = 1         ; short-range van der Waals cutoff (in nm)
26 rvdw-switch    = 0.9       ; where to start switching the LJ force
27 vdw-type       = cut-off    ; Twin range cut-offs with neighbor list cut
    -off
28 vdw-modifier= Potential-shift ; Shift the Van der Waals potential by
    a constant such that it is zero at the cut-off
29
30 ewald_rtol     = 1e-6
31 ; Electrostatics
32 coulombtype    = PME        ; Particle Mesh Ewald for long-range
    electrostatics
33 pme_order      = 4          ; cubic interpolation

```



```

34 fourierspacing = 0.10      ; grid spacing for FFT
35 ; Temperature coupling is on
36 tcoupl        = nose-hoover      ; modified Berendsen
    thermostat
37 tc-grps       = Protein Water_and_ions AUS AUB AUI ; two coupling groups
    - more accurate
38 tau_t         = 0.1          0.1      0.1 0.1 0.1 ; time constant, in
    ps
39 ref_t         = 300          300      300 300 300 ; reference
    temperature, one for each group, in K
40 ; Pressure coupling is off
41 pcoupl        = no            ; no pressure coupling in NVT
42 ; Periodic boundary conditions
43 pbc           = xyz          ; 3-D PBC
44 ; Dispersion correction
45 DispCorr      = EnerPres     ; account for cut-off vdW scheme
46 ; Velocity generation
47 gen_vel       = no          ; assign velocities from Maxwell distribution
48 gen_temp      = 300         ; temperature for Maxwell distribution
49 gen_seed      = -1         ; generate a random seed
50
51 ; Many warnings of large rotations of rods
52 ; may appear in the initial few ps of the simulation
53 ; to prevent them:
54 lincs_warnangle = 80
55 ; To keep au surface in place, freeze Au atoms.
56 ; The AU group has been defined via make_ndx
57 ; to contains all the AU atoms ('a AU').
58 freezegrps    = AU AUI
59 freezedim     = Y Y Y Y Y Y
60 comm_mode     = None

```

The equilibration is performed for a duration of 50 ps in steps of 1 K. The value of `ref_t` is changed from 1-300 K incrementally in each step. The equilibration has to be performed in steps to avoid large kinetic energy differences between steps that can lead to the system exploding.

C.5 Production MD run

After equilibration under an *NVT* ensemble, typically a pressure equilibration is performed under an *NPT* ensemble. However, since GOLP-OPLS is not validated under an *NPT* ensemble, this step is skipped in our simulations. This may result in clashes between solvent and solute molecules during the course of the simulation. We have carefully checked the simulation trajectory and found no clashes and hence an *NVT* ensemble is sufficient for our simulations. The production run of the MD simulation is run of 50 ns per simulation using the following input file to `grompp`,

```

1 title = GolP-OPLS Mall interaction with a Au <111>
   surface
2 ; Run parameters
3 integrator = md ; leap-frog integrator
4 nsteps = 25000000 ; 2 * 500000 = 1000 ps (1 ns)
5 dt = 0.002 ; 2 fs
6
7 ; Output control
8 nstxout = 0 ; suppress bulky .trr file by
   specifying
9 nstvout = 0 ; 0 for output frequency of nstxout
   ,
10 nstfout = 0 ; nstvout, and nstfout
11 nstenergy = 5000 ; save energies every 10.0 ps
12 nstlog = 5000 ; update log file every 10.0 ps
13 nstxout-compressed = 5000 ; save compressed coordinates every
   10.0 ps
14 compressed-x-grps = System ; save the whole system
15
16 ; Bond parameters
17 continuation = yes ; Restarting after NPT
18 constraint_algorithm = lincs ; holonomic constraints
19 constraints = h-bonds ; bonds involving H are constrained
20 lincs_iter = 1 ; accuracy of LINCS
21 lincs_order = 4 ; also related to accuracy
22
23 ; Neighorsearching
24 cutoff-scheme = Verlet ; Buffered neighbor searching
25 ns_type = grid ; search neighboring grid cells
26 nstlist = 10 ; 20 fs, largely irrelevant with
   Verlet scheme
27 nsttcouple = 2 ; temperature coupling frequency
28 nhchainlength = 1 ; chain length set to 1 for md
   integrator
29 rcoulomb = 1.0 ; short-range electrostatic cutoff
   (in nm)
30 rvdw = 1.0 ; short-range van der Waals cutoff
   (in nm)

```

```
31 rvdw-switch          = 0.90          ; switching distance for short-
    range van der Waals (in nm)
32
33 ; Electrostatics
34 coulombtype          = PME           ; Particle Mesh Ewald for long-
    range electrostatics
35 pme_order            = 4             ; cubic interpolation
36 ewald_rtol           = 1e-6         ;
37 fourierspacing       = 0.10         ; grid spacing for FFT
38
39 ; Temperature coupling is on
40 tcoupl               = nose-hoover   ; Nose-Hoover
    thermostat
41 tc_grps              = Protein Water_and_ions AUS AUB AUI ;
    multiple groups - more accurate
42 tau_t                = 0.1          0.1          0.1 0.1 0.1 ; time
    constant, in ps
43 ref_t                = 300          300          300 300 300 ;
    reference temperature, one for each group, in K
44
45 ; Pressure coupling is off
46 pcoupl               = no           ; no pressure coupling in NVT
47
48 ; Periodic boundary conditions
49 pbc                  = xyz          ; 3-D PBC
50
51 ; Dispersion correction
52 DispCorr             = EnerPres     ; account for cut-off vdW scheme
53
54 ; Velocity generation
55 gen_vel              = no           ; Velocity generation is off
56
57 ; prevent warning due to large rod rotations in the first few steps
58 lincs_warnangle      = 80
59
60 ; To keep au surface in place, freeze Au atoms.
61 freezegrps           = AU AUI       ; AU group created using make_ndx
    ('a AU')
62 freezedim            = Y Y Y Y Y Y   ; freeze all dimensions
63 comm_mode            = None         ; no common mode correction
```

Bibliography

- [1] Eric Betzig, George H. Patterson, Rachid Sougrat, O. Wolf Lindwasser, Scott Olenych, Juan S. Bonifacino, Michael W. Davidson, Jennifer Lippincott-Schwartz, and Harald F. Hess. Imaging Intracellular Fluorescent Proteins at Nanometer Resolution. *Science*, 313(5793):1642–1645, sep 2006.
- [2] Michael J. Rust, Mark Bates, and Xiaowei Zhuang. Sub-diffraction-limit imaging by stochastic optical reconstruction microscopy (STORM). *Nature Methods*, 3(10):793–795, 2006.
- [3] Stefan W. Hell and Jan Wichmann. Breaking the diffraction resolution limit by stimulated emission: stimulated-emission-depletion fluorescence microscopy. *Optics Letters*, 19(11):780, jun 1994.
- [4] W. E. Moerner. New directions in single-molecule imaging and analysis. *Proceedings of the National Academy of Sciences*, 104(31):12596–12602, jul 2007.
- [5] Christoph Dellago and Peter G Bolhuis. Transition Path Sampling Simulations of Biological Systems. In Markus Reiher, editor, *Atomistic Approaches in Modern Biology*, pages 291–317. Springer Berlin Heidelberg, Berlin, Heidelberg, 2007.
- [6] Katherine Henzler-Wildman and Dorothee Kern. Dynamic personalities of proteins. *Nature*, 450(7172):964–972, 2007.
- [7] H M Berman, J Westbrook, Z Feng, G Gilliland, T N Bhat, H Weissig, I N Shindyalov, and P E Bourne. The protein data bank. *Nucleic acids research*, 28(1):235–242, 2000.
- [8] R H Austin, K Beeson, Eisenstein L, H Frauenfelder, and Gunsalus I. Ligand binding to myoglobin. *Biochem*, 14(24):5355–5373, 1975.
- [9] Hans Frauenfelder, Gregory A. Petsko, and Demetrius Tsernoglou. Temperature-dependent X-ray diffraction as a probe of protein structural dynamics. *Nature*, 280(5723):558–563, 1979.
- [10] D Beece, L Eisenstein, Hans Frauenfelder, D Good, M.C. Marden, L Reinisch, A.H. Reynolds, L.B. Sorensen, and K.T. Yue. Solvent Viscosity and Protein Dynamics. *Biochemistry*, 18(11):2139–2145, 1979.

-
- [11] Charles L. Brooks and Martin Karplus. Solvent effects on protein motion and protein effects on solvent motion. Dynamics of the active site region of lysozyme. *Journal of Molecular Biology*, 208(1):159–181, 1989.
- [12] H Frauenfelder, S. Sligar, and P. Wolynes. The energy landscapes and motions of proteins. *Science*, 254(5038):1598–1603, 1991.
- [13] Shaodong Dai, Rosmarie Friemann, Dominique A. Glauser, Florence Bourquin, Wanda Manieri, Peter Schürmann, and Hans Eklund. Structural snapshots along the reaction pathway of ferredoxin–thioredoxin reductase. *Nature*, 448(7149):92–96, 2007.
- [14] D. Bourgeois and M. Weik. *Kinetic protein crystallography: a tool to watch proteins in action*, volume 15. Taylor & Francis, 2009.
- [15] Yifan Cheng. Single-particle Cryo-EM at crystallographic resolution. *Cell*, 161(3):450–457, 2015.
- [16] Alexey G. Kikhney and Dmitri I. Svergun. A practical guide to small angle X-ray scattering (SAXS) of flexible and intrinsically disordered proteins. *FEBS Letters*, 589(19):2570–2577, 2015.
- [17] A. G. Palmer, C. D. Kroenke, and J. P. Loria. Nuclear magnetic resonance methods for quantifying microsecond-to-millisecond motions in biological macromolecules. *Methods in Enzymology*, 339:204–238, 2001.
- [18] Lewis E. Kay. NMR studies of protein structure and dynamics. *Journal of Magnetic Resonance*, 173(2):193–207, 2005.
- [19] I. R. Kleckner and M. P. Foster. An Introduction to NMR based approaches for measuring protein dynamics. *Biochimica et Biophys Acta (BBA) - Proteins and Proteomics*, 1814(8):942–968, 2011.
- [20] Michael Kovermann, Per Rogne, and Magnus Wolf-Watz. Protein dynamics and function from solution state NMR spectroscopy. *Quarterly Reviews of Biophysics*, 49:e6, 2016.
- [21] Keir C Neuman and Attila Nagy. Single-molecule force spectroscopy: optical tweezers, magnetic tweezers and atomic force microscopy. *Nature methods*, 5(6):491–505, 2008.
- [22] Michael T. Woodside and Steven M. Block. Reconstructing Folding Energy Landscapes by Single-Molecule Force Spectroscopy. *Annual Review of Biophysics*, 43(1):19–39, 2014.
- [23] X Michalet, S Weiss, and M Jager. Single-molecule fluorescence studies of protein folding and conformational dynamics. *Chem. Rev.*, 106:1785–1813, 2006.
- [24] H. Yang. Protein Conformational Dynamics Probed by Single-Molecule Electron Transfer. *Science*, 302(5643):262–266, 2003.
- [25] L Stryer and R P Haugland. ENERGY TRANSFER: A SPECTROSCOPIC RULER. *Annual Review of Biochemistry*, 47(1):819–846, 1978.
-

-
- [26] Hoi Sung Chung and William A. Eaton. Single-molecule fluorescence probes dynamics of barrier crossing. *Nature*, 502(7473):685–688, 2013.
- [27] S A Adcock and J A McCammon. Molecular dynamics: survey of methods for simulating the activity of proteins. *Chem. Rev.*, 106:1589–1615, 2006.
- [28] James C. Phillips, Rosemary Braun, Wei Wang, James Gumbart, Emad Tajkhorshid, Elizabeth Villa, Christophe Chipot, Robert D. Skeel, Laxmikant Kalpa, and Klaus Schulten. Scalable molecular dynamics with NAMD. *Journal of Computational Chemistry*, 26(16):1781–1802, 2005.
- [29] S. Plimpton. Fast Parallel Algorithms for Short – Range Molecular Dynamics. *Journal of Computational Physics*, 117(June 1994):1–19, 1995.
- [30] Sander Pronk, Szilárd Páll, Roland Schulz, Per Larsson, Pär Bjelkmar, Rosten Apostolov, Michael R. Shirts, Jeremy C. Smith, Peter M. Kasson, David Van Der Spoel, Berk Hess, and Erik Lindahl. GROMACS 4.5: A high-throughput and highly parallel open source molecular simulation toolkit. *Bioinformatics*, 29(7):845–854, 2013.
- [31] Martin Karplus and Joseph N. Kushick. Method for estimating the configurational entropy of macromolecules. *Macromolecules*, 14(2):325–332, 1981.
- [32] T Haliloglu, I Bahar, and B Erman. Gaussian dynamics of folded proteins. *Phys. Rev. Lett.*, 79:3090–3093, 1997.
- [33] D J Jacobs, A J Rader, L A Kuhn, and M F Thorpe. Protein flexibility predictions using graph theory. *Proteins*, 44:150–165, 2001.
- [34] Valentina Tozzini. Coarse-grained models for proteins. *Current Opinion in Structural Biology*, 15(2):144–150, 2005.
- [35] David E. Shaw, Kevin J. Bowers, Edmond Chow, Michael P. Eastwood, Douglas J. Jerardi, John L. Klepeis, Jeffrey S. Kuskin, Richard H. Larson, Kresten Lindorff-Larsen, Paul Maragakis, Mark A. Moraes, Ron O. Dror, Stefano Piana, Yibing Shan, Brian Towles, John K. Salmon, J. P. Grossman, Kenneth M. Mackenzie, Joseph A. Bank, Cliff Young, Martin M. Deneroff, and Brannon Batson. Millisecond-scale molecular dynamics simulations on Anton. *Proceedings of the Conference on High Performance Computing Networking, Storage and Analysis - SC '09*, page 1, 2009.
- [36] Kresten Lindorff-Larsen, Paul Maragakis, Stefano Piana, and David E. Shaw. Picosecond to Millisecond Structural Dynamics in Human Ubiquitin. *Journal of Physical Chemistry B*, 120(33):8313–8320, 2016.
- [37] Adam B. Taylor and Peter Zijlstra. Single-Molecule Plasmon Sensing: Current Status and Future Prospects. *ACS Sensors*, 2(8):1103–1122, aug 2017.
- [38] Jolly Xavier, Serge Vincent, Fabian Meder, and Frank Vollmer. Advances in optoplasmonic sensors – combining optical nano/microcavities and photonic crystals with plasmonic nanostructures and nanoparticles. *Nanophotonics*, 7(1):1–38, jan 2018.
-

-
- [39] Eugene Kim, Martin D. Baaske, and Frank Vollmer. Towards next-generation label-free biosensors: recent advances in whispering gallery mode sensors. *Lab Chip*, 17(7):1190–1205, 2017.
- [40] Yanyan Zhi, Xiao-Chong Yu, Qihuang Gong, Lan Yang, and Yun-Feng Xiao. Single Nanoparticle Detection Using Optical Microcavities. *Advanced Materials*, 29(12):1604920, mar 2017.
- [41] Sivaraman Subramanian, Hsin-Yu Wu, Tom Constant, Jolly Xavier, and Frank Vollmer. Label-Free Optical Single-Molecule Micro- and Nanosensors. *Advanced Materials*, 30(51):1801246, dec 2018.
- [42] Peter Zijlstra, Pedro M.R. Paulo, and Michel Orrit. Optical detection of single non-absorbing molecules using the surface plasmon resonance of a gold nanorod. *Nature Nanotechnology*, 7(6):379–382, 2012.
- [43] Yuanjie Pang and Reuven Gordon. Optical trapping of a single protein. *Nano Letters*, 12(1):402–406, 2012.
- [44] Daniel V. Verschueren, Sergii Pud, Xin Shi, Lorenzo De Angelis, L. Kuipers, and Cees Dekker. Label-Free Optical Detection of DNA Translocations through Plasmonic Nanopores. *ACS Nano*, 13(1):61–70, 2019.
- [45] Michael A. Beuwer, Menno W. J. Prins, and Peter Zijlstra. Stochastic Protein Interactions Monitored by Hundreds of Single-Molecule Plasmonic Biosensors. *Nano Letters*, 15(5):3507–3511, may 2015.
- [46] Skyler Wheaton, Ryan M. Gelfand, and Reuven Gordon. Probing the Raman-active acoustic vibrations of nanoparticles with extraordinary spectral resolution. *Nature Photonics*, 9(1):68–72, 2014.
- [47] Xin Shi, Daniel V. Verschueren, and Cees Dekker. Active Delivery of Single DNA Molecules into a Plasmonic Nanopore for Label-Free Optical Sensing. *Nano Letters*, 18(12):8003–8010, dec 2018.
- [48] Calin Plesa, Stefan W Kowalczyk, Ruben Zinsmeister, Alexander Y Grosberg, Yitzhak Rabin, and Cees Dekker. Fast Translocation of Proteins through Solid State Nanopores. *Nano Letters*, 13(2):658–663, feb 2013.
- [49] Reuven Gordon. [INVITED] Biosensing with nanoaperture optical tweezers. *Optics & Laser Technology*, 109:328–335, jan 2019.
- [50] Irene Ament, Janak Prasad, Andreas Henkel, Sebastian Schmachtel, and Carsten Sönnichsen. Single Unlabeled Protein Detection on Individual Plasmonic Nanoparticles. *Nano Letters*, 12(2):1092–1095, feb 2012.
- [51] Eugene Kim, Martin D. Baaske, and Frank Vollmer. In Situ Observation of Single-Molecule Surface Reactions from Low to High Affinities. *Advanced Materials*, 28(45):9941–9948, 2016.
-

-
- [52] Eugene Kim, Martin D Baaske, Isabel Schultes, Peter S Wilsch, and Frank Vollmer. Label-free optical detection of single enzyme-reactant reactions and associated conformational changes. *Science Advances*, 3(3):e1603044, mar 2017.
- [53] Wenyan Yu, Wei C Jiang, Qiang Lin, and Tao Lu. Cavity optomechanical spring sensing of single molecules. *Nature Communications*, 7:12311, 2016.
- [54] Feng Liang, Yuzheng Guo, Shaocong Hou, and Qimin Quan. Photonic-plasmonic hybrid single-molecule nanosensor measures the effect of fluorescent labels on DNA-protein dynamics. *Science Advances*, 3(5):e1602991, may 2017.
- [55] F. Vollmer, D. Braun, A. Libchaber, M. Khoshshima, I. Teraoka, and S. Arnold. Protein detection by optical shift of a resonant microcavity. *Applied Physics Letters*, 80(21):4057–4059, may 2002.
- [56] Sivaraman Subramanian, Serge Vincent, and Frank Vollmer. Effective linewidth shifts in single-molecule detection using optical whispering gallery modes. *Applied Physics Letters*, 117(15):151106, oct 2020.
- [57] Joanne K. Hobbs, Wanting Jiao, Ashley D. Easter, Emily J. Parker, Louis A. Schipper, and Vickery L. Arcus. Change in Heat Capacity for Enzyme Catalysis Determines Temperature Dependence of Enzyme Catalyzed Rates. *ACS Chemical Biology*, 8(11):2388–2393, nov 2013.
- [58] M Kuwata-Gonokami, R H Jordan, a Dodabalapur, H E Katz, M L Schilling, R E Slusher, and S Ozawa. Polymer microdisk and microring lasers. *Optics letters*, 20(20):2093–2095, 1995.
- [59] W. Bogaerts, P. De Heyn, T. Van Vaerenbergh, K. De Vos, S. Kumar Selvaraja, T. Claes, P. Dumon, P. Bienstman, D. Van Thourhout, and R. Baets. Silicon microring resonators. *Laser & Photonics Reviews*, 6(1):47–73, jan 2012.
- [60] D K Armani, T J Kippenberg, S M Spillane, and K J Vahala. Ultra-high-Q toroid microcavity on a chip. *Nature*, 421(6926):925–928, 2003.
- [61] Tobias J. Kippenberg and K. J Vahala. Cavity Optomechanics: Back-Action at the Mesoscale. *Science*, 321(5893):1172–1176, 2008.
- [62] T J Kippenberg, R Holzwarth, and S A Diddams. Microresonator-based optical frequency combs. *Science (New York, N.Y.)*, 332(6029):555–559, 2011.
- [63] M Sumetsky. Whispering-gallery-bottle microcavities: the three-dimensional etalon. *Optics letters*, 29(1):8–10, 2004.
- [64] Vishnu Kavungal. *Optical Whispering Gallery Mode Cylindrical Micro-Resonator Devices for Sensing Applications*. PhD thesis, Dublin Institute of Technology, 2018.
- [65] F Vollmer, S Arnold, and D Keng. Single virus detection from the reactive shift of a whispering-gallery mode. *Proceedings of the National Academy of Sciences of the United States of America*, 105(52):20701–20704, 2008.
-

-
- [66] Lord Rayleigh. CXII.The problem of the whispering gallery. *Philosophical Magazine Series 6*, 20(120):1001–1004, 1910.
- [67] Lord Rayleigh. IX.Further applications of Bessel’s functions of high order to the Whispering Gallery and allied problems. *Philosophical Magazine Series 6*, 27(157):100–109, 1914.
- [68] G. C. Righini, Y. Dumeige, P. Féron, M. Ferrari, G. Nunzi Conti, D. Ristic, and S. Soria. Whispering Gallery Mode microresonators: Fundamentals and applications. *Rivista del Nuovo Cimento*, 34(7):435–488, 2011.
- [69] C. C. Lam, P. T. Leung, and K. Young. Explicit asymptotic formulas for the positions, widths, and strengths of resonances in Mie scattering. *Journal of the Optical Society of America B*, 9(9):1585, sep 1992.
- [70] Stéphane Balac and Patrice Féron. Whispering gallery modes volume computation in optical micro-spheres. Research report, FOTON, UMR CNRS 6082, December 2014.
- [71] Matthew R Foreman, Wei-Liang Jin, and Frank Vollmer. Optimizing detection limits in whispering gallery mode biosensing. *Optics express*, 22(5):5491–511, 2014.
- [72] Matthew R. Foreman, Jon D. Swaim, and Frank Vollmer. Whispering gallery mode sensors. *Advances in Optics and Photonics*, 7(2):168, jun 2015.
- [73] Gustav Schweiger and Marion Horn. Effect of changes in size and index of refraction on the resonance wavelength of microspheres. *Journal of the Optical Society of America B*, 23(2):212, feb 2006.
- [74] Niranjana M. Hanumegowda, Caleb J. Stica, Bijal C. Patel, Ian White, and Xudong Fan. Refractometric sensors based on microsphere resonators. *Applied Physics Letters*, 87(20):201107, nov 2005.
- [75] S Arnold, M Khoshshima, I Teraoka, S Holler, and F Vollmer. Shift of whispering-gallery modes in microspheres by protein adsorption. *Optics letters*, 28(4):272–274, 2003.
- [76] Iwao Teraoka and Stephen Arnold. Theory of resonance shifts in TE and TM whispering gallery modes by nonradial perturbations for sensing applications. *Journal of the Optical Society of America B*, 23(7):1381, jul 2006.
- [77] Jiangang Zhu, Sahin Kaya Ozdemir, Yun-Feng Xiao, Lin Li, Lina He, Da-Ren Chen, and Lan Yang. On-chip single nanoparticle detection and sizing by mode splitting in an ultrahigh-Q microresonator. *Nature Photonics*, 4(1):46–49, 2010.
- [78] Jan Wiersig. Structure of whispering-gallery modes in optical microdisks perturbed by nanoparticles. *Physical Review A*, 84(6):063828, dec 2011.
- [79] Markus Aspelmeyer, Tobias J. Kippenberg, and Florian Marquardt. Cavity optomechanics. *Reviews of Modern Physics*, 86(December), 2014.
-

-
- [80] Venkata R Dantham, Stephen Holler, Curtis Barbre, David Keng, Vasily Kolchenko, and Stephen Arnold. Label-Free Detection of Single Protein Using a Nanoplasmonic-Photonic Hybrid Microcavity. *Nano Letters*, 13(7):3347–3351, jul 2013.
- [81] Martin D Baaske, Matthew R Foreman, and Frank Vollmer. Single-molecule nucleic acid interactions monitored on a label-free microcavity biosensor platform. *Nature Nanotechnology*, 9(August):1–7, 2014.
- [82] Lina He, Şahin Kaya Özdemir, Jiengang Zhu, Woosung Kim, and Lan Yang. Detecting single viruses and nanoparticles using whispering gallery microlasers. *Nature Nanotechnology*, 6(7):428–432, 2011.
- [83] J. Abadie, B. P. Abbott, R. Abbott, T. D. Abbott, M. Abernathy, C. Adams, R. Adhikari, C. Affeldt, P. Ajith, B. Allen, G. S. Allen, E. Amador Ceron, D. Amariutei, R. S. Amin, S. B. Anderson, W. G. Anderson, K. Arai, M. A. Arain, M. C. Araya, S. M. Aston, D. Atkinson, P. Aufmuth, C. Aulbert, B. E. Aylott, S. Babak, P. Baker, S. Ballmer, D. Barker, B. Barr, P. Barriga, L. Barsotti, M. A. Barton, I. Bartos, R. Bassiri, M. Bastarrika, J. Batch, J. Bauchrowitz, B. Behnke, A. S. Bell, I. Belopolski, M. Benacquista, J. M. Berliner, A. Bertolini, J. Betzwieser, N. Beveridge, P. T. Beyersdorf, I. A. Bilenko, G. Billingsley, J. Birch, R. Biswas, E. Black, J. K. Blackburn, L. Blackburn, D. Blair, B. Bland, O. Bock, T. P. Bodiya, C. Bogan, R. Bondarescu, R. Bork, M. Born, S. Bose, P. R. Brady, V. B. Braginsky, J. E. Brau, J. Breyer, D. O. Bridges, M. Brinkmann, M. Britzger, A. F. Brooks, D. A. Brown, A. Brummitt, A. Buonanno, J. Burguet-Castell, O. Burmeister, R. L. Byer, L. Cadonati, J. B. Camp, P. Campsie, J. Cannizzo, K. Cannon, J. Cao, C. D. Capano, S. Caride, S. Caudill, M. Cavagliá, C. Cepeda, T. Chalermongsak, E. Chalkley, P. Charlton, S. Chelkowski, Y. Chen, N. Christensen, H. Cho, S. S.Y. Chua, S. Chung, C. T.Y. Chung, G. Ciani, F. Clara, D. E. Clark, J. Clark, J. H. Clayton, R. Conte, D. Cook, T. R. Corbitt, M. Cordier, N. Cornish, A. Corsi, C. A. Costa, M. Coughlin, P. Couvares, D. M. Coward, D. C. Coyne, J. D.E. Creighton, T. D. Creighton, A. M. Cruise, A. Cumming, L. Cunningham, R. M. Cutler, K. Dahl, S. L. Danilishin, R. Dannenberg, K. Danzmann, B. Daudert, H. Daveloza, G. Davies, E. J. Daw, T. Dayanga, D. DeBra, J. Degallaix, T. Dent, V. Dergachev, R. DeRosa, R. DeSalvo, S. Dhurandhar, J. DiGuglielmo, I. DiPalma, M. Díz, F. Donovan, K. L. Dooley, S. Dorsner, R. W.P. Drever, J. C. Driggers, Z. Du, J. C. Dumas, S. Dwyer, T. Eberle, M. Edgar, M. Edwards, A. Effler, P. Ehrens, R. Engel, T. Etzel, K. Evans, M. Evans, T. Evans, M. Factourovich, S. Fairhurst, Y. Fan, B. F. Farr, W. Farr, D. Fazi, H. Fehrmann, D. Feldbaum, L. S. Finn, R. P. Fisher, M. Flanigan, S. Foley, E. Forisi, N. Fotopoulos, M. Frede, M. Frei, Z. Frei, A. Freise, R. Frey, T. T. Fricke, D. Friedrich, P. Fritschel, V. V. Frolov, P. J. Fulda, M. Fyffe, M. R. Ganija, J. Garcia, J. A. Garofoli, R. Geng, L. Gergely, S. Ghosh, J. A. Giaime, S. Giampanis, K. D. Giardina, C. Gill, E. Goetz, L. M. Goggin, G. González, M. L. Gorodetsky, S. Goßler, C. Graef, A. Grant, S. Gras, C. Gray, N. Gray, R. J.S. Greenhalgh, A. M. Gretarsson, R. Grosso, H. Grote, S. Grunewald, C. Guido, R. Gupta, E. K. Gustafson, R. Gustafson, T. Ha, B. Hage, J. M. Hallam, D. Hammer, G. Hammond, J. Hanks, C. Hanna, J. Hanson, J. Harms, G. M. Harry, I. W. Harry, E. D.
-

Harstad, M. T. Hartman, K. Haughian, K. Hayama, J. Heefner, M. C. Heintze, M. A. Hendry, I. S. Heng, A. W. Heptonstall, V. Herrera, M. Hewitson, S. Hild, D. Hoak, K. A. Hodge, K. Holt, T. Hong, S. Hooper, D. J. Hosken, J. Hough, E. J. Howell, B. Hughey, T. Huynh-Dinh, S. Husa, S. H. Huttner, D. R. Ingram, R. Inta, T. Isogai, A. Ivanov, K. Izumi, M. Jacobson, H. Jang, W. W. Johnson, D. I. Jones, G. Jones, R. Jones, L. Ju, P. Kalmus, V. Kalogera, I. Kamaretsos, S. Kandhasamy, G. Kang, J. B. Kanner, E. Katsavounidis, W. Katzman, H. Kaufer, K. Kawabe, S. Kawamura, F. Kawazoe, W. Kells, D. G. Keppel, Z. Keresztes, A. Khalaidovski, F. Y. Khalili, E. A. Khazanov, B. Kim, C. Kim, D. Kim, H. Kim, K. Kim, N. Kim, Y. M. Kim, P. J. King, M. Kinsey, D. L. Kinzel, J. S. Kissel, S. Klimenko, K. Kokeyama, V. Kondrashov, R. Kopparapu, S. Koranda, W. Z. Korth, D. Kozak, V. Kringel, S. Krishnamurthy, B. Krishnan, G. Kuehn, R. Kumar, P. Kwee, P. K. Lam, M. Landry, M. Lang, B. Lantz, N. Lastzka, C. Lawrie, A. Lazzarini, P. Leaci, C. H. Lee, H. M. Lee, N. Leindecker, J. R. Leong, I. Leonor, J. Li, P. E. Lindquist, N. A. Lockerbie, D. Lodhia, M. Lormand, J. Luan, M. Lubinski, H. Lück, A. P. Lundgren, E. Macdonald, B. Machenschalk, M. MacInnis, D. M. Macleod, M. Mageswaran, K. Mailand, I. Mandel, V. Mandic, A. Marandi, S. Márka, Z. Márka, A. Markosyan, E. Maros, I. W. Martin, R. M. Martin, J. N. Marx, K. Mason, F. Matichard, L. Matone, R. A. Matzner, N. Mavalvala, G. Mazzolo, R. McCarthy, D. E. McClelland, S. C. McGuire, G. McIntyre, J. McIver, D. J.A. McKechnan, G. D. Meadors, M. Mehmet, T. Meier, A. Melatos, A. C. Melissinos, G. Mendell, D. Menendez, R. A. Mercer, S. Meshkov, C. Messenger, M. S. Meyer, H. Miao, J. Miller, V. P. Mitrofanov, G. Mitselmakher, R. Mittleman, O. Miyakawa, B. Moe, P. Moesta, S. D. Mohanty, D. Moraru, G. Moreno, T. Mori, K. Mossavi, C. M. Mow-Lowry, C. L. Mueller, G. Mueller, S. Mukherjee, A. Mullavey, H. Müller-Ebhardt, J. Munch, D. Murphy, P. G. Murray, A. Mytidis, T. Nash, R. Nawrodt, V. Necula, J. Nelson, G. Newton, A. Nishizawa, D. Nolting, L. Nuttall, J. O'Dell, B. O'Reilly, R. O'Shaughnessy, E. Ochsner, E. Oelker, J. J. Oh, S. H. Oh, G. H. Ogin, R. G. Oldenburg, C. Osthelder, C. D. Ott, D. J. Ottaway, R. S. Ottens, H. Overmier, B. J. Owen, A. Page, Y. Pan, C. Pankow, M. A. Papa, P. Patel, M. Pedraza, P. Peiris, L. Pekowsky, S. Penn, C. Peralta, A. Perreca, M. Phelps, M. Pickenpack, I. M. Pinto, M. Pitkin, H. J. Pletsch, M. V. Plissi, J. Pöld, F. Postiglione, V. Predoi, L. R. Price, M. Prijatelj, M. Principe, S. Privitera, R. Prix, L. Prokhorov, O. Puncken, V. Quetschke, F. J. Raab, H. Radkins, P. Raffai, M. Rakhmanov, C. R. Ramet, B. Rankins, S. R.P. Mohapatra, V. Raymond, K. Redwine, C. M. Reed, T. Reed, S. Reid, D. H. Reitze, R. Riesen, K. Riles, N. A. Robertson, C. Robinson, E. L. Robinson, S. Roddy, C. Rodriguez, M. Rodruck, J. Rollins, J. D. Romano, J. H. Romie, C. Röver, S. Rowan, A. Rüdiger, K. Ryan, H. Ryll, P. Sainathan, M. Sakosky, F. Salemi, A. Sambrowski, L. Sammut, L. De La Sancho Jordana, V. Sandberg, S. Sankar, V. Sannibale, L. Santamaría, I. Santiago-Prieto, G. Santostasi, B. S. Sathyaprakash, S. Sato, P. R. Saulson, R. L. Savage, R. Schilling, S. Schlamminger, R. Schnabel, R. M.S. Schofield, B. Schulz, B. F. Schutz, P. Schwinberg, J. Scott, S. M. Scott, A. C. Searle, F. Seifert, D. Sellers, A. S. Sengupta, A. Sergeev, D. A. Shaddock, M. Shaltev, B. Shapiro, P. Shawhan, D. H. Shoemaker, A. Sibley, X. Siemens, D. Sigg, A. Singer, L. Singer, A. M. Sintes, G. Skelton, B. J.J. Slagmolen, J. Slutsky, R. J.E. Smith, J. R. Smith, M. R. Smith, N. D. Smith,

- K. Somiya, B. Sorazu, J. Soto, F. C. Speirits, A. J. Stein, E. Steinert, J. Steinlechner, S. Steinlechner, S. Steplewski, M. Stefszky, A. Stochino, R. Stone, K. A. Strain, S. Strigin, A. S. Stroeer, A. L. Stuver, T. Z. Summerscales, M. Sung, S. Susmithan, P. J. Sutton, D. Talukder, D. B. Tanner, S. P. Tarabrin, J. R. Taylor, R. Taylor, P. Thomas, K. A. Thorne, K. S. Thorne, E. Thrane, A. Thüring, C. Titsler, K. V. Tokmakov, C. Torres, C. I. Torrie, G. Traylor, M. Trias, K. Tseng, D. Ugolini, K. Urbanek, H. Vahlbruch, M. Vallisneri, A. A. VanVeggel, S. Vass, R. Vaulin, A. Vecchio, J. Veitch, P. J. Veitch, C. Veltkamp, A. E. Villar, S. Vitale, C. Vorvick, S. P. Vyatchanin, A. Wade, S. J. Waldman, L. Wallace, Y. Wan, A. Wanner, X. Wang, Z. Wang, R. L. Ward, P. Wei, M. Weinert, A. J. Weinstein, R. Weiss, L. Wen, S. Wen, P. Wessels, M. West, T. Westphal, K. Wette, J. T. Whelan, S. E. Whitcomb, D. White, B. F. Whiting, C. Wilkinson, P. A. Willems, H. R. Williams, L. Williams, B. Willke, L. Winkelmann, W. Winkler, C. C. Wipf, H. Wittel, A. G. Wiseman, G. Woan, R. Wooley, J. Worden, J. Yablon, I. Yakushin, K. Yamamoto, H. Yamamoto, H. Yang, D. Yeaton-Massey, S. Yoshida, P. Yu, M. Zanolin, F. Zhang, L. Zhang, W. Zhang, Z. Zhang, C. Zhao, N. Zotov, M. E. Zucker, and J. Zweigig. A gravitational wave observatory operating beyond the quantum shot-noise limit. *Nature Physics*, 7(12):962–965, dec 2011.
- [84] Changhyoup Lee, Frederik Dieleman, Jinhyoung Lee, Carsten Rockstuhl, Stefan A. Maier, and Mark Tame. Quantum Plasmonic Sensing: Beyond the Shot-Noise and Diffraction Limit. *ACS Photonics*, 3(6):992–999, jun 2016.
- [85] R. W P Drever, J. L. Hall, F. V. Kowalski, J. Hough, G. M. Ford, a. J. Munley, and H. Ward. Laser phase and frequency stabilization using an optical resonator. *Applied Physics B Photophysics and Laser Chemistry*, 31(2):97–105, 1983.
- [86] Jens M Dobrindt. *Bio-sensing using toroidal microresonators & Theoretical cavity optomechanics*. PhD thesis, Ludwig–Maximilians–University of Munich, 2012.
- [87] Jon D. Swaim, Joachim Knittel, and Warwick P. Bowen. Detection limits in whispering gallery biosensors with plasmonic enhancement. *Applied Physics Letters*, 99(24):243109, dec 2011.
- [88] S. Arnold, R. Ramjit, D. Keng, V. Kolchenko, and I. Teraoka. MicroParticle photophysics illuminates viral bio-sensing. *Faraday Discuss.*, 137:65–83, 2008.
- [89] Krishnendu Saha, Sarit S Agasti, Chaekyu Kim, Xiaoning Li, and Vincent M Rotello. Gold Nanoparticles in Chemical and Biological Sensing. *Chemical Reviews*, 112(5):2739–2779, may 2012.
- [90] Dakrong Pissuwan, Stella M. Valenzuela, and Michael B. Cortie. Therapeutic possibilities of plasmonically heated gold nanoparticles. *Trends in Biotechnology*, 24(2):62–67, 2006.
- [91] Cuiping Yao, Luwei Zhang, Jing Wang, Yulu He, Jing Xin, Sijia Wang, Hao Xu, and Zhenxi Zhang. Gold Nanoparticle Mediated Phototherapy for Cancer. *Journal of Nanomaterials*, 2016:1–29, 2016.

-
- [92] Stefan A. Maier. *Plasmonics: Fundamentals and Applications*, volume 677. Springer US, New York, NY, sep 2007.
- [93] John David Jackson. *Classical electrodynamics*. Third edition. New York : Wiley, [1999] ©1999, 1999.
- [94] P. B. Johnson and R. W. Christy. Optical Constants of the Noble Metals. *Physical Review B*, 6(12):4370–4379, dec 1972.
- [95] J. B. Khurgin and G. Sun. Enhancement of optical properties of nanoscaled objects by metal nanoparticles. *Journal of the Optical Society of America B*, 26(12):B83, dec 2009.
- [96] Jürgen Waxenegger, Andreas Trügler, and Ulrich Hohenester. Plasmonics simulations with the MNPBEM toolbox: Consideration of substrates and layer structures. *Computer Physics Communications*, 193:138–150, aug 2015.
- [97] A B Matsko, A A Savchenkov, D Strekalov, V S Ilchenko, and L Maleki. Review of Applications of Whispering-Gallery Mode Resonators in Photonics and Nonlinear Optics. *PRism*, 42(162):1–51, 2005.
- [98] Michael L. Gorodetsky and Vladimir S. Ilchenko. Optical microsphere resonators: optimal coupling to high-Q whispering gallery modes. *J. Opt. Soc. Am.*, 16(1):14, 1998.
- [99] Martin D. Baaske and Frank Vollmer. Optical observation of single atomic ions interacting with plasmonic nanorods in aqueous solution. *Nature Photonics*, 10(11):733–739, 2016.
- [100] Abraham Savitzky and M. J. E. Golay. Smoothing and Differentiation of Data by Simplified Least Squares Procedures. *Analytical Chemistry*, 36(8):1627–1639, jul 1964.
- [101] M. Zimbone, L. Calcagno, G. Messina, P. Baeri, and G. Compagnini. Dynamic light scattering and UV–vis spectroscopy of gold nanoparticles solution. *Materials Letters*, 65(19-20):2906–2909, oct 2011.
- [102] Hadas Weinrib, Amihai Meiri, Hamootal Duadi, and Dror Fixler. Uniformly Immobilizing Gold Nanorods on a Glass Substrate. *Journal of Atomic, Molecular, and Optical Physics*, 2012:1–6, jun 2012.
- [103] Htet H. Kyaw, Salim H. Al-Harhi, Azzouz Sellai, and Joydeep Dutta. Self-organization of gold nanoparticles on silanated surfaces. *Beilstein Journal of Nanotechnology*, 6(1):2345–2353, 2015.
- [104] Jiali Wan, Jia-Hong Wang, Ting Liu, Zhixiong Xie, Xue-Feng Yu, and Wenhua Li. Surface chemistry but not aspect ratio mediates the biological toxicity of gold nanorods in vitro and in vivo. *Scientific Reports*, 5(1):11398, sep 2015.
- [105] José da Silva, Roberta Dias, Gabriel da Hora, Thereza Soares, and Mario Meneghetti. Molecular Dynamics Simulations of Cetyltrimethylammonium Bromide (CTAB) Micelles and their Interactions with a Gold Surface in Aqueous Solution. *Journal of the Brazilian Chemical Society*, 2017.
-

-
- [106] Biwu Liu and Juewen Liu. Methods for preparing DNA-functionalized gold nanoparticles, a key reagent of bioanalytical chemistry. *Analytical Methods*, 9(18):2633–2643, 2017.
- [107] Edward P. O’Brien, Bernard R. Brooks, and D. Thirumalai. Effects of pH on Proteins: Predictions for Ensemble and Single-Molecule Pulling Experiments. *Journal of the American Chemical Society*, 134(2):979–987, jan 2012.
- [108] T. Inagaki, R. N. Hamm, E. T. Arakawa, and L. R. Painter. Optical and dielectric properties of DNA in the extreme ultraviolet. *The Journal of Chemical Physics*, 61(10):4246–4250, nov 1974.
- [109] Helmut Hinterwirth, Stefanie Kappel, Thomas Waitz, Thomas Prohaska, Wolfgang Lindner, and Michael Lämmerhofer. Quantifying Thiol Ligand Density of Self-Assembled Monolayers on Gold Nanoparticles by Inductively Coupled Plasma–Mass Spectrometry. *ACS Nano*, 7(2):1129–1136, feb 2013.
- [110] Tatyana Abramova. Frontiers and Approaches to Chemical Synthesis of Oligodeoxyribonucleotides. *Molecules*, 18(1):1063–1075, jan 2013.
- [111] Ralf Jungmann, Christian Steinhauer, Max Scheible, Anton Kuzyk, Philip Tinnefeld, and Friedrich C. Simmel. Single-Molecule Kinetics and Super-Resolution Microscopy by Fluorescence Imaging of Transient Binding on DNA Origami. *Nano Letters*, 10(11):4756–4761, nov 2010.
- [112] Daniel Nieves, Katharina Gaus, and Matthew Baker. DNA-Based Super-Resolution Microscopy: DNA-PAINT. *Genes*, 9(12):621, dec 2018.
- [113] Eckhard Limpert, Werner A Stahel, and Markus Abbt. Log-normal Distributions across the Sciences: Keys and Clues: On the charms of statistics, and how mechanical models resembling gambling machines offer a link to a handy way to characterize log-normal distributions, which can provide deeper insight into variability and probability—normal or log-normal: That is the question. *BioScience*, 51(5):341–352, may 2001.
- [114] Sarah A. Mutch, Bryant S. Fujimoto, Christopher L. Kuyper, Jason S. Kuo, Sandra M. Bajjalieh, and Daniel T. Chiu. Deconvolving Single-Molecule Intensity Distributions for Quantitative Microscopy Measurements. *Biophysical Journal*, 92(8):2926–2943, apr 2007.
- [115] Idah C. Pekcevik, Lester C. H. Poon, Michael C. P. Wang, and Byron D. Gates. Tunable Loading of Single-Stranded DNA on Gold Nanorods through the Displacement of Polyvinylpyrrolidone. *Analytical Chemistry*, 85(20):9960–9967, oct 2013.
- [116] H.A. Haus and Weiping Huang. Coupled-mode theory. *Proceedings of the IEEE*, 79(10):1505–1518, 1991.
- [117] Tobias Jan August Kippenberg. *Nonlinear Optics in Ultra-high-Q Whispering-Gallery Optical Microcavities*. PhD thesis, California Institute of Technology, 2004.
-

- [118] Yuwen Hu, Linbo Shao, Stephen Arnold, Yong-Chun Liu, Cao-Yuan Ma, and Yun-Feng Xiao. Mode broadening induced by nanoparticles in an optical whispering-gallery microcavity. *Physical Review A*, 90(4):043847, oct 2014.
- [119] Lina He, Şahin Kaya Özdemir, Jiangang Zhu, Faraz Monifi, Huzeyfe Yılmaz, and Lan Yang. Statistics of multiple-scatterer-induced frequency splitting in whispering gallery microresonators and microlasers. *New Journal of Physics*, 15(7):073030, jul 2013.
- [120] D. Keng, X. Tan, and S. Arnold. Whispering gallery micro-global positioning system for nanoparticle sizing in real time. *Applied Physics Letters*, 105(7), 2014.
- [121] Serge Vincent, Sivaraman Subramanian, and Frank Vollmer. Optoplasmonic characterisation of reversible disulfide interactions at single thiol sites in the attomolar regime. *Nature Communications*, 11(1):2043, dec 2020.
- [122] Serge Rosenblum, Yulia Lovsky, Lior Arazi, Frank Vollmer, and Barak Dayan. Cavity ring-up spectroscopy for ultrafast sensing with optical microresonators. *Nature Communications*, 6:6788, 2015.
- [123] Georgios E. Katsoprinakis and T. Peter Rakitzis. Cavity-based chiral polarimetry: parity nonconserving optical rotation in Cs, Dy, and HgH. *Journal of Physics B: Atomic, Molecular and Optical Physics*, 52(21):213501, nov 2019.
- [124] Eric D. Black. An introduction to Pound–Drever–Hall laser frequency stabilization. *American Journal of Physics*, 69(1):79, 2001.
- [125] Jon D. Swaim, Joachim Knittel, and Warwick P. Bowen. Detection of nanoparticles with a frequency locked whispering gallery mode microresonator. *Applied Physics Letters*, 102(18):2011–2015, 2013.
- [126] Katherine Henzler-wildman and Dorothee Kern. Dynamic personalities of proteins. *Nature*, 450(December):7–9, 2007.
- [127] Petr Ptáček, František Šoukal, and Tomáš Opravil. Introduction to the Transition State Theory. In *Introducing the Effective Mass of Activated Complex and the Discussion on the Wave Function of this Instanton*. InTech, jul 2018.
- [128] Vickery L. Arcus, Erica J. Prentice, Joanne K. Hobbs, Adrian J. Mulholland, Marc W. Van der Kamp, Christopher R. Pudney, Emily J. Parker, and Louis A. Schipper. On the Temperature Dependence of Enzyme-Catalyzed Rates. *Biochemistry*, 55(12):1681–1688, mar 2016.
- [129] Hannah B.L. Jones, Stephen A. Wells, Erica J. Prentice, Anthony Kwok, Liyin L. Liang, Vickery L. Arcus, and Christopher R. Pudney. A complete thermodynamic analysis of enzyme turnover links the free energy landscape to enzyme catalysis. *FEBS Journal*, 284(17):2829–2842, 2017.

-
- [130] Marc W. van der Kamp, Erica J. Prentice, Kirsty L. Kraakman, Michael Connolly, Adrian J. Mulholland, and Vickery L. Arcus. Dynamical origins of heat capacity changes in enzyme-catalysed reactions. *Nature Communications*, 9(1):1177, dec 2018.
- [131] Hannu Häkkinen. The gold–sulfur interface at the nanoscale. *Nature Chemistry*, 4(6):443–455, jun 2012.
- [132] Yuyang Wang, Karsten van Asdonk, and Peter Zijlstra. A Robust and General Approach to Quantitatively Conjugate Enzymes to Plasmonic Nanoparticles. *Langmuir*, 35(41):13356–13363, oct 2019.
- [133] William Humphrey, Andrew Dalke, and Klaus Schulten. VMD: Visual molecular dynamics. *Journal of Molecular Graphics*, 14(1):33–38, feb 1996.
- [134] John Stone. *An Efficient Library for Parallel Ray Tracing and Animation*. Master’s thesis, Computer Science Department, University of Missouri-Rolla, April 1998.
- [135] Kenneth A. Johnson and Roger S. Goody. The Original Michaelis Constant: Translation of the 1913 Michaelis–Menten Paper. *Biochemistry*, 50(39):8264–8269, oct 2011.
- [136] Leslie B. Poole. The basics of thiols and cysteines in redox biology and chemistry. *Free Radical Biology and Medicine*, 80(5):148–157, mar 2015.
- [137] Mark James Abraham, Teemu Murtola, Roland Schulz, Szilárd Páll, Jeremy C. Smith, Berk Hess, and Erik Lindahl. GROMACS: High performance molecular simulations through multi-level parallelism from laptops to supercomputers. *SoftwareX*, 1-2:19–25, sep 2015.
- [138] George A. Kaminski, Richard A. Friesner, Julian Tirado-Rives, and William L. Jorgensen. Evaluation and reparametrization of the OPLS-AA force field for proteins via comparison with accurate quantum chemical calculations on peptides. *Journal of Physical Chemistry B*, 105(28):6474–6487, 2001.
- [139] F. Iori, R. Di Felice, E. Molinari, and S. Corni. GolP: An atomistic force-field to describe the interaction of proteins with Au(111) surfaces in water. *Journal of Computational Chemistry*, 30(9):1465–1476, jul 2009.
- [140] M. Ozboyaci, D. B. Kokh, and R. C. Wade. Three steps to gold: mechanism of protein adsorption revealed by Brownian and molecular dynamics simulations. *Physical Chemistry Chemical Physics*, 18(15):10191–10200, 2016.
- [141] H. J. C. Berendsen, J. R. Grigera, and T. P. Straatsma. The missing term in effective pair potentials. *The Journal of Physical Chemistry*, 91(24):6269–6271, nov 1987.
- [142] Peter G. Kusalik and Igor M. Svishchev. The Spatial Structure in Liquid Water. *Science*, 265(5176):1219–1221, aug 1994.
- [143] Shūichi Nosé. A molecular dynamics method for simulations in the canonical ensemble. *Molecular Physics*, 52(2):255–268, jun 1984.
-

-
- [144] William G. Hoover. Canonical dynamics: Equilibrium phase-space distributions. *Physical Review A*, 31(3):1695–1697, mar 1985.
- [145] Berk Hess, Henk Bekker, Herman J.C. Berendsen, and Johannes G.E.M. Fraaije. Lincs: A linear constraint solver for molecular simulations. *J. Comput. Chem*, 18:18–1463, 1997.
- [146] O. Flomenbom, K. Velonia, D. Loos, S. Masuo, M. Cotlet, Y. Engelborghs, J. Hofkens, A. E. Rowan, R. J. M. Nolte, M. Van der Auweraer, F. C. de Schryver, and J. Klafter. Stretched exponential decay and correlations in the catalytic activity of fluctuating single lipase molecules. *Proceedings of the National Academy of Sciences*, 102(7):2368–2372, feb 2005.
- [147] H. P. Lu. Single-Molecule Enzymatic Dynamics. *Science*, 282(5395):1877–1882, dec 1998.
- [148] X. S. Xie. Enzyme Kinetics, Past and Present. *Science*, 342(6165):1457–1459, dec 2013.
- [149] X. Sunney Xie. Single-molecule approach to dispersed kinetics and dynamic disorder: Probing conformational fluctuation and enzymatic dynamics. *The Journal of Chemical Physics*, 117(24):11024–11032, dec 2002.
- [150] Kelly Velonia, Ophir Flomenbom, Davey Loos, Sadahiro Masuo, Mircea Cotlet, Yves Engelborghs, Johan Hofkens, Alan E. Rowan, Joseph Klafter, Roeland J. M. Nolte, and Frans C. de Schryver. Single-Enzyme Kinetics of CALB-Catalyzed Hydrolysis. *Angewandte Chemie International Edition*, 44(4):560–564, jan 2005.
- [151] Yusdi Santoso, Catherine M. Joyce, Olga Potapova, Ludovic Le Reste, Johannes Hohlbein, Joseph P. Torella, Nigel D.F. Grindley, and Achillefs N. Kapanidis. Conformational transitions in DNA polymerase I revealed by single-molecule FRET. *Proceedings of the National Academy of Sciences of the United States of America*, 107(2):715–720, 2010.
- [152] Huanjun Chen, Xiaoshan Kou, Zhi Yang, Weihai Ni, and Jianfang Wang. Shape- and Size-Dependent Refractive Index Sensitivity of Gold Nanoparticles. *Langmuir*, 24(10):5233–5237, may 2008.
- [153] Péter Dombi, Zsuzsanna Pápa, Jan Vogelsang, Sergey V. Yalunin, Murat Sivis, Georg Herink, Sascha Schäfer, Petra Groß, Claus Ropers, and Christoph Lienau. Strong-field nano-optics. *Reviews of Modern Physics*, 92(2):025003, jun 2020.
- [154] H. P. Wagner, H. Schmitzer, J. Lutti, P. Borri, and W. Langbein. Effects of uniaxial pressure on polar whispering gallery modes in microspheres. *Journal of Applied Physics*, 113(24):243101, jun 2013.
- [155] Jessica Melin and Stephen R Quake. Microfluidic Large-Scale Integration: The Evolution of Design Rules for Biological Automation. *Annual Review of Biophysics and Biomolecular Structure*, 36(1):213–231, 2007.
- [156] Cyrill Kuemin, Lea Nowack, Luisa Bozano, Nicholas D. Spencer, and Heiko Wolf. Oriented assembly of gold nanorods on the single-particle level. *Advanced Functional Materials*, 22(4):702–708, 2012.
-

- [157] Valentin Flauraud, Massimo Mastrangeli, Gabriel D. Bernasconi, Jeremy Butet, Duncan T. L. Alexander, Elmira Shahrabi, Olivier J. F. Martin, and Juergen Brugger. Nanoscale topographical control of capillary assembly of nanoparticles. *Nature Nanotechnology*, 12(1):73–80, jan 2017.
- [158] G. P. Acuna, F. M. Moller, P. Holzmeister, S. Beater, B. Lalkens, and P. Tinnefeld. Fluorescence Enhancement at Docking Sites of DNA-Directed Self-Assembled Nanoantennas. *Science*, 338(6106):506–510, oct 2012.
- [159] Steven H. Huang, Xuefeng Jiang, Bo Peng, Corey Janisch, Alexander Cocking, Şahin Kaya Özdemir, Zhiwen Liu, and Lan Yang. Surface-enhanced Raman scattering on dielectric microspheres with whispering gallery mode resonance. *Photonics Research*, 6(5):346, may 2018.
- [160] James A. Maier, Carmenza Martinez, Koushik Kasavajhala, Lauren Wickstrom, Kevin E. Hauser, and Carlos Simmerling. ff14SB: Improving the Accuracy of Protein Side Chain and Backbone Parameters from ff99SB. *Journal of Chemical Theory and Computation*, 11(8):3696–3713, aug 2015.
- [161] K. Vanommeslaeghe, E. Hatcher, C. Acharya, S. Kundu, S. Zhong, J. Shim, E. Darian, O. Guvench, P. Lopes, I. Vorobyov, and A. D. Mackerell. CHARMM general force field: A force field for drug-like molecules compatible with the CHARMM all-atom additive biological force fields. *Journal of Computational Chemistry*, pages NA–NA, 2009.